Title

Clinical Assessment of Blood Stasis and Transport in the Left Ventricle

Author

Rossini, Lorenzo

Publication Date

2017

UNIVERSITY OF CALIFORNIA, SAN DIEGO

Clinical Assessment of Blood Stasis and Transport in the Left Ventricle

A dissertation submitted in partial satisfaction of the
requirements for the degree
Doctor of Philosophy

in

Engineering Sciences (Mechanical Engineering)

by

Lorenzo Rossini

Committee in charge:

- Professor Juan Carlos del Álamo, Chair
- Professor Andrew M. Kahn, Co-Chair
- Professor Albert Hsiao
- Professor Juan Lasheras
- Professor Andrew McCulloch
- Professor Elliot McVeigh
- Professor Daniel Tartakovsky

2017

The dissertation of Lorenzo Rossini is approved, and it is acceptable in quality and form for publication on microfilm or electronically:

Co-Chair

Chair

University of California, San Diego

2017

EPIGRAPH

You look at where you're going and where you are and it never makes sense,
but then you look back at where you've been and a pattern seems to emerge.
...
Sometimes it's a little better to travel than to arrive.

— Robert M. Pirsig
Zen and the Art of Motorcycle Maintenance: An Inquiry Into Values.

TABLE OF CONTENTS

Signature Page iii

Epigraph iv

Table of Contents v

List of Figures viii

List of Tables x

Acknowledgements xi

Vita xiii

Abstract of the Dissertation xv

Chapter 1 Introduction 1

Chapter 2 A clinical method for mapping and quantifying blood stasis in the left ventricle 4
- 2.1 Introduction 4
- 2.2 Methods 6
  - 2.2.1 Study population 6
  - 2.2.2 3D PCMRI: Image acquisition and processing 6
  - 2.2.3 2D Image acquinsition, analysis and processing 7
- 2.3 Residence time 8
  - 2.3.1 Evolution equation fot residence time 8
  - 2.3.2 PCMRI velocity correction for mass conservation . . 9
  - 2.3.3 Grid sensitivity analysis 10
- 2.4 Results and discussion 10
  - 2.4.1 Residence time in 3D 10
  - 2.4.2 LV residence time in non-ischemic dilated cardiomyopathy 15
  - 2.4.3 Changes in Blood Stasis After LVAD Implantation . . 17
  - 2.4.4 Simplified Residence Time Indices 19
- 2.5 Conclusions and study limitation 21
- 2.6 Appendix: Derivation of the residence time equation 25
  - 2.6.1 An Equation for the Standard Deviation of Residence Time 27
- 2.7 Acknowledgements 29

Chapter 3 A Prospective Study in Acute Myocardial Infarction 30
- 3.1 Introduction 30
- 3.2 Methods 31
  - 3.2.1 Study Population 31
  - 3.2.2 Image Acquisition and Analysis 34
  - 3.2.3 Magnetic Resonance Imaging 34
  - 3.2.4 Stasis Imaging and Mapping 35
  - 3.2.5 Statistical Analysis 37
- 3.3 Results 40
  - 3.3.1 Clinical Data and Convential Echocardiography . . . 40
  - 3.3.2 Stasis Imaging 41
  - 3.3.3 Determinants of Stasis 46
  - 3.3.4 Stasis and Mural Thrombosis 46
- 3.4 Discussion 48
  - 3.4.1 Stasis as an Index of Cardiac Physiology 48
  - 3.4.2 Myocardial Function and Stasis 52
  - 3.4.3 Limitations 53
  - 3.4.4 Clinical Implications 53
- 3.5 Conclusions 54
- 3.6 Acknowledgements 55

Chapter 4 Clinical assessment of intraventricular blood transport in patients undergoing cardiac resynchronization therapy 56
- 4.1 Introduction 56
- 4.2 Methods 58
  - 4.2.1 Study Population 58
  - 4.2.2 AV Delay Settings and Data acquisition 58
  - 4.2.3 2D Image Analysis and Intraventricular Flow Processing 60
  - 4.2.4 Blood Transport Assessment 61
  - 4.2.5 Statistical Analysis 65
- 4.3 Results 67
  - 4.3.1 Intraventricular Inflow and Blood Transport Under Cardiac Resynchronization Therapy 67
  - 4.3.2 Atrioventricular Delay and Blood Transport During Early and Late Filling 67
  - 4.3.3 Time-Evolution of Intraventricular Transport Regions 68
- 4.4 Discussion 71
- 4.5 Limitations 74
- 4.6 Conclusions 75
- 4.7 Acknowledgements 76

Chapter 5 Conclusions and future direction 77
5.1 Summary of the dissertation 77
5.2 Recommendations for future work 79
5.2.1 Left Ventricular Assist Device 79
5.2.2 Residence Time in the Left Atrium 80

Bibliography 82

LIST OF FIGURES

Figure 2.1: 3-D intraventricular velocity field and residence time map in a pig at mitral valve opening. 12
Figure 2.2: 3-D intraventricular velocity field and residence time map in a pig at the end of filling. 13
Figure 2.3: Snapshots of 2-D intraventricular residence time along the cardiac cycle in a healthy heart (A) and in two different examples of dilated cardiomyopathy (NIDCM) patients (B and C) 14
Figure 2.4: Snapshots of 2-D K and T_S before mitral valve opening in the last converged cardiac cycle in a healthy heart (A) and in two different examples of NIDCM (B and C). 16
Figure 2.5: Snapshots of 2-D intraventricular residence time along the cardiac cycle in a patient before (A) and after (B) LVAD implantation. . 18
Figure 2.6: Example of region tracking (A) and time evolution of V_{TR} (B), $T_{M,2}$ (C), $K_{M,2}$ (D), $T_{SM,2}$ (E) 20

Figure 3.1: Study populations flowchart. 33
Figure 3.2: Methodology. Methods used for image acquisition and processing. 2D+t: unsteady 2-dimensional. 36
Figure 3.3: Stasis Imaging. Boxplots and scatterplots of stasis indices for the control group and the AMI patients at the early and late phases. 43
Figure 3.4: Wall Jet & Stasis. Scatterplots and boxplots of stasis indices (pooled early, late and control studies) with and without wall filling jets. 44
Figure 3.5: Stasis & LVT. Boxplots and scatterplots of stasis indices of early-phase studies of the AMI cohort, with and without LVT. 47
Figure 3.6: ROC analyses. Receiver operating characteristic (ROC) curves for the average residence time and the endocardial contact length of stagnant regions for the diagnosis of LVT. 49
Figure 3.7: Examples. Patient without and with LVT. 51

Figure 4.1: Pulse wave Doppler inflow velocity as a function of time in a patient without CRT , and undergoing CRT at AVOPT, AVMAX, AVMIN, and atrial pacing at 100 bpm. 61
Figure 4.2: Evolution of filling transport regions in the LV. 64
Figure 4.3: Percentage LV volume occupied by E-wave and A-wave filling transport at mitral valve closing in patients (N=9) undergoing CRT with different AV delay settings, compared with healthy volunteers (N=3). 66
Figure 4.4: End-diastolic distribution of different transport regions in the LV of the same patient shown in Figures 4.2 and 4.4, plotted for different CRT settings 69

Figure 4.5: Statistics of intraventricular blood redirection efficiency at aortic valve opening in patients undergoing CRT with different AV delay settings, compared with healthy volunteers. 72

LIST OF TABLES

Table 2.1: Clinical data of the studied cases. 7
Table 2.2: Sensitivity analysis over 6 beats (6T). 11
Table 2.3: Time-averaged stasis indices for the cases under study. 22

Table 3.1: Clinical Data of the AMI Cohorts. 32
Table 3.2: Intra-class correlation coefficient (R_{ic}) and relative error (mean ± std) of the reproducibility study. 38
Table 3.3: Pearson correlation coefficient among the different indices of stasis. 39
Table 3.4: Conventional Ultrasound Data of the Full AMI Cohort and the Control Population. 41
Table 3.5: Stasis Mapping Data of the Full AMI Cohort and the Control Population. 42
Table 3.6: Stasis Mapping Data of the Full AMI Cohort and the Control Population in terms of cycles. 42
Table 3.7: Determinants of Stasis. Analysis performed using pooled data from early and late AMI as well as controls studies 45
Table 3.8: Receiver-operating characteristic curves (ROC) analysis of stasis metrics to predict LVT in AMI subjects. 50

Table 4.1: Summary of study population data. 59
Table 4.2: Intraclass correlation coefficient (R_{ic}) of the reproducibility study. 65
Table 4.3: Results of E and A wave tracking at mitral valve closing (average ± standard deviation). 67
Table 4.4: Average ± standard deviation of relative end-diastolic flow fractions of the LV for the different CRT settings. 70
Table 4.5: Flow kinematic efficiency parameters obtained at aortic valve opening. 71

ACKNOWLEDGEMENTS

There are so many of people whom I would like to acknowledge for having contributed to the success of my Ph.D. research and made these last five years an unforgettable, enriching and life-changing journey.

First of all, I want to thank with all my heart my advisor, Juan Carlos. Needless to say, withouth him, none of what you are reading would have been possible. Since the first time I met him in 2009, he has been a continuous role model to follow for scientific method and rigor, a cornerstone in my personal and professional development and a never-ending source of knowledge, support, encouragement and (mostly funny) jokes. I feel deeply honored to have been under his guidance for the past 5+ years.

Thanks to all the members of my doctoral committee for their support, for their suggestions and for their time. An exceptional mention goes to Andy, co-chair of the committee, for being the most trusted source of cardiological knowledge and for being such a friendly, yet meticulous research collaborator.

Next, my gratitude goes to the whole team of cardiologists and researchers I have been so lucky to collaborate with in the Hospital Gregorio Marañón in Madrid, Spain. In particular, I would like to thank Pablo, Javier, Raquel. Almost all the clinical data that is presented in this manuscript and was published in several journal articles comes from their amazing organization and hard work.

Thanks to all the amazing people of our research group: to Ernesto, Ricardiño and Shun for being such great friends, a diverse source of laughter, inspiration, suggestion, lunch-club organization and for always giving a good reason to be at work; to Marissa, Kristen, Stephanie, Ashish, Josh, Yi-Ting, Ruedi for their smiles, their insight and for being great labmates; to Juan for his continuous support, encouragement and inspiring discussions.

Thanks to all the other students and post docs in the Biomechanics wing of SME and in the Mechanical and Aerospace Engineering department, present and past, for making the workplace the perfect place to spend my days: Maxime, Morgan, Deba, Hari, Abhay, Justin, Mahdi, Daniele, Micheal, Miriam, Broto, Roberto, Gopesh, Joseph, Karcher.

Thanks to Lauran for being a loving and supporting girlfriend. A special thought to all the Italian friends who are or were at UC San Diego that always made me feel a bit home: Pigaz, Sabba, Jack, Tosone, Simone M., Martina, Francesca, Pardis, Simone S., Margherita, Marco, Gloria, Francesco, Giuseppe, Christian, Pietro, Lorenzo, Giorgio.

Finally, but perhaps the most important thanks to my mum, my dad, Sandro and all my beautiful family for always supporting me and making me grow with that curiosity that I believe is so important in everyone's life.

Chapter 2, in part, has been published in the *Journal of Biomechanics*. Rossini, Lorenzo; Martinez-Legazpi, Pablo; Vu, Vi; Fernández-Friera, Leticia; del Villar, Candelas Pérez; Rodríguez-López, Sara; Benito, Yolanda; Borja, María-Guadalupe; Pastor-Escuredo, David; Yotti, Raquel; Ledesma-Carbayo, MarÃŋa J.; Kahn, Andrew M.; Ibanez, Borja; Fernández-Avilés Francisco; May-Newman, Karen; Bermejo, Javier; del Álamo, Juan C. 2016. The title of this paper is "A clinical method for mapping and quantifying blood stasis in the left ventricle". The dissertation author was the primary author of this paper.

Chapter 3, in part, has been published in the *Journal of American College of Cardiology: Cardiovascular Imaging*. Martinez-Legazpi, Pablo; Rossini, Lorenzo; del Villar, Candelas Pérez; Benito, Yolanda; Devesa-Cordero, Carolina; Yotti, Raquel; Delgado-Montero, Antonia; Gonzalez-Mansilla, Ana; Kahn, Andrew M; Fernández-Avilés Francisco; Bermejo, Javier; del Álamo, Juan C. 2017. The title of this paper is "Stasis Mapping Using Ultrasound: A Prospective Study in Acute Myocardial Infarction". The dissertation author was the second author of this paper.

Chapter 4, in part, has been published in *Meccanica*. Rossini, Lorenzo; Martinez-Legazpi, Pablo; Benito, Yolanda; del Villar, Candelas Pérez; Gonzalez-Mansilla, Ana; Barrio, Alicia; Borja, María-Guadalupe; Yotti, Raquel; Kahn, Andrew M; Shadden, Shawn C; Fernández-Avilés Francisco; Bermejo, Javier; del Álamo, Juan C. 2017. The title of this paper is "Clinical assessment of intraventricular blood transport in patients undergoing cardiac resynchronization therapy". The dissertation author was the primary author of this paper.

VITA

2010	Laurea (B. S.) in Aerospace Engineering, Università di Bologna (Italy)
2012	Laurea Magistrale (M. S.) in Aerospace Engineering, Politecnico di Torino (Italy)
2012	Laurea Magistrale (M. S.) in Aerospace Engineering, Politecnico di Milano (Italy)
2013 - 2017	Graduate Research Assistant, University of California, San Diego
2013 - 2017	Teaching Assistant, University of California, San Diego
2017	Technology Management and Entrepreneurism fellowship program, Institute for the Global Entrepreneur, University of California, San Diego
2017	Ph. D. in Engineering Sciences (Mechanical Engineering), University of California, San Diego

PUBLICATIONS

Rossini, Lorenzo; Martinez-Legazpi, Pablo; Vu, Vi; Fernández-Friera, Leticia; del Villar, Candelas Pérez; Rodríguez-López, Sara; Benito, Yolanda; Borja, María-Guadalupe; Pastor-Escuredo, David; Yotti, Raquel; Ledesma-Carbayo, MarÃŋa J.; Kahn, Andrew M.; Ibanez, Borja; FernÃąndez-Avilés Francisco; May-Newman, Karen; Bermejo, Javier and del Álamo, Juan C., "A clinical method for mapping and quantifying blood stasis in the left ventricle", *Journal of biomechanics*, **49**, 2152 (2016).

Rossini, Lorenzo; Martinez-Legazpi, Pablo; Benito, Yolanda; del Villar, Candelas Pérez; Gonzalez-Mansilla, Ana; Barrio, Alicia; Borja, María-Guadalupe; Yotti, Raquel; Kahn, Andrew M; Shadden, Shawn C; FernÃąndez-Avilés Francisco; Bermejo, Javier and del Álamo, Juan C., "Clinical assessment of intraventricular blood transport in patients undergoing cardiac resynchronization therapy", *Meccanica*, **52**, 563 (2017).

Reider, Claudine; Moon, Juyeun; Ramesh, Varsha; Montes, Ricardo; Campos, Josue; Herold, Brian; Martinez-Legazpi, Pablo; Rossini, Lorenzo; del Alamo, Juan Carlos; Dembitsky, Walter and May-Newman, Karen, "Intraventricular thrombus formation in the LVAD-assisted heart studied in a mock circulatory loop", *Meccanica*, **52**, 515 (2017).

Martinez-Legazpi, Pablo; Rossini, Lorenzo; Pérez, Del Villar C; Benito, Yolanda; Devesa-Cordero, Carolina; Yotti, Raquel; Delgado-Montero, Antonia; Gonzalez-Mansilla, Ana; Kahn, Andrew M; Fernandez-Avilés, Francisco; del Álamo, Juan C. and Bermejo, Javier, "Stasis Mapping Using Ultrasound: A Prospective Study in Acute Myocardial Infarction", *JACC. Cardiovascular imaging*, (2017).

Braun, Oscar O; Brambatti, Michela; Almeida, Shone; Mizeracki, Adam; Rossini, Lorenzo; Miramontes, Marissa; Martinez-Legazpi, Pablo; Benito, Yolanda; Bermejo, Javier; Kahn, Andrew M; del Álamo, Juan C. and Adler, Eric D., "Non-Invasive Mapping of Intraventricular Flow Patterns in Patients Treated with Left Ventricular Assist Devices", *Journal of Cardiac Failure*, **23**, S24 (2017).

ABSTRACT OF THE DISSERTATION

Clinical Assessment of Blood Stasis and Transport in the Left Ventricle

by

Lorenzo Rossini
Doctor of Philosophy in Engineering Sciences (Mechanical Engineering)

University of California San Diego, 2017

Professor Juan Carlos del Álamo, Chair
Professor Andrew M. Kahn, Co-Chair

Blood stasis in the cardiac chambers is a recognized risk factor for intracardiac thrombosis and potential cardiogenic embolic events. In patients at risk of intraventricular thrombosis, the benefits of anticoagulation therapy must be balanced with its pro-hemorrhagic effects. In the healthy heart, instead, left ventricular (LV) flow patterns have been proposed to optimize blood transport by coupling diastole and systole.

This work introduces a novel flow image-based method to assess LV blood stasis and transport by processing flow-velocity images obtained by 2D color-Doppler velocimetry or phase-contrast magnetic resonance. This approach is based on quantifying the LV blood Residence Time (T_R) from time-resolved blood velocity fields by solving the advection equation for a passive scalar. This equation can be derived from statistical mechanics and the process can be further generalized to higher order moments of the time distribution to find, for example, the T_R standard deviation.

We showed proof-of-concept feasibility of the method in normal hearts, patients with dilated cardiomyopathy and patients before and after the implantation of a left ventricular assist device (LVAD). We then conducted two clinical studies on two populations of patients: with acute myocardial infarction (AMI) and undergoing cardiac resynchronization therapy (CRT).

In patients with AMI we identified the biomechanical determinants of stasis and addressed the techniqueâĂŹs potential to predict LV thrombosis. T_R was longer in the early than in the late phases of AMI and longer in AMI than in controls. The largest stagnant regions were identified in acute stage of the AMI and stasis metrics performed well to predict LV thrombosis.

To track blood transport in the LV of patients undergoing CRT we used a modified analysis with time-varying inflow boundary conditions. The device programming was varied to analyze flow transport under different atrioventricular conduction delays, and to model tachycardia. The analysis showed how CRT influences the transit of blood, contributes to conserving kinetic energy, and favors the generation of hemodynamic forces that accelerate blood in the direction of the LV outflow tract.

This work paves the way for using T_R-derived measures of bloos stasis as a relevant bio-marker in the clinical setting.

Chapter 1

Introduction

It is expected that cardiovascular diseases will be the leading cause of mortality worldwide by 2030. Cardioembolic stroke is one of the most devastating consequences of cardiac diseases, both in terms of mortality and disability. Amongst all causes of stroke, the cardioembolic etiology is associated to the highest mortality rate and reaches 20 % in some prospective series [2].

Three major mechanisms promote intracardiac thrombosis and embolism in cardiac diseases. First, endocardial injury due to surgery, chronic stretch or ischemic necrosis activates clot formation by exposing pro-coagulation factors of the basal membrane. Additionally, cardiac diseases are frequently associated to chronic inflammation and increased catecholamine and inflammatory cytokine levels which induce a systemic hypecoagulable state. Finally, blood flow stagnation triggers the activation of the coagulation system. These three predisposing factors are classically known as "Virchow's triad" [48]. Diseases such as atrial fibrillation, myocardial infarction, dilated and hypertrophic cardiomyopathies are well established conditions that increase the risk of cardiac embolisms by a combination of these three mechanisms.

In patients at risk of intraventricular thrombosis, the benefits of chronic anticoagulation therapy need to be balanced with the pro-hemorrhagic effects of therapy. In the absence of atrial fibrillation, there is no clinical evidence supporting the indication of chronic anticoagulation therapy in cardiac diseases where intraventricular thrombosis may be a major complication, such as dilated or hypertrophic cardiomyopathies, or after the implantation of left ventricular assistance devices (LVADs) in patients with refractory heart failure. Indeed, a number of trials based on clinical markers of thrombosis have failed to demonstrate a net benefit of such therapies in terms of overall clinical outcomes. However, these trials were performed without a patient-specific risk quantification of intraventricular thrombosis. Blood stasis in the cardiac chambers is an important risk factor for intracardiac thrombosis and potential cardiogenic embolic events. Therefore, we hypothesized that a robust and clinically applicable method for measuring and visualizing intraventricular stasis could provide useful surrogate markers of the risk of intraventricular thrombus formation.

In chapter 2, we introduce a novel flow image-based method to assess left ventricular (LV) blood stasis by digital processing flow-velocity images obtained either by phase-contrast magnetic resonance (PCMR) or 2D color-Doppler velocimetry (echo-CDV). This approach is based on quantifying the distribution of the blood Residence Time (T_R) from time-resolved blood velocity fields in the LV by solving the advection equation for a passive scalar.

We tested the new method in illustrative examples of normal hearts, two patients with dilated cardiomyopathy and one patient before and after the implantation of a left ventricular assist device (LVAD). The method allowed us to assess in-vivo the location and extent of the stasis regions in the LV. Original metrics were developed to integrate flow properties into simple scalars suitable for a robust and personalized assessment of the risk of thrombosis.

In chapter 3, the T_R-based analysis was tested in patients with acute myocardial infarction (AMI) to identify the biomechanical determinants of increased stasis and to address tho quantify left ventricular blood stasis, to identify the biomechanical determinants of stasis, and to address the technique's potential to predict LV mural thrombosis (LVT). This population of patients is homogeneous and highly selected so that it constitutes the ideal benchmark to test the relation between blood stasis (measured through the residence time approach) and the formation of a thrombus in presence of endocardium injury and a state of hypercoagulability. We obtained intraventricular stasis maps from conventional Doppler echocardiography sequences in 73 patients in the early (72 hours) and late (4-5 months) phases after a first anterior-AMI. 37 healthy subjects were studied as controls. We calculated the spatio-temporal maps of blood residence time in the LV (the time spent by fluid elements inside the chamber), and characterized the main features of stagnant regions. Stasis mapping provides new insights into the genesis of blood stasis and seems a promising tool to assess the patient-specific risk of intracavitary thrombosis in cardiac diseases.

Chapter 4 focuses on how different flow patterns influence LV blood transport in patients undergoing cardiac resynchronization therapy (CRT). This approach is still based upon solving the advection equation for a passive scalar field from time-resolved blood velocity fields. Imposing time-varying inflow boundary conditions for the scalar field provides a straightforward method to distinctly track the transport of blood entering the LV in the different filling waves of a given cardiac cycle, as well as the transport barriers which couple filling and ejection. We applied this method to analyze flow transport in a group of patients with implanted CRT devices and a group of healthy volunteers. In the patients under CRT, the device programming was varied to analyze flow transport under different values of the atrioventricular conduction delay, and to model tachycardia (100 bpm). Using this method, we show how CRT influences the transit of blood inside the left ventricle, contributes to conserving kinetic energy, and favors the generation of hemodynamic forces that accelerate blood in the direction of the LV outflow tract.

From a clinical perspective, this work introduces the new paradigm that quantitative flow dynamics can provide the basis to obtain subclinical markers of intraventricular thrombosis risk. The early prediction of LV blood stasis may result in decrease strokes by appropriate use of anticoagulant therapy for the purpose of primary and secondary prevention.

Chapter 2

A clinical method for mapping and quantifying blood stasis in the left ventricle

2.1 Introduction

Cardiovascular diseases are the leading cause of mortality worldwide and are projected to cause more than 20 million deaths per year by 2030. Cardioembolic stroke is one of the most devastating consequences of cardiac diseases, both in terms of mortality and disability. Amongst all causes of stroke, the cardioembolic etiology is associated with the highest mortality rate and reaches 20 % in some prospective series [2].

Three major mechanisms promote intracardiac thrombosis and embolism in cardiac diseases. First, endocardial injury, due to surgery, chronic stretch or ischemic necrosis, activates clot formation by exposing pro-coagulation factors of the basal membrane.

Additionally, cardiac diseases are frequently associated with chronic inflammation, and increased catecholamine and inflammatory cytokine levels, which induce a systemic hypercoagulable state. Finally, blood flow stagnation triggers the activation of the coagulation system. These three predisposing factors are classically known as "Virchow's triad" [48]. Diseases such as atrial fibrillation, myocardial infarction, dilated and hypertrophic cardiomyopathies are well-established conditions that increase the risk of cardiac embolisms by a combination of these three mechanisms.

Anticoagulation therapy has proven to be effective for decreasing the risk of cardioembolic events. However, the benefits of anticoagulation are frequently neutralized by the increased hemorrhagic risk associated with this therapy [51]. In fact, most clinical trials assessing the efficacy of primary prevention of anticoagulation therapy in non-AF cardioembolic diseases have been negative or neutral [4, 36]. These trials have been based on clinical risk factors and demographic variables, because precision individualized risk assessment methods are lacking. We hypothesize that imaging-based biomarkers are particularly well suited for this purpose.

Mechanical left-ventricular-assisted-devices (LVADs) are being used as temporary and destination therapies in an increasing number of patients with end-stage heart failure (HF) [75]. However, intraventricular thrombosis is a well-recognized complication of LVADs and may lead to device malfunction and embolism. A quantitative and individualized topologic assessment of the chamber regions at particular risk for thrombus development may help to define the ideal locations for the insertion of the LVAD cannulas on a patient-specific basis and, to optimize the device operating settings.

Flow in the heart involves complex fluid transport and mixing processes [7]. Intracardiac transport and mixing depends on convoluted trajectories of flow inside the chambers [42, 83, 89] as well as on the dynamical interactions between incoming flow and residual flow from preceding cycles [10]. In the healthy heart, these phenomena result in a small residual volume with no associated blood stasis. However, intraventricular flow patterns are significantly altered by disease [6, 17, 37, 64]. How these disturbed flow dynamics may lead to increased blood stasis is only beginning to be understood [17, 35].

Currently, there are no tools capable of a high-throughput measurement of flow stasis in the clinical setting. There have been only a few attempts to define indices of intraventricular blood stasis using in vitro and computational models [62, 84]. However, most of these indices are based on Eulerian flow metrics and therefore fail to capture the intricate unsteady nature of blood flow transport, as well as the mixing between the blood volume entering the LV each heart beat and the residual volume from preceding ones [35].

The present study was designed to implement a novel method for measuring and mapping blood stasis in the heart. The purpose was to obtain individual quantitative metrics of global and regional stasis from flow-velocity measurements in the LV. The feasibility of the method was first tested in a high-resolution three-dimensional dataset of LV flow velocity obtained in a large animal by phase-contrast magnetic resonance (PCMRI). To generalize the applicability of the tool we also adapted the method to work with ultrasound data. We analyzed data from healthy and diseased LVs, as well as before and after LVAD implantation. We demonstrate the unique ability of the tool to identify and track the regions at risk of blood stagnation, providing qualitative and topological assessments of blood stasis in the LV.

2.2 Methods

2.2.1 Study population

The present study is based on the following data: 1) high-resolution 3D PCMRI data from a pig scanned under highly controlled heart and respiratory rates, and 2) color-Doppler ultrasound datasets from 2 patients with non-ischemic dilated cardiomyopathy (NIDCM), one healthy volunteer without known heart disease and no cardiovascular risk factors, and one patient with end-stage HF both before and after LVAD implantation. Ultrasound datasets were randomly selected from a large database of two-dimensional velocity maps recruited at our institutions. The study protocol was approved by the local institutional review committee and all subjects provided written informed consent for this study. Clinical data are summarized in Table 2.1.

2.2.2 3D PCMRI: Image acquisition and processing

A high-resolution 3D PCMRI of the LV together with its corresponding 3D anatomical images were obtained in a male Large White pig under anesthesia, using a 3T magnet (Achieva-Tx, Philips Medical Systems, Best, the Netherlands), equipped with a 32-channel cardiac phased-array surface coil. Images were acquired during

Table 2.1: Clinical data of the studied cases. H.R: Heart rate, EDV: End-Diastolic Volume, ESV: End-Systolic Volume, EF: Ejection fraction, HEALTHY: healthy volunteer; NIDCM: non-ischemic dilated cardiomyopathy; LVAD: left ventricle assist device.

ID	Age	Gender	Regional Wall Motion	H.R. (b.p.m.)	EDV (mL)	ESV (mL)	EF (%)
HEALTHY	51	F	Normal	64	98	31	68
NIDCM-1	47	M	Inferior & posterior akinesis	80	81	62	24
NIDCM-2	64	F	Global hypokinesis	76	154	117	24
PRE-LVAD	63	F	Inferior & septal akinesis	68	156	111	29
POST-LVAD	63	F	LVAD	100	84	63	25
PIG	1	M	Normal	76	—	—	—

spontaneous ventilation using retrospective electrocardiographic gating. 3D PCMRI images were planned in a standard 4 and 2-chamber view to cover the entire LV from the level of the mitral annulus to the apex. The following imaging parameters were used: FOV 240x240 mm, voxel size 2x2x4 mm, 1 NEX, SENSE 2, reconstructed heart phases 25 corresponding to a time resolution of 34 ms, PC flow directions RL-AP-FH, act. T_R /TE (ms) = 6.0 / 3.7 and VENC of 100 cm/s, as similarly reported [25]. The velocity field inside the ventricle was obtained from the phase data after correcting for phase-aliasing artifacts through phase unwrapping of closed regions with abnormal intensity gradient. Each anatomical image was post processed using a semi-automatic volume segmentation tool in order to obtain the ventricle boundary surface throughout the cardiac cycle. The segmentation method is based on a multi-resolution level-set active contour optimized for heart segmentation [30].

2.2.3 2D Image acquinsition, analysis and processing

Comprehensive 2-dimensional (2D) B-mode and color-Doppler echocardiographic examinations were performed using a Vivid 7 scanner and 2-4 MHz transducers (General Electric Healthcare). The LV myocardial wall was segmented, and its longitudinal and transversal strain were measured from the apical long-axis B-mode sequences to delineate the endocardial boundary (EchoPac v.110.1.2, General Electric Healthcare). We reconstructed the 2D+t flow field inside the LV using 2D echo color Doppler velocimetry (echo-CDV), as previously described and validated in vitro [24] and in vivo [6]. The 2D flow velocity fields together with the LV segmentation were used to integrate the unit-forced transport equation and to calculate the spatio-temporal evolution of blood residence time inside the LV (see below). Conventional Doppler-echocardiographic data was recorded following current recommendations [44].

2.3 Residence time

2.3.1 Evolution equation fot residence time

The time spent by a blood particle inside the LV can be evaluated by a scalar magnitude known as Residence Time (T_R). Using a Lagrangian approach, T_R evolution can be described by the advection equation with unit forcing,

$$\frac{\partial T_R}{\partial t} + \nabla \cdot (\vec{v}_{inc} T_R) = 1 \tag{2.1}$$

where $\vec{v}_{inc}$ is the velocity field, imposing zero-flux boundary conditions at the endocardial wall and homogeneous Dirichlet conditions at the inlet/outlet. Previous works have considered a similar equation with a non-zero mass diffusivity term [20, 49], but we note that the self-diffusivity of blood is negligible compared to its advective fluxes inside the LV [7, 73]. The full derivation of equation (2.1) can be found in this chapter's Appendix. In the absence of a diffusive term, equation (2.1) can be completed with explicit Dirichlet boundary conditions at the inlet, S_in, when the blood coming from the left atrium enters the ventricle domain V_{LV}.

Equation (2.1) was numerically integrated on a Cartesian grid using a second-order Finite Volume discretization, in which T_R and $\vec{v}_{inc}$ were respectively interpolated at each cell's center and faces. We used a Total Variation Diminishing (TVD) flux limiting scheme [46] to avoid the numerical oscillations that would appear at the sharp interfaces created by the transport process, particularly between fresh blood entering the LV each cycle and the residual blood from previous cycles. A second-order time integration scheme was performed adopted keeping the Courant-Friedrichs-Lewy (CFL) number below 0.5 throughout the whole integration and using a variable time step, $\varDelta t$, bounded between 0.005-0.0003 ms for the 2D-echo-CDV and 0.033-0.0005 ms for the 3D PCMRI data. The velocity field at each integration step was obtained by linearly interpolating in time the previous and the successive velocity acquisition data frames. Spatio-temporally connected pixels with high residence time (e.g. $T_R > 2$ sec) were clustered and stored for further analysis using in-house algorithms. Clusters smaller than 2% LV volume (area in 2-D) and clusters that did not span the whole cardiac cycle were discarded and were not analyzed further.

2.3.2 PCMRI velocity correction for mass conservation

Similar to other flow measurement techniques, PCMRI provides velocity fields with noise that usually do not satisfy mass conservation (i.e. $\nabla \cdot \vec{v}_{inc} \neq 0$). Although noise can be minimized by appropriate fine-tuning during data acquisition, appreciable errors remain in current state-of-the-art PCMRI measurements [13]. Errors in mass conservation are particularly troublesome for the purpose of analyzing blood transport and residence time because they introduce a spurious source term equals to $-T_R \nabla \cdot \vec{v}_{inc}$ in the transport equation (2.1). This spurious term can generate undesired variations in T_R that are not caused by convective blood transport. In this work, we apply a solenoidal projection method to enforce the condition that the PCMRI velocity field is incompressible [14]. Note that, since the echo-CDV fields are derived by enforcing mass conservation [24], they automatically satisfy this condition.

Briefly, a velocity field derived from a potential function ϕ is added to the original field, $\vec{v}_0$: $\vec{v}_{inc} = \vec{v}_0 + \nabla \phi$. Imposing that $\vec{v}_{inc}$ is divergence-free allows for calculating ϕ by solving a Poisson's equation with non-homogeneous Neumann boundary conditions at the LV walls. This problem was solved using a custom Multi-Grid method developed in FORTRAN, interpolating the original domain onto a Cartesian grid. The moving boundary was defined independently of the Cartesian grid by using a sharp interface immersed boundary method [53].

2.3.3 Grid sensitivity analysis

While time-resolved 3D PCMRI provides invaluable information about the multi-dimensional flow transport and stasis patterns in the LV, the moderate spatio-temporal resolution ($\mathit{\Delta} x = \mathit{\Delta} y = 0.94$ mm, $\mathit{\Delta} z = 2$ mm and $\mathit{\Delta} t = 0.033$ ms) of this technique could pose a potential limitation. To rule out this possibility, we performed a sensitivity analysis of the dependence of the T_R maps on the time and space resolution in the echo-CDV data, which is better resolved ($\mathit{\Delta} x = 0.5$ mm and $\mathit{\Delta} t = 0.005$ ms). We progressively deteriorated the resolution of $N = 3$ echo-CDV datasets and computed the average L_2 norm of the error in the T_R fields as a function of $\mathit{\Delta} x$ and $\mathit{\Delta} t$. Table 2.2 summarizes the results of this analysis, and suggests that the resolution of the PCRMI data used in this work was sufficient to accurately resolve the spatiotemporal evolution of the residence time.

2.4 Results and discussion

2.4.1 Residence time in 3D

The 3D+t spatiotemporal distribution of T_R in the LV was calculated from PCMRI data. Figures 2.1 and 2.2 display 3D renderings of T_R at mitral valve opening and at isovolumic contraction, respectively. The velocity field shows the strong diastolic jet and associated vortex ring that characterizes LV filling flow [7]. In this ventricle the region of highest T_R is located close to the apex, and extends towards the aortic tract along the anteroseptal wall. This residence time pattern agrees well with the pattern observed in normal human LVs (see example in Figure 2.3A). The three-dimensionality of the T_R field is evident in Figures 2.1 and 2.2, and is caused by the complexity of intraventricular blood flow and transport during the cardiac cycle. However, the main features of this field are relatively well captured in the three-chamber view (delineated by the magenta contour in Figure 1), particularly the maximum value of T_R and its apical location. This result is important because our echocardiographic estimation approach to estimate of T_R in humans using conventional echocardiography is performed from velocity fields acquired in the three-chamber view.

Table 2.2: Sensitivity analysis over 6 beats (6T): mean ± standard deviation, of the L_2 norm of the error, defined above, compared to the reference frame in 3 different cases.

	dt [ms]				
	3.9 ± 0.4	7.8 ± 0.7	15.7 ± 1.5	39.2 ± 3.8	78 ± 7.5
	Number of input frames				
Nx × Ny, dx [mm]	200	100	50	20	10
256×256,0.35 ± 0.02	Reference:$\tilde{T}_R$	0.022 ± 0.015	0.121 ± 0.02	0.15 ± 0.039	0.297 ± 0.104
128×128,0.70 ± 0.04	0.123 ± 0.018	0.124 ± 0.018	0.154 ± 0.02	0.173 ± 0.029	0.28 ± 0.092
64×64, 1.42 ± 0.08	0.212 ± 0.027	0.21 ± 0.028	0.218 ± 0.03	0.227 ± 0.024	0.282 ± 0.075
32×32, 2.88 ± 0.16	0.295 ± 0.028	0.293 ± 0.029	0.293 ± 0.029	0.296 ± 0.028	0.32 ± 0.049
16×16, 5.96 ± 0.32	0.394 ± 0.035	0.395 ± 0.036	0.401 ± 0.041	0.406 ± 0.055	0.396 ± 0.035

$$||err||_2 = \sqrt{\frac{\int_{t=0}^{t=6T} \int_{\Omega} \left(\tilde{T}_R - T_R\right)^2 \mathrm{d}x\mathrm{d}y\mathrm{d}t}{\int_{t=0}^{t=6T} \int_{\Omega} \tilde{T}_R^{\,2} \mathrm{d}x\mathrm{d}y\mathrm{d}t}}$$

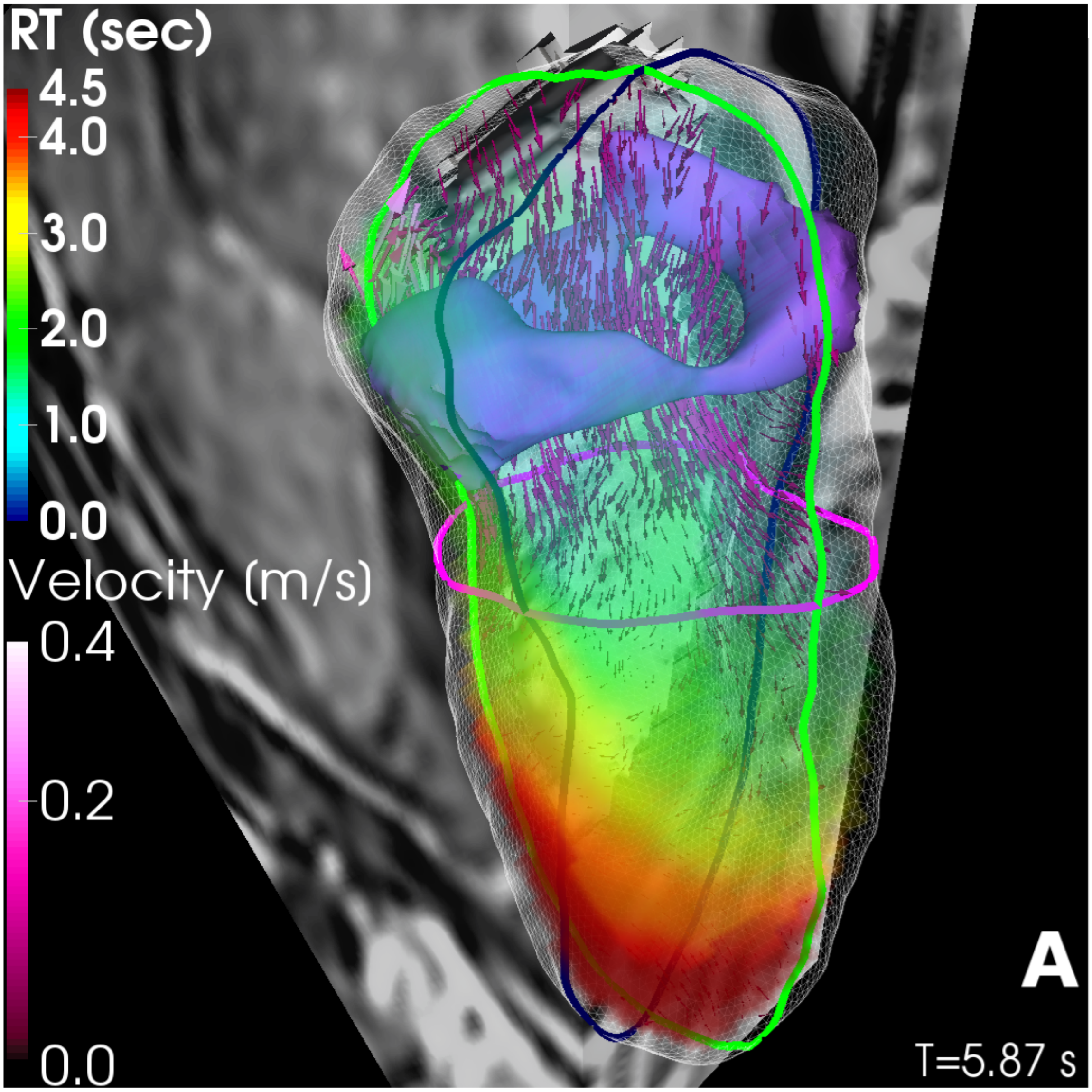

Figure 2.1: 3-D intraventricular velocity field and residence time map in a pig at mitral valve opening. The wireframe contour depicts the LV volume segmentation. The magenta and contour lines identify the long-axis plane that contains the mitral valve, apex and aortic valve. The vortical structures in purple are visualized by isosurfaces of λ_{ci} (imaginary part of the complex conjugate eigenvalue of $\nabla\vec{v}$).

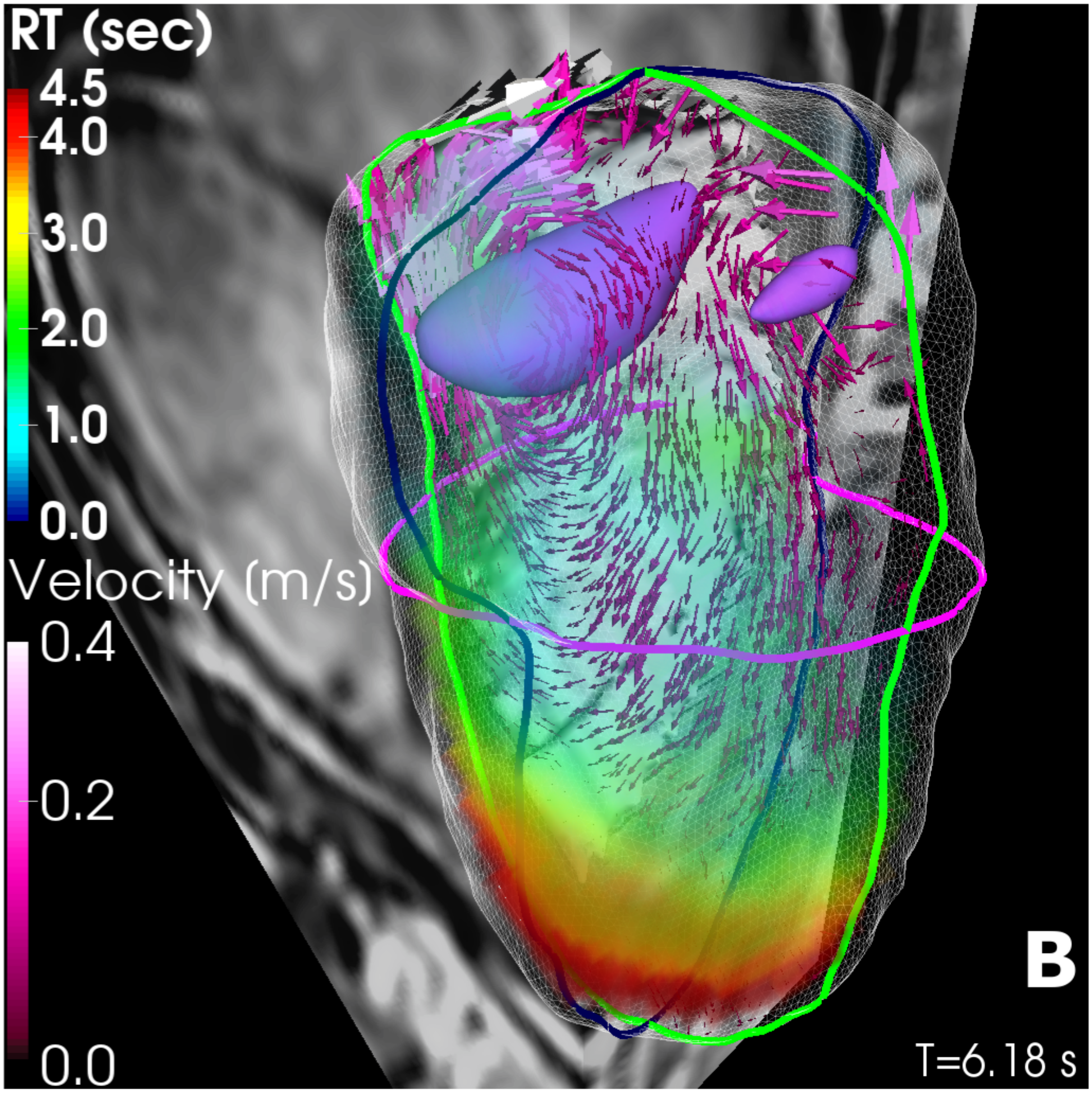

Figure 2.2: 3-D intraventricular velocity field and residence time map in a pig at the end of filling. The wireframe contour depicts the LV volume segmentation. The magenta and contour lines identify the long-axis plane that contains the mitral valve, apex and aortic valve. The vortical structures in purple are visualized by isosurfaces of λ_{ci} (imaginary part of the complex conjugate eigenvalue of $\nabla\vec{v}$).

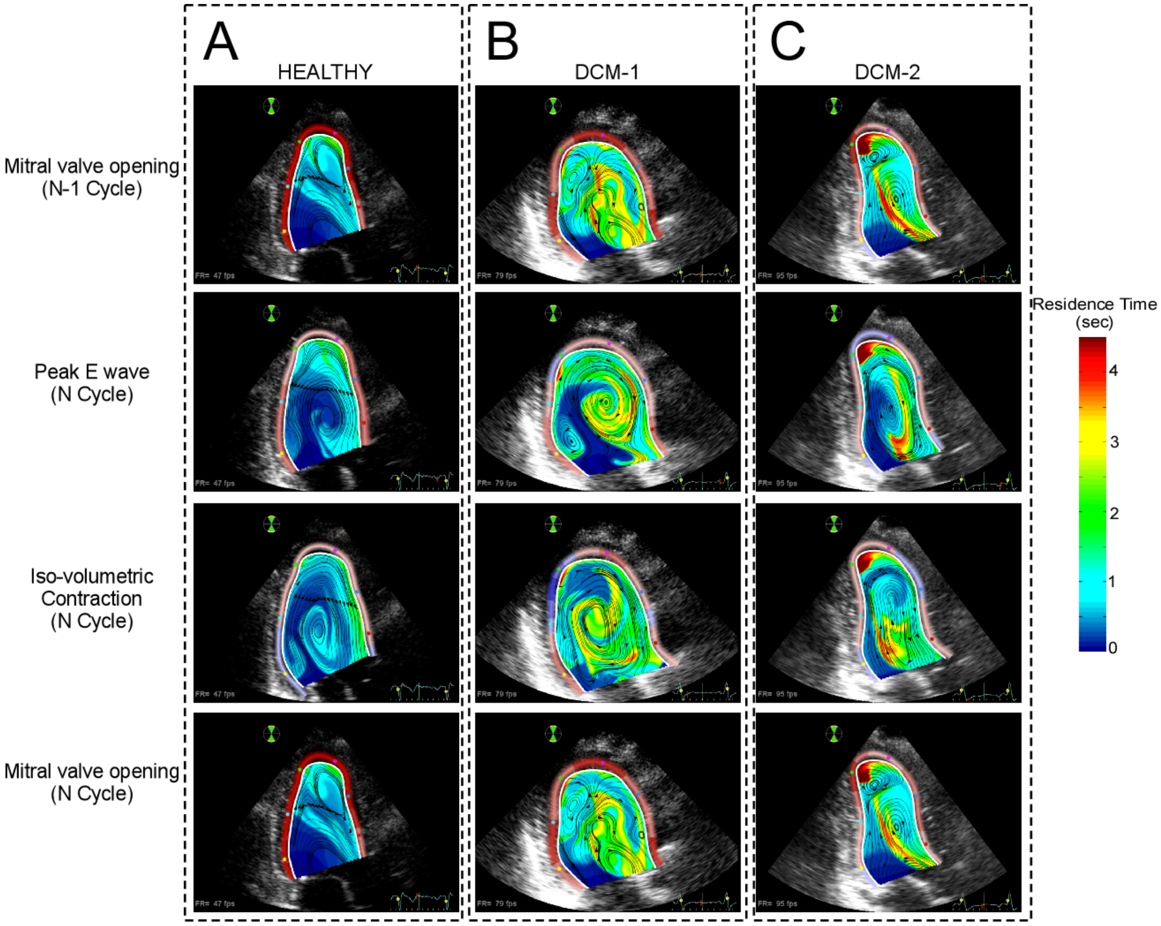

Figure 2.3: Snapshots of 2-D intraventricular residence time along the cardiac cycle in a healthy heart (A) and in two different examples of dilated cardiomyopathy (NIDCM) patients (B and C). 1st row: Residence Time mapping at the mitral valve opening in the converged N-1 cycle. 2nd row: Residence Time mapping at peak E-wave in the last computed cycle. 3rd row: Residence Time mapping at the iso-volumetric contraction in the last computed cycle. 4th row: Residence Time mapping at mitral valve opening in the last cycle. Notice that in both NIDCMs there coexist different regions with high Tr.

2.4.2 LV residence time in non-ischemic dilated cardiomyopathy

Dilated cardiomyopathy is a condition associated with increased risk of intraventricular thrombosis. The normal LV flow pattern has been reported to recycle the blood volume inside the left ventricle every 2-3 heart beats (Figure 2.3A) [10, 18, 35, 78]. However, blood transport is significantly altered in patients with NIDCM by the large swirling flow patterns that are typical of this condition (Figure 2.3B-C) [6, 35]. In these patients, blood is trapped inside long-lasting vortices and undergoes rotation throughout most of the cardiac cycle (see supplementary movie 1). Thus, proper assessment of intraventricular stasis should consider factors such as the distortion of fluid particles and their kinetic energy density in addition to T_R. The kinetic energy density of a fluid particle, defined as $K = \left(u^2 + v^2\right)/2$, can be used together with T_R as an intuitive indicator of stasis. However, kinetic energy is not a Galilean invariant and it could be possible for a fluid parcel to have high values of K while moving with little distortion, similar to a rigid solid. The distortion of a fluid particle can be quantified by the second invariant of the symmetric strain tensor $S_{ij} = \left(\frac{\partial u_i}{\partial x_j} + \frac{\partial u_j}{\partial x_i}\right)/2$. For an incompressible flow, the first invariant of S_{ij} is zero and the second invariant is defined as $Q_S = \mathrm{trace}\left(S_{ij}^2\right)/2$. Note that Q_S has dimensions of squared inverse of time, so it can be used to define a second stasis timescale $T_S = Q_S^{-1/2}$ in addition to T_R.

Figure 2.4 shows the spatial distributions of K and T_S in the regions with $T_R > 2$ sec for the same ventricles of figure 2.3, at the end of diastole. As expected, the normal LV (Figure 2.4A) does not show any significant region with $T_R > 2$ sec. There is a small cluster located near the endocardium but it has relatively high K and low T_S. Interestingly, both dilated LVs (Figure 2.4B-C) show large regions with $T_R > 2$ sec located at the center of the chamber but these regions are associated with high values of K and low values of T_S. This indicates that blood is continuously being stirred by the LV flow patterns in this centrally located region despite having high T_R . By contrast, the second diseased LV (Figure 2.4C) shows a separate, apically located region with $T_R > 2$ sec that also has low K and high T_S, and is therefore stagnant. These results illustrate how the combined analysis of the spatio-temporal

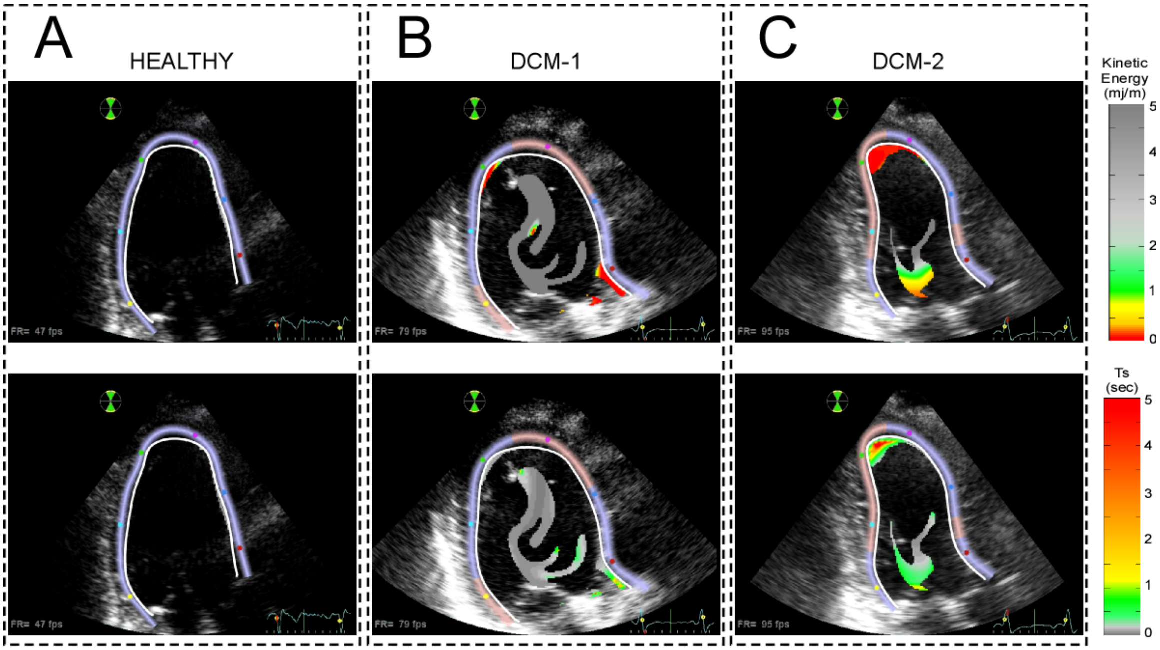

Figure 2.4: Snapshots of 2-D K and T_S before mitral valve opening in the last converged cardiac cycle in a healthy heart (A) and in two different examples of NIDCM (B and C). 1st row: Kinetic energy density (K) mapping in the regions with in the regions with $T_R > 2$ s. 2nd row: Distortion time (T_S) in the regions with $T_R > 2$ s. The NIDCM-2 case is at risk of apical blood stasis given the combination of low K and large T_S.

Lagrangian patterns of residence time and Eulerian measures of fluid motion and distortion can provide clinically accessible information about intraventricular blood stasis from conventional color-Doppler datasets.

2.4.3 Changes in Blood Stasis After LVAD Implantation

Implantable cardiac assist devices, particularly LVADs, are considered to alter the physiological blood flow patterns in the heart, leading to increased risk of thrombosis [9, 84]. Among the three elements of Virchov's triad, abnormal flow patterns present the most complex challenge to improve device design and post-implantation patient management [43]. However, blood stasis has not been previously measured in the patients implanted with LVADs.

Figure 2.5 shows residence time maps along a cardiac cycle in a patient with NIDCM, mitral regurgitation and end-stage HF before and 1 month after LVAD implantation. The pre-LVAD condition (Figure 2.5A) shows a large region with $T_R >$ 2 sec located at the center of the chamber, which is caused by the large swirling region that is sustained during most of the cardiac cycle in this dilated heart. This large swirling pattern is indicated by the circular instantaneous streamlines in Figure 2.5A. Consistent with the results presented in Figure 2.4, this region is associated with relatively high values of kinetic energy density and low values of T_S , implying that this region is not stagnant. However, this flow and stasis pattern are significantly altered after LVAD implantation, as the flow is channeled from the mitral annulus to the LVAD inflow cannula located at the LV apex, instead of transiting towards the outflow tract (magenta line in Figure 2.5B). As a result, a region with high residence time, moderate low kinetic energy and moderate low fluid distortion (moderately high T_S) appears near the LV outflow tract. These factors combined are the hallmark of blood stasis, suggesting a hemodynamic explanation for clinical reports of mural thrombosis in the LV outflow tract of LVAD-implanted patients [52]. These in vivo results generally agreeare in agreement with previous in vitro experiments performed using a cardiac simulator [84], although it should be noted that the drastic LV volume unloading caused by LVAD implantation was not modeled in the in vitro study.

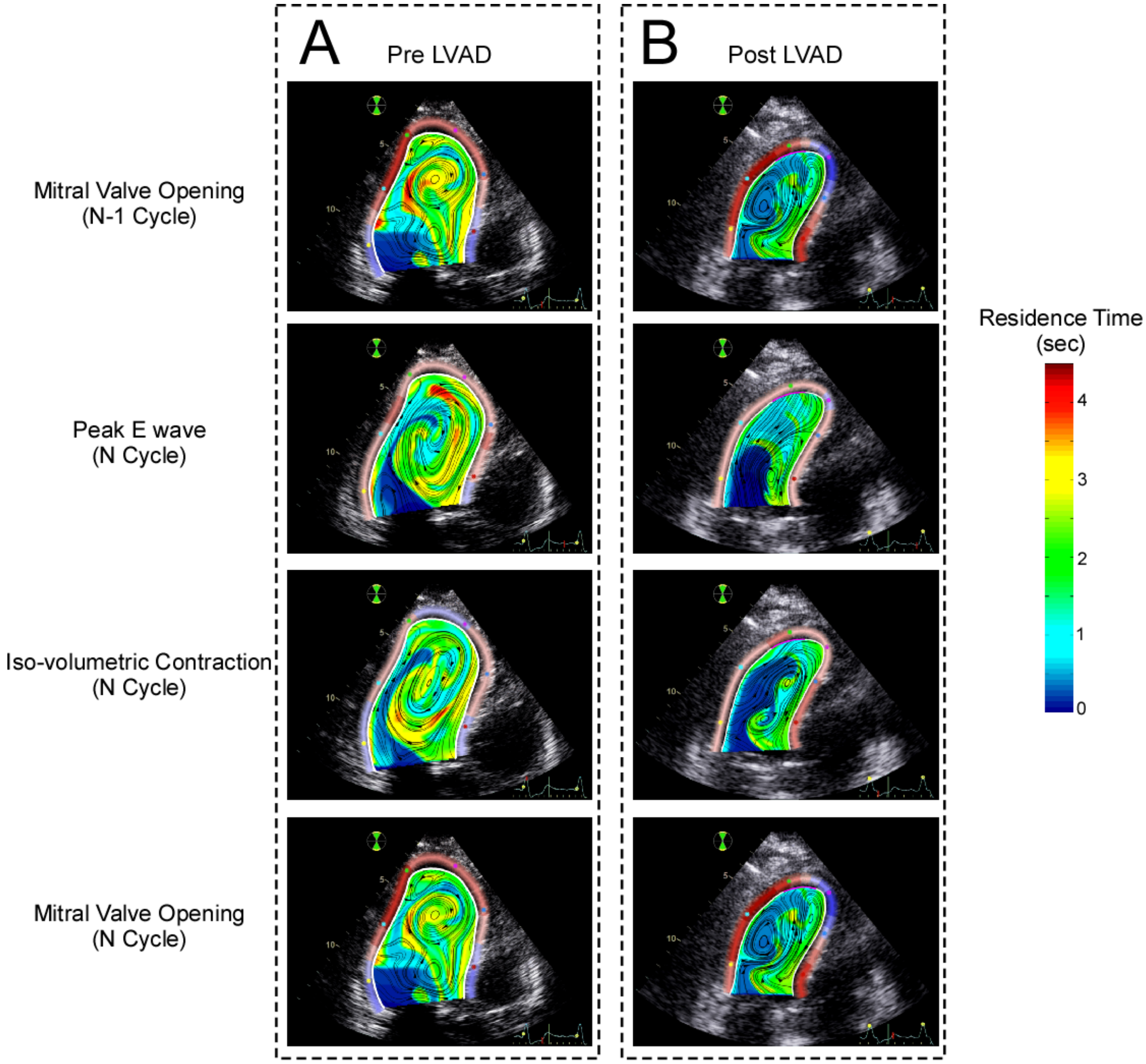

Figure 2.5: Snapshots of 2-D intraventricular residence time along the cardiac cycle in a patient before (A) and after (B) LVAD implantation. The apically located inflow LVAD cannula is represented in magenta. 1st row A: Residence Time mapping at the mitral valve opening in the converged N-1 cycle. 2nd row: Residence Time mapping at E-wave peak in the last computed cycle. 3rd row: Residence Time mapping at the onset of isovolumic contraction in the last computed cycle. 4th row: Residence Time mapping at mitral valve opening in the last cycle.

2.4.4 Simplified Residence Time Indices

An additional challenge to in introducing implement clinically relevant indices of LV blood stasis is to incorporate metrics that integrate the spatio-temporal nature of the T_R distributions, together with additional parameters such as K or T_S, into simple metrics that can be used to compare values between patients. To address this challengeTherefore, we identified Lagrangian clusters of residual volume formed by spatiotemporally connected pixels with $T_R > 2$ sec (Figure 2.6A and supplementary movie 2), and plotted the following indices as a function of time for each Lagrangian cluster:

1. relative LV volume (area in 2D) occupied by each cluster (V_{TR}, Figure 2.6B),
2. spatially-averaged value of T_R in each cluster ($T_{RM,2}$, Figure 2.6C),
3. spatially-averaged value of K in each cluster ($K_{M,2}$, Figure 2.6D), and
4. spatially-averaged value of T_S in each cluster ($T_{SM,2}$, Figure 2.6E).

The temporal profiles of VTR varied periodically, implying that the numerical integration of eq. 1 achieved numerical convergence. Consistent with the instantaneous maps in Figure 2.3, the diseased hearts showed higher values of VTR than the healthy volunteer throughout the cardiac cycle. Remarkably, in the NIDCM cases, the profiles of $T_{RM,2}$ increased from beat to beat, indicating that there is a persistent residual volume of blood that does not mix with incoming blood in these ventricles. Conversely, $T_{RM,2}$ varied periodically for the healthy case, suggesting that blood is not indefinitely trapped in healthy ventricles. Separate analysis of each $T_R > 2$ sec Lagrangian cluster for diseased LVs showed that the apically located residual volume in NIDCM case 2 had significantly higher values of $T_{SM,2}$,and significantly lower values of $K_{M,2}$ than all other residual volumes in NIDCM cases 1 and 2. These data suggest that it is possible to derive simplified indices of stasis from the Doppler-derived spatio-temporal maps of T_R , T_S and K. Furthermore, our results indicate that individual analyses of intraventricular residual volumes help to unmask blood stasis in patients with more than one residual volume region.

To further simplify the potential clinical application of these stasis indices, we considered temporally averaging the time-varying indices defined above for each

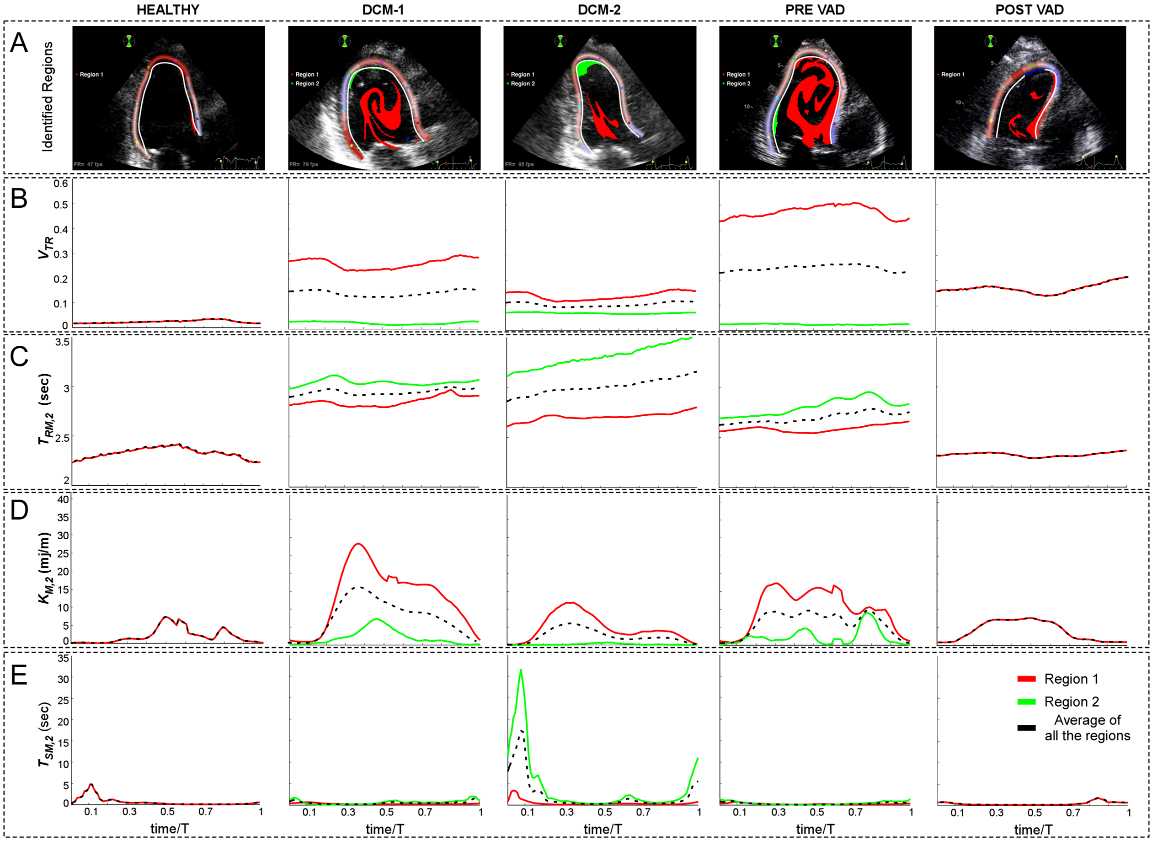

Figure 2.6: Example of region tracking (A) and time evolution of V_{TR} (B), $T_{M,2}$ (C), $K_{M,2}$ (D), $T_{SM,2}$ (E) along the last converged cycle in all the 2-D studied cases: Healthy heart (1st col), NIDCM-1 (2nd col), NIDCM-2 (3rd col), Pre-VAD (4th col) and Post-VAD (5th col). Line colors correspond to each of the tracked regions (row A) and their average (black)

Lagrangian cluster of residual volume. The time-averaged indices are denoted with an overline (e.g. $\overline{V_{TR}}$) and are summarized in Table 2.3 for the subjects analyzed in this pilot study. To facilitate the identification of each cluster, its normalized average apical location, $\overline{X_A}$, is included in the table (0 indicates basal and 1 indicates apical). Despite the small number of cases, we found marked differences in time-averaged stasis indices in patients with NIDCM and healthy volunteers, as well as in the patient with HF before and after LVAD implantation. The values of $\overline{V_{TR}}$ in the diseased LVs ranged between 20% and 50%, much higher than the healthy case which had less than 2.5%. The secular variation of $T_{RM,2}$ in the diseased cases rendered $\overline{T_{RM,2}}$ meaningless in those cases. Conversely, the values of $\overline{K_{M,2}}$ and ($\overline{T_{SM,2}}$) were not relevant in the healthy case and for the secondary residual volumes of cases NIDCM 1, NIDCM2 and the pre-LVAD case, which had insignificant size. Consistent with the results presented in the previous sections, the apical residual volume of NIDCM case 2 had an appreciable size ($\overline{V_{TR}} \approx 7$ %), its value of ($\overline{K_{M,2}}$) was considerably low and its value of $\overline{T_{SM,2}}$ was considerably high. Likewise, in the LVAD patient, $\overline{V_{TR}}$, $\overline{K_{M,2}}$, and $\overline{T_{SM,2}}$ reflect the increase of blood stasis risk near the outflow tract after LVAD implantation.

These results suggest that the time-averaged stasis indices were able to capture the subtle differences in the spatio-temporal stasis patterns found in those two ventricles. Further analysis with larger patient populations and validation with patient outcomes (e.g. incidence of LV thrombus formation) are required to confirm these trends.

2.5 Conclusions and study limitation

In this paper, implement an in vivo method to generate multi-dimensional spatio-temporal maps of LV blood stasis. We also derive simplified patient-specific stasis metrics that integrate these maps and can be used to guide personalized clinical decision-making. This new method is based on the quantification of the residence time spent by blood particles inside the LV since entering the chamber, which is obtained by integrating a transport equation with unit forcing. A residence time threshold can be used to automatically segment and label residual blood volumes that do not mix

Table 2.3: Time-averaged stasis indices for the cases under study. HEALTHY: healthy volunteer; NIDCM: non ischemic dilated cardiomyopathy; LVAD: left ventricle assist device. $\overline{V_{TR}}$: Normalized fraction of chamber volume (Area in 2D) occupied by blood with $T_R > 2$ s, averaged over the cardiac cycle. $\overline{T_{RM,2}}$: Mean residence time in the region with $T_R > 2$ s, averaged over the cardiac cycle. $\overline{T_{SM,2}}$: Mean distortion time scale in the region with $T_R > 2$ sec, averaged over the cardiac cycle. $\overline{K_{M,2}}$: Mean kinetic energy density in the region with $T_R > 2$ s, averaged over the cardiac cycle. $\overline{X_A}$: Normalized average cluster apical location . Subindex 0 denotes the average of all the regions with $T_R > 2$ s.

CASE	N. of residual volumes ($T_R > 2$ s)	Cluster	$\overline{V_{TR}}$ (nor.)	$\overline{T_{RM,2}}$ (sec)	$\overline{T_{SM,2}}$ (sec)	$\overline{K_{M,2}}$ (mJ/m^3)	$\overline{X_A}$	$\overline{V_{TR0}}$ (nor.)	$\overline{T_{RM,2_0}}$ (sec)	$\overline{T_{SM,2_0}}$ (sec)	$\overline{K_{M,2_0}}$ (mJ/m^3)
HEALTHY	1	1	0.023	2.33	0.64	2.0	0.92				
NIDCM-1	2	1	0.26	secular	0.25	13.4	0.43	0.14	Secular	0.34	7.74
		2	0.025	secular	0.43	2.1	0.85				
NIDCM-2	2	1	0.14	secular	0.48	4.8	0.28	0.10	Secular	2.36	2.49
		2	0.068	secular	4.3	0.19	0.86				
PRE-VAD	2	1	0.47	secular	0.28	10.0	0.51	0.25	secular	0.47	4.03
		2	0.023	secular	0.66	2.2	0.40				
POST-VAD	1	1	0.17	secular	0.45	4.0	0.32				

with the fresh blood entering the LV each cardiac cycle, and which are potentially stagnant. By analyzing the kinetic energy and the rate of distortion of each one of these residual volumes we were able to discern if blood is stagnant inside of them. This semi-Lagrangian categorization has been shown to anticipate thrombogenic regions in a pilot study in patients with acute myocardial infarction [15].

To illustrate the residence time mapping methodology, we assessed intraventricular blood stasis in several representative examples. The healthy LV presented residual volumes of small size in comparison to NIDCM patients. Conversely, we often observed large residual volumes inside the persistent swirling flow patterns that develop in dilated LVs [6]. These results are concordant with previous studies based on echo-CDV and PCMRI [10, 18, 19, 35].

Further analysis of the fluid's kinetic energy and rate of distortion suggests that, although the blood inside these residual volumes barely mixes with fresh blood entering the LV each cardiac cycle, it is continuously stirred by the surrounding fluid. Therefore, we conclude that the large swirling flow pattern that develops in dilated LVs does not necessarily induce blood stasis. In addition to this frequent pattern, some diseased LVs had other regions of high residence time that were also associated with low kinetic energy and low rates of distortion, and which were effectively stagnant. Thus, the new method proposed in this paper allows clinicians to assess the degree of intraventricular blood stasis on an individualized basis. Future trials are obviously necessary to address whether this method is suitable to predict the risk of intraventricular thrombosis and, eventually, cardioembolic events. The possibility of Lagrangianly tracking and analyzing each residual volume inside the LV at low computational costs is instrumental for this purpose.

By combining echo-CDV and residence time mapping, we obtained the first quantification of intraventricular blood stasis in patients with LVADs. Our results suggest that intraventricular blood stasis in the LVAD-assisted heart can be higher than prior to implanting the device, particularly near the left ventricular outflow tract, a region reported to be thrombogenic during continuous LVAD support [52]. Mapping methods as the one proposed herein show an excellent potential to correlate stagnant regions with local and global wall motion abnormalities. This type of analysis may be useful in optimally choosing the insertion sites for the LVAD cannulas on a *per-patient* basis.

The proposed methodological framework relies on clinical access to time-resolved LV velocity fields but is independent of the imaging modality employed to measure intraventricular velocity. In this work, we exploited this flexibility to obtain TR maps from both 3D+t PCMRI and 2D+t echo-CDV velocity fields. This allowed us to use each modality to evaluate the limitations of the other, namely the spatiotemporal resolution in PCMRI and the planar flow simplification in echo-CDV. The analysis of residence time maps derived from 3D+t PCMRI showed that both the key spatial features and numerical values of T_R are well represented in the long-axis three-chamber plane imaged by 2D echo-CDV. We performed a sensitivity analysis on echo-CVD data with progressively coarsened spatial and temporal resolutions, concluding that the resolution of the PCRMI velocity fields used in this work was adequate to accurately quantify intraventricular blood stasis. However, we noticed that this method may be sensitive to low-scale velocities. Future clinical studies are needed to optimize the adjustments of the VENC scale (PCMRI) and the Nyquist limit (Doppler) for the purpose of quantifying stasis.

Currently, LV blood stasis is not assessed in the clinical setting. Echo-CDV has important practical advantages, as it is fast, clinically feasible, does not require infusion of contrast agents, and it can be safely performed in patients implanted with LVADs. A limitation of this approach is that it neglects the presence of intraventricular anatomical elements such as papillary muscles and endocardial trabeculae, which can locally increase mixing [7]. This may be particularly important at the endocardial surface, where our approach predicts high residence time values. This limitation could be addressed by including a mass-diffusivity term in eq. (2.1) with a spatially varying coefficient that would need to be determined from high-resolution anatomical imaging. Additionally, there is no doubt that the planar flow simplification may lead to inaccuracies in the estimation of LV blood transport. However, the impact of these and other technical issues needs to be balanced against the potential clinical benefit offered by the new method. In this context, a pilot study suggests that echo-CDV-derived indices of blood stasis may be able to predict LV thrombus formation in patients with acute myocardial infarction [15], a condition in which an individualized assessment of the risk of thrombosis is particularly necessary. If these promising results are confirmed in further trials, it is possible that the clinical information provided by the quantitation of stasis using conventional ultrasound outweighs by far the technical limitations of the method.

In summary, we have implemented a method to quantify and map intraventricular stasis from flow-velocity measurements which is suitable for bedside clinical application. Using this method, important physiological consequences of a number of cardiovascular procedures can now be addressed. Interventions such as valve replacement, resynchronization therapy, correction or palliation of congenital cardiac defects, and surgical ventricular restoration are all known to heavily disturb physiological flow dynamics. Why and to what extent these procedures may impact stasis can be clarified. Spatial, temporal and velocity resolution of current imaging modalities are rapidly increasing, potentially allowing this type of analyses in other cardiac chambers. The final objective of obtaining a reliable individual assessment of the risk of cardiac thrombosis, useful for tailoring anticoagulant therapy and programming cardiac interventions such as LVADs on a patient specific basis, seems therefore achievable in the near future.

2.6 Appendix: Derivation of the residence time equation

In this section, we derive the continuum equation for the residence time of a fluid parcel based on the stochastic analysis of the residence time of its constituent particles. The stochastic derivation is done in 1D without loss of generality. We consider a fluid particle with position, x, which varies as the particle moves with local flow velocity, v, and due to Brownian fluctuations. The Langevin equations for the particle's position and residence time, T, are

$$\frac{dx}{dt} = v + 2\sqrt{k}\xi\left(t\right), \tag{2.2}$$

$$\frac{dT}{dt} = 1, \tag{2.3}$$

where $\xi\left(t\right)$ is a random forcing with a Dirac delta correlation function, and k

is the diffusivity of the fluid particle within the rest of the fluid [26]. From these equations, it is straightforward to derive the Fokker-Planck equation for the probability density function, $p(x, T, t)$,

$$\frac{\partial p}{\partial t} = -\frac{\partial (vp)}{\partial x} - \frac{\partial p}{\partial T} + k\frac{\partial^2 p}{\partial x^2}. \tag{2.4}$$

Notice that the relevant coefficient in equation (2.4) is diffusivity and not the viscosity, as at a microstructural level mass diffusion between two instants of time requires change of position while momentum diffusion requires particle collision, which can occur without change of position. To obtain an equation for the continuum residence time, one can multiply by T equation (2.4), yielding to

$$\frac{\partial Tp}{\partial t} = -\frac{\partial (Tvp)}{\partial x} - T\frac{\partial p}{\partial T} + k\frac{\partial^2 Tp}{\partial x^2}. \tag{2.5}$$

This equation can be integrated in T between $\pm\infty$ to obtain a governing equation for the ensemble average of T,

$$T_R(x,t) = \int_{-\infty}^{\infty} T\ p(x,T,t)\ \mathrm{d}T, \tag{2.6}$$

which is the residence time of the fluid parcel at each position and instant of time.

The only non-trivial term when integrating eq. (2.5) is

$$\int_{-\infty}^{\infty} T\frac{\partial p}{\partial T}\ \mathrm{d}T. \tag{2.7}$$

Equation (2.7) can be handled by parts resulting in

$$\int_{-\infty}^{\infty} T\frac{\partial p}{\partial T}\mathrm{d}T = [Tp]_{-\infty}^{\infty} - \int_{-\infty}^{\infty} p\ \mathrm{d}T = -1. \tag{2.8}$$

It is straightforward to see that the first term in the right-hand-side of equation (2.8) needs to be zero if p is integrable, and that the integral of p must be equal to 1 since p is a probability density function. Thus, combining equations (2.5), (2.6) and

(2.8), one arrives at:

$$\frac{\partial T_R}{\partial t} = -\frac{\partial (vT_R)}{\partial x} - (-1) + k\frac{\partial^2 T_R}{\partial x^2}. \tag{2.9}$$

The mass diffusivity of blood is customarily considered much smaller than its kinematic viscosity, and it is not expected to play an important role in influencing particle trajectories, platelet-surface contact frequency and dissociative binding phenomena under flow at physiological shear rates [22, 45, 54, 58]. Therefore, we set $k = 0$, which is analogous to previous studies of LV blood transport based on the deterministic integration of fluid particle trajectories [35, 83]. Under these premises, equation (2.9) becomes

$$\frac{\partial T_R}{\partial t} + \frac{\partial (vT_R)}{\partial x} = 1, \tag{2.10}$$

which is the 1D analogous of equation (2.1).

2.6.1 An Equation for the Standard Deviation of Residence Time

In a similar way, we can multiply by T^2 equation (2.4) and obtain

$$\frac{\partial T^2 p}{\partial t} = -\frac{\partial (T^2 vp)}{\partial x} - T^2\frac{\partial p}{\partial T} + k\frac{\partial^2 T^2 p}{\partial x^2}. \tag{2.11}$$

This equation can be integrated in T between $\pm\infty$ to obtain a governing equation for S_R, the second moment of T at each position and instant of time:

$$S_R(x,t) = \int_{-\infty}^{\infty} T^2 \; p(x,T,t) \; \mathrm{d}T. \tag{2.12}$$

The only non-trivial term when integrating eq. (2.11) is

$$\int_{-\infty}^{\infty} T^2 \frac{\partial p}{\partial T} \; \mathrm{d}T, \tag{2.13}$$

which can be handled by parts, as done previously, resulting in

$$\int_{-\infty}^{\infty} T^2 \frac{\partial p}{\partial T} \mathrm{d}T = \left[T^2 p\right]_{-\infty}^{\infty} - \int_{-\infty}^{\infty} 2Tp \; \mathrm{d}T = -2T_R. \tag{2.14}$$

This allows to write an evolution equation for S_R:

$$\frac{\partial S_R}{\partial t} = -\frac{\partial (v S_R)}{\partial x} + 2T_R + k_s \frac{\partial^2 S_R}{\partial x^2}. \tag{2.15}$$

Advecting both the second moment S_R and the average residence time T_R we could now obtain for any point in time and space a measure of the standard deviation of the residence time:

$$\sigma_T(x,t) = \sqrt{S_R - T_R^2}. \tag{2.16}$$

2.7 Acknowledgements

Chapter 2, in part, has been published in the *Journal of Biomechanics*. Rossini, Lorenzo; Martinez-Legazpi, Pablo; Vu, Vi; Fernández-Friera, Leticia; del Villar, Candelas Pérez; Rodríguez-López, Sara; Benito, Yolanda; Borja, María-Guadalupe; Pastor-Escuredo, David; Yotti, Raquel; Ledesma-Carbayo, MarÃŋa J.; Kahn, Andrew M.; Ibanez, Borja; Fernández-Avilés Francisco; May-Newman, Karen; Bermejo, Javier; del Álamo, Juan C. 2016. The title of this paper is "A clinical method for mapping and quantifying blood stasis in the left ventricle". The dissertation author was the primary author of this paper.

Chapter 3

A Prospective Study in Acute Myocardial Infarction

3.1 Introduction

Cardioembolic stroke is a major source of mortality and disability worldwide, and blood stasis is the main risk factor for intracardiac thrombosis [1]. In conditions such as atrial fibrillation or left ventricular (LV) systolic dysfunction, impaired blood washout in the heart chambers is thought to facilitate the formation of clots that eventually may dislodge. In-vivo quantification of stasis could be helpful to identify specific flow patterns that predispose to the formation of intracavitary thrombi in cardiac diseases. A variety of flow imaging modalities have become clinically available [7, 10, 24] and it is now possible to accurately analyze the transport of blood using ultrasound or phase-contrast magnetic resonance (MR) [10, 35, 65, 71]. Furthermore, computational studies have shown the potential of blood flow analysis to quantify stasis and thrombogenesis in the heart [35, 69, 71]. Recently, it has become possible to obtain patient-specific maps of stasis in the LV using conventional echocardiography [65]. We hypothesized that this method is useful for quantifying the abnormalities in flow leading to stasis and for obtaining patient-specific metrics of cardioembolic risk.

Acute myocardial infarction (AMI) is an excellent clinical scenario to prospectively test these hypotheses. During the first three months after an anterior-AMI, the incidence of LV thrombosis (LVT) can be as high as 15-20% [27, 76, 81]. Thereafter the prevalence of LVT declines as stunned myocardium recovers after reperfusion. Nevertheless, if systolic dysfunction persists, the risk of cardiac embolism exceeds that of the general population [33]. Hence, sequential studies after AMI allow for addressing the time-evolving interactions among regional myocardial function, intraventricular stasis and mural thrombosis. Additionally, a method for assessing the risk of LVT would be of particular value patients with an anterior-AMI because prophylactic anticoagulation must be balanced against the bleeding risk of triple antithrombotic regimens. The present study was designed to address the clinical potential of an ultrasound-based stasis imaging method in a prospective cohort of patients with an anterior AMI. We aimed to characterize the stasis abnormalities induced by AMI, to elucidate the biomechanical factors that determine stasis, and to test the performance of stasis metrics to predict LVT.

3.2 Methods

3.2.1 Study Population

Seventy-eight consecutive patients admitted to our institution for a first anterior ST-elevation myocardial infarction from July 2013 to January 2016 were prospectively enrolled (Figure 3.1). Inclusion criteria were: 1) sinus rhythm, 2) absence of greater than mild aortic regurgitation (due to methodological limitations for computing the flow velocity field), 3) LV ejection fraction $\leq 45\%$ within the first 72 hours of AMI onset, 4) no previous history of myocardial infarction, 5) stable clinical status, 6) Killip class $<$ IV and 7) willingness to sign the informed consent. Suitable images for processing were unavailable in 5 patients. Thus, this report is based on a cohort of 73 patients with AMI, studied both in the early-phase (within 72 hours of admission) and at 4-5 month follow-up (late phase, Table 3.5). For comparison we enrolled 37 age-matched control subjects (age: 58 ± 11 years old; 40% female) based on the absence of known or suspected cardiovascular disease, normal electrocardiographic and Doppler echocardiographic examinations, and no history of diabetes or hypertension. The institutional review board approved the study, and all participants provided written informed consent.

Table 3.1: Clinical Data of the AMI Cohorts. CAD: coronary artery disease, ACEI/ARB: angiotensin converter enzyme inhibitors/aldosterone receptor blockers. ASA: acetylsalicylic acid. LAD: left anterior descending artery. PCI: percutaneous coronary intervention.

	Full AMI Cohort	Selected AMI Cohort
N	73	37
Age (years)	60 ± 14	59 ± 12
Sex (Female)	17 (23 %)	3 (8 %)
LV mural Thrombosis	15 (20 %)	15 (40 %)
Heart Rate (bpm)	56 ± 10	57 ± 11
Systolic / Diastolic Blood Pressure (mmHg)	117 ± 17/ 69 ± 12	117 ± 16/ 68 ± 11
CAD risk factors		
Hypertension	31 (42 %)	14 (38 %)
Hypercholesterolemia	28 (38 %)	17 (46 %)
Diabetes Mellitus	12 (16 %)	6 (16 %)
Smoking	36 (49 %)	18 (49 %)
Cardiovascular Medications		
Beta-blocker	64 (88 %)	35 (95 %)
ACEI / ARB	63 (86 %)	34 (92 %)
Diuretic	7 (10 %)	37 (100 %)
Statin	73 (100 %)	37 (100 %)
Antithrombotic medication		
Aspirin	72 (100 %)	37 (100 %)
Clopidogrel	23 (32 %)	8 (22 %)
Ticagrelor or Prasugrel	50 (68 %)	28 (76 %)
Coronary Angiography		
Associated non-culprit disease	22 (30 %)	10 (27 %)
Therapeutic Management		
Primary PCI	70 (96 %)	35 (95 %)
Thrombolysis	3 (4 %)	1 (3 %)
No reperfusion therapy	1 (1 %)	1 (3 %)
Additional Revascularization	9 (12 %)	5 (14 %)

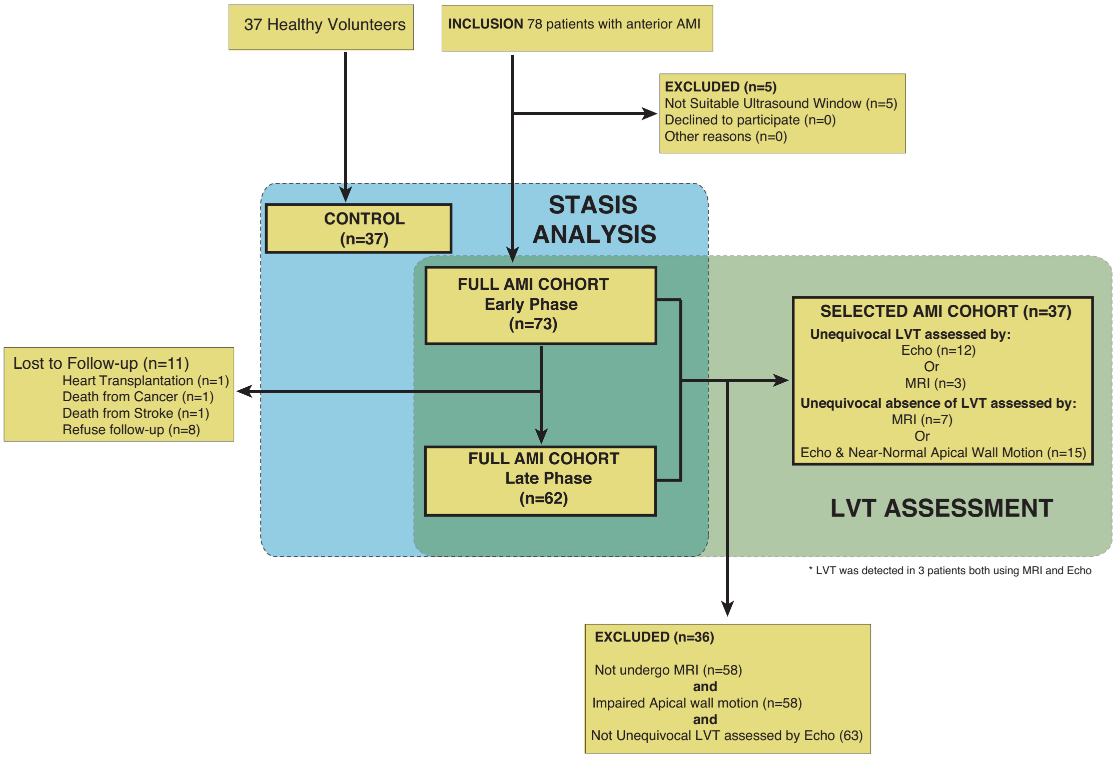

Figure 3.1: Study populations flowchart. We studied 73 patients with AMI at admission (n=73) and after 4-5 months follow-up (n=62) (early & late phases), and 37 healthy volunteers (control group). Given the limited sensitivity of echocardiography to detect LVT, we selected a subset of n= 37 patients from the full-AMI cohort based on unequivocal presence/absence of LVT and near-normal apical wall motion. The full and the selected AMI cohorts were used to test the performance of stasis metrics to predict LVT.

To assess the relationship between stasis metrics and LVT, in addition to ultrasound data we made use of late-enhanced gadolinium MR images from 15 patients undergoing MR scanning at the early (n= 12) or late phases (n= 3) due to additional research studies. We defined LVT positive patients on the basis of unequivocal LVT detection by non-contrast and contrast ultrasound and/or by cardiac MR. We combined these LVT positive patients with two different LVT negative AMI groups to define the full and selected AMI cohorts (Figure 3.1 & Table 3.5). In the full AMI cohort, all non-LVT positive AMI patients were considered as LVT negative. However, due to the limited sensitivity of B-mode echocardiography to detect LVT [79, 80], we defined a subset of the full AMI cohort (selected AMI cohort), based on:

1) a LVT negative MR scan or 2) a LVT negative ultrasound examination which also showed normal or near-normal apical wall motion. The latter was defined as apical wall-motion scores < 5 (conventional B-mode) and < 7 (contrast echocardiography), since these cutoffs exclude LVT in the setting of an anterior myocardial infarction [80].

3.2.2 Image Acquisition and Analysis

Echocardiographic examinations were performed using a Vivid 7 scanner and phase-array 2-4 MHz transducers (GE Healthcare). Three-dimensional sequences were obtained from apical views to ensure complete apical visualization without foreshortening and used to measure LV volumes and ejection fractions. Contrast-echo sequences were obtained in the AMI cohort (intravenous Sonovue, Bracco Imaging, 1-2 mL; pulse inversion imaging; mechanical index < 0.3). Two level-3 experts in echocardiography blindly analyzed the presence/absence of LVT in the AMI group as well as apical regional wall motion. LV sphericity was calculated as the short axis to long axis ratio. Longitudinal and transversal myocardial strain and strain-rate were measured from apical long-axis sequences using a 6-segment model (EchoPac version 110.1.2, GE Healthcare). The ratio between the E-wave velocity time integral and the LV length (E-Wave propagation index) was also measured [34].

3.2.3 Magnetic Resonance Imaging

Fifteen AMI patients underwent late-enhancement gadolinium MR scanning (Philips Achieva 1.5T) at the early (n= 12) or late phases (n=3) due to additional research studies. The MR imaging protocol included a cine steady-state free precession imaging of LV function (SENSE X 2, repetition time: 2.4 ms, echo time: 1.2 ms, average in-plane spatial resolution: 1.6 x 2 mm, 30 phases per cycle, 8-mm slice thickness without gap) and late enhancement imaging (3D inversion-recovery turbo gradient echo sequence, pre-pulsed delay optimized for maximal myocardial signal suppression; 5-mm actual slice thickness, inversion time: 200-300 and 600 ms). Images were obtained in short axis (10 to 14 contiguous slices) and 4-, 2-, and 3-chamber views. Late enhancement was performed 3 to 10 min after injection of 0.1 mmol/Kg of gadobenate dimeglumine (MultiHance, Bracco Imaging).

3.2.4 Stasis Imaging and Mapping

We used color-Doppler velocimetry (Echo-CDV) to obtain the unsteady two-dimensional (2D+t) flow field as previously described [6, 24, 50] (Figure 3.2). For this purpose, we acquired consecutively color-Doppler sequences of 8 to 14 beats, followed by a 2D cine-loop (4 beats) at high frame-rate without moving the probe. Echo-CDV provides the cross-beam flow velocity by integrating the continuity equation under a planar flow assumption, imposing a condition of non-flow penetration at the myocardium-blood interface. The technique has been validated in vitro [24] and in vivo [6].

We defined residence time as the time spent by a blood particle before it leaves the chamber. We have previously shown that spatio-temporal maps of residence time can be efficiently obtained in the LV from 2D+t echo-CDV data by integrating the equation of advection of a passive scalar with unit forcing [65]. We solved this equation for 8 consecutive cardiac cycles to ensure temporal convergence (Figure 3.2). From the residence time maps, we calculated the average residence time of the entire blood volume inside the LV. This is a representative metric of global stasis that accounts for the full blood pool in the ventricle. However, local stasis metrics may be particularly meaningful for mural thrombosis. Therefore, we also identified and tracked blood regions with a residence time ≥ 2 s, hereinafter defined as stagnant regions.

Blood clusters with residence time > 2 seconds were defined as stagnant regions. The basis of this threshold is the well-accepted decomposition of LV blood volumes based on their transit [7, 10]: direct flow (blood volume that enters and exits the LV in the same cardiac cycle), retained inflow (incoming blood volume that is not ejected during the same cycle), delayed ejection (ejected blood volume that entered the LV in a previous cardiac cycle) and residual volume (blood volume that entered the LV in a previous cycle and is not ejected in the current cycle, therefore residing in the LV for at least two cardiac cycles). Thus, if the residence time of a blood particle is > 2 seconds ≈ 2 cardiac cycles, then it belongs to the residual volume pool and it is stagnant. Note that the existence of small stagnant regions that remain in the

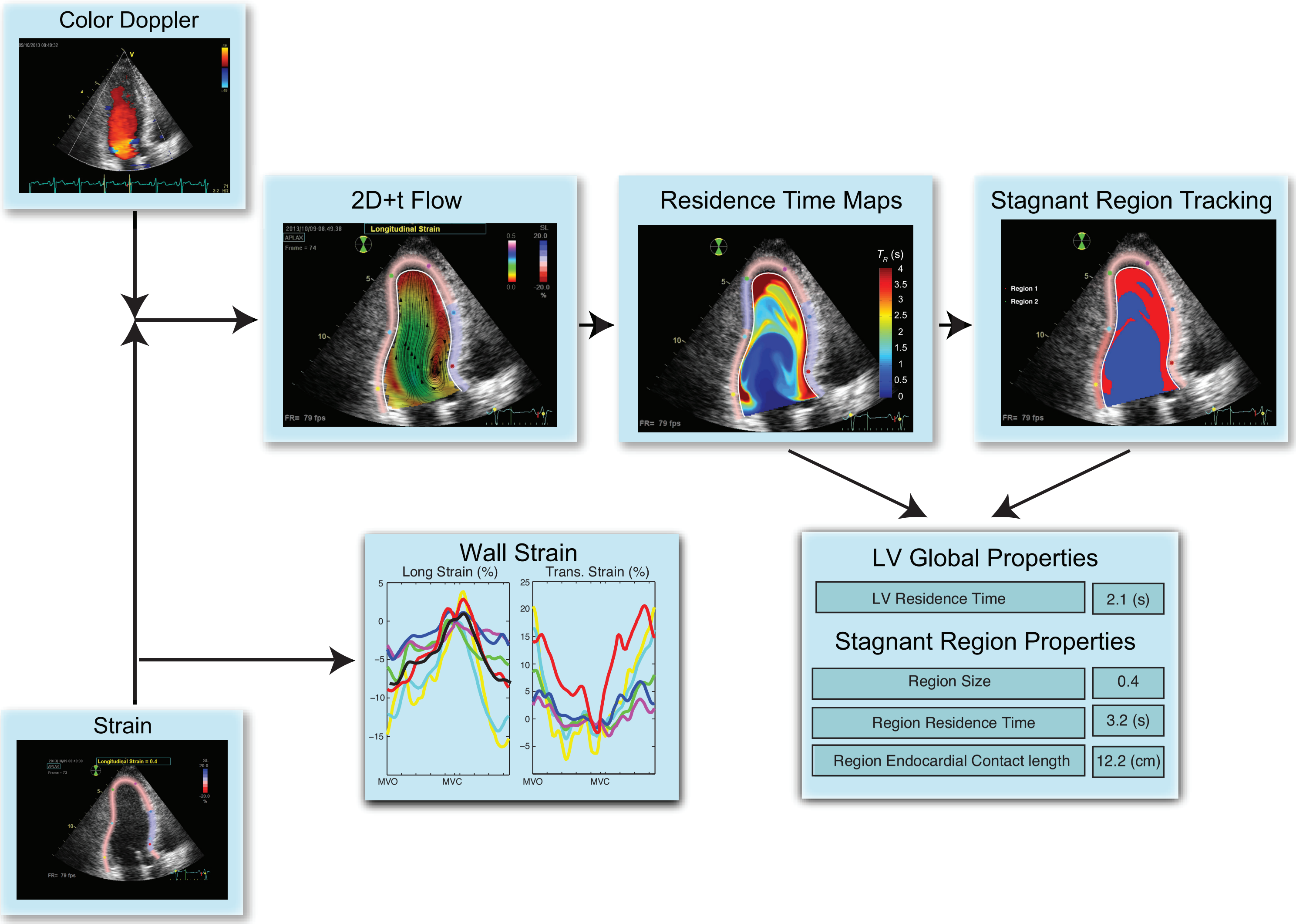

Figure 3.2: Methodology. Methods used for image acquisition and processing. 2D+t: unsteady 2-dimensional.

LV for periods > 2 s may be physiological in the normal heart and is not per-se an indicator of increased thrombogenesis risk.

We measured the following features of these stagnant regions: 1) size relative to total LV volume (area in 2D) (dimensionless), 2) mean residence time (in seconds), and 3) perimeter of contact with the endocardium (in cm). The contact perimeter of stagnant regions with the endocardium accounts for flow-endocardium interactions that most intensively activate the coagulation cascade [69]. The features of stagnant regions were automatically measured at the instant of mitral valve opening. Stagnant regions not spanning a full cardiac cycle or $< 2\%$ of LV area were dismissed, and whenever more than one region were identified, only the one closest to the apex was analyzed.

Additionally, the time and perimeter metrics were normalized with the period of the cardiac cycle and total endocardial length respectively, in an effort to derive dimensionless stasis metrics less sensitive to heart rate and LV size (see Table 3.6). The test-retest reproducibility of stasis metrics was good (intraclass correlation coefficient > 0.75 for most indices; Table 3.2).

We analyzed the two-dimensional evolution of the filling E-wave with respect to the LV lateral wall and its effect on blood stasis. To this end, we categorized filling jets as wall jets or free jets depending on whether they impinged or not on the inferolateral wall (2 independent observers). This categorization is standard in fluid mechanics [82].

3.2.5 Statistical Analysis

Apical strain was computed by averaging the values from the mid-anteroseptal, apical-septal and apical-inferior segments. Variables are described as mean ± standard deviation unless otherwise specified. Proportions were compared using chi-squared tests. Quantitative variables were analyzed using paired and unpaired t-tests where appropriate. To analyze the determinants of stasis we pooled the control, early AMI and late AMI cases (n= 172). We used Pearson linear correlation and multiple linear regression analyses (backwards stepwise regression based on Alkaike's information criterion, ruling-out significant interactions as well as collinearities based on

Table 3.2: Intra-class correlation coefficient (R_{ic}) and relative error (mean ± std) of the reproducibility study (fully blinded echocardiographic image re-acquisition by two independent observers in n = 8 control subjects, including re-calculation of 2D+t flow velocity fields and residence time, event-time identification and final computation of stasis indices).

Parameter	Intraobserver		Interobserver	
	R_{ic}	Relative Error (%)	R_{ic}	Relative Error (%)
Average residence time in the LV (s)	0.77	3 ± 25	0.82	18 ± 29
Size of stagnant regions (dimensionless)	0.78	17 ± 43	0.75	30 ± 45
Residence time of the stagnant regions (s)	0.85	2 ± 14	0.71	1 ± 21
Endocardial Contact length of stagnant regions (cm)	0.79	-11 ± 18	0.89	4 ± 19

Table 3.3: Pearson correlation coefficient among the different indices of stasis. All correlations were significant with $p < 0.001$

	Size of stagnant regions (dimensionless)	Residence time of the stagnant regions (s)	Endocardial Contact length of stagnant regions (cm)
Average residence time (s)	0.91	0.81	0.61
Size of stagnant regions (dimensionless)		0.56	0.70
Residence time of the stagnant regions (s)			0.45

the variance inflation factor). We calculated receiver-operating characteristic curves (ROC) to assess the diagnostic performance of stasis indices to predict LVT in the full and the selected AMI cohorts. Sensitivity, specificity, positive predictive values (PPV) and negative predictive values (NPV) were calculated based on cutoffs derived from the ROC analyses. Bias corrected and adjusted 95% intervals of ROC parameters were obtained by bootstrapping of 2,000 replicates. Two sets of cut-off values were selected: 1) to maximize the negative predictive value as recommended when a second-step confirmatory examination, i.e. late gadolinium-enhanced MR, is available, and 2) to maximize diagnostic performance. Statistical significance was established at the $p< 0.05$ level (R version 3.2).

3.3 Results

3.3.1 Clinical Data and Convential Echocardiography

Seventy patients (96%) were acutely treated by percutaneous coronary intervention, 3 (4%) received thrombolytic therapy, and 1 (1%) did not receive reperfusion therapy. All patients except one received dual antiplatelet therapy of aspirin and clopidogrel (23,32%), ticagrelor or prasugrel (50, 68%). Patients diagnosed of LVT received oral anticoagulation. Two patients died during follow-up. One patient suffered a fatal acute stroke during early admission without LVT being identified in the early echocardiography study. The other one died of cancer two months after inclusion. One patient underwent heart transplantation, and 8 patients were lost to follow-up. Thus, late-phase imaging data was available in 62 (85%) patients at a median (Q1 - Q3) follow-up period of 4.6 (3.7 - 5.3) months (Figure 3.1). LVT was diagnosed in 15 (20%) patients, 12 and 3 of them in the early and late studies, respectively. These 15 patients were defined as the LVT positive group. The selected cohort was composed of the 15 LVT-positive patients, $n= 7$ LVT-negative by MR, and $n= 15$ LVT-negative by conventional and contrast-echocardiography showing normal or near normal apical wall-motion (Figure 3.1).

Compared to controls, AMI patients in the early phase showed larger LVs and lower values of ejection fraction and apical strain, as expected (Table 3.4). From the

Table 3.4: Conventional Ultrasound Data of the Full AMI Cohort and the Control Population. *: $p < 0.05$ Early AMI vs Control, \$: $p < 0.05$ Early AMI vs Late AMI and #: $p<0.05$ Late AMI vs Control.

	Early AMI	Late AMI	Control
End-diastolic volume index (mL/m2)	57 ± 13$^{\$,*}$	63 ± 21$^{\#}$	46 ± 8
End-systolic volume index (mL/m2)	32 ± 10*	32 ± 16$^{\#}$	17 ± 4
LV Ejection fraction (%)	43 ± 9$^{\$,*}$	52 ± 10$^{\$,\#}$	63 ± 5
End-diastolic diameter (cm)	4.7 ± 0.6*	4.8 ± 0.6$^{\#}$	4.4 ± 0.4
End-systolic diameter (cm)	3.5 ± 0.7*	3.6 ± 0.6$^{\#}$	3.1 ± 0.4
LV mass index (g/m2)	97 ± 22*	94 ± 22$^{\#}$	69 ± 13
LV Sphericity	0.55 ± 0.07	0.55 ± 0.07	0.55 ± 0.07
Apical Peak Transversal Strain (%)	12.2 ± 9.3$^{\$,*}$	18.7 ± 11.3	21.1 ± 23.5
Apical Peak Longitudinal Strain (%)	-10.2 ± 4.3$^{\$,*}$	-16.4 ± 6.2$^{\#}$	-20.6 ± 4.1
LV filling wall jet [n (%)]	34 (47%)	35 (57%)	12 (32%)

early to the late-phase studies of the AMI cohort, EF improved from 43 ± 9 to 52 ± 10% ($p < 0.001$). Apical strain also improved significantly during follow-up, although longitudinal strain remained significantly lower than in the control group (Table 3.4).

3.3.2 Stasis Imaging

Global residence time was $> 37\%$ higher in the early phase of AMI (full AMI cohort) than in controls (2.2 ± 0.8 s vs. 1.6 ± 0.7 s, $p = 0.001$), subsequently improving in late-phase studies (1.9 ± 0.8 s, $p = 0.009$ vs. early-phase; Table 3.5 and Figure 3.3). Features of stagnant regions were also different in the early AMI studies than in controls. In particular, stagnant regions were larger (0.38 ± 0.17 vs. 0.27 ± 0.2, $p = 0.003$), with longer regional residence times (4.0 ± 1.0 vs. 3.6 ± 1.5 s, $p = 0.04$), and with an average 3 cm longer perimeters of endocardial contact (11.3 ± 3.2 vs 8.3 ± 2.4 cm, $p < 0.001$). The stasis metrics improved towards control values in follow-up studies of AMI patients, and only the perimeter of endocardial contact remained significantly above control values (9.6 ± 4.2 cm, $p = 0.04$). Correlation among the indices of stasis is shown in Table 3.2. Normalized dimensionless metrics of stasis followed similar trends (Table 3.3).

Table 3.5: Stasis Mapping Data of the Full AMI Cohort and the Control Population. *: $p < 0.05$ Early AMI vs Control, \$: $p < 0.05$ Early AMI vs Late AMI and #: $p < 0.05$ Late AMI vs Control.

LV Global Stasis	Early AMI	Late AMI	Control
Average residence time (s)	$2.2 \pm 0.8^{\$}$,	1.9 ± 0.8	1.6 ± 0.7
Regional Stasis			
Size of stagnant regions (dimensionless)	$0.38 \pm 0.17^{\$}$,	0.32 ± 0.20	0.27 ± 0.21
Residence time of the stagnant regions (s)	$4.0 \pm 1.0^{\$}$,	3.7 ± 1.0	3.6 ± 0.9
Endocardial contact length of stagnant regions (cm)	$11.3 \pm 3.2^{\$,*}$	$9.6 \pm 4.2^{\#}$	8.3 ± 2.4

Table 3.6: Stasis Mapping Data of the Full AMI Cohort and the Control Population. For this table, average residence is expressed in terms of the number of cardiac cycles and regions of stasis defined as blood regions lasting longer than two beats. Endocardial contact length of stagnant regions is expressed in relative terms to total endocardial perimeter. *: $p < 0.05$ Early AMI vs Control, \$: $p < 0.05$ Early AMI vs Late AMI and #: $p < 0.05$ Late AMI vs Control.

LV Global Stasis	Early AMI	Late AMI	Control
Average residence time (cycles)	$2.6 \pm 0.9^{\$,*}$	1.8 ± 0.8	1.7 ± 0.9
Regional Stasis			
Size of stagnant regions (dimensionless)	$0.44 \pm 0.15^{\$,*}$	0.30 ± 0.2	0.27 ± 0.16
Residence time of stagnant regions (cycles)	$4.4 \pm 1.1^{\$,*}$	3.6 ± 1.0	3.8 ± 1.1
Endocardial contact length of stagnant regions (dimensionless)	$0.67 \pm 0.14^{\$,*}$	0.59 ± 0.21	0.58 ± 0.13

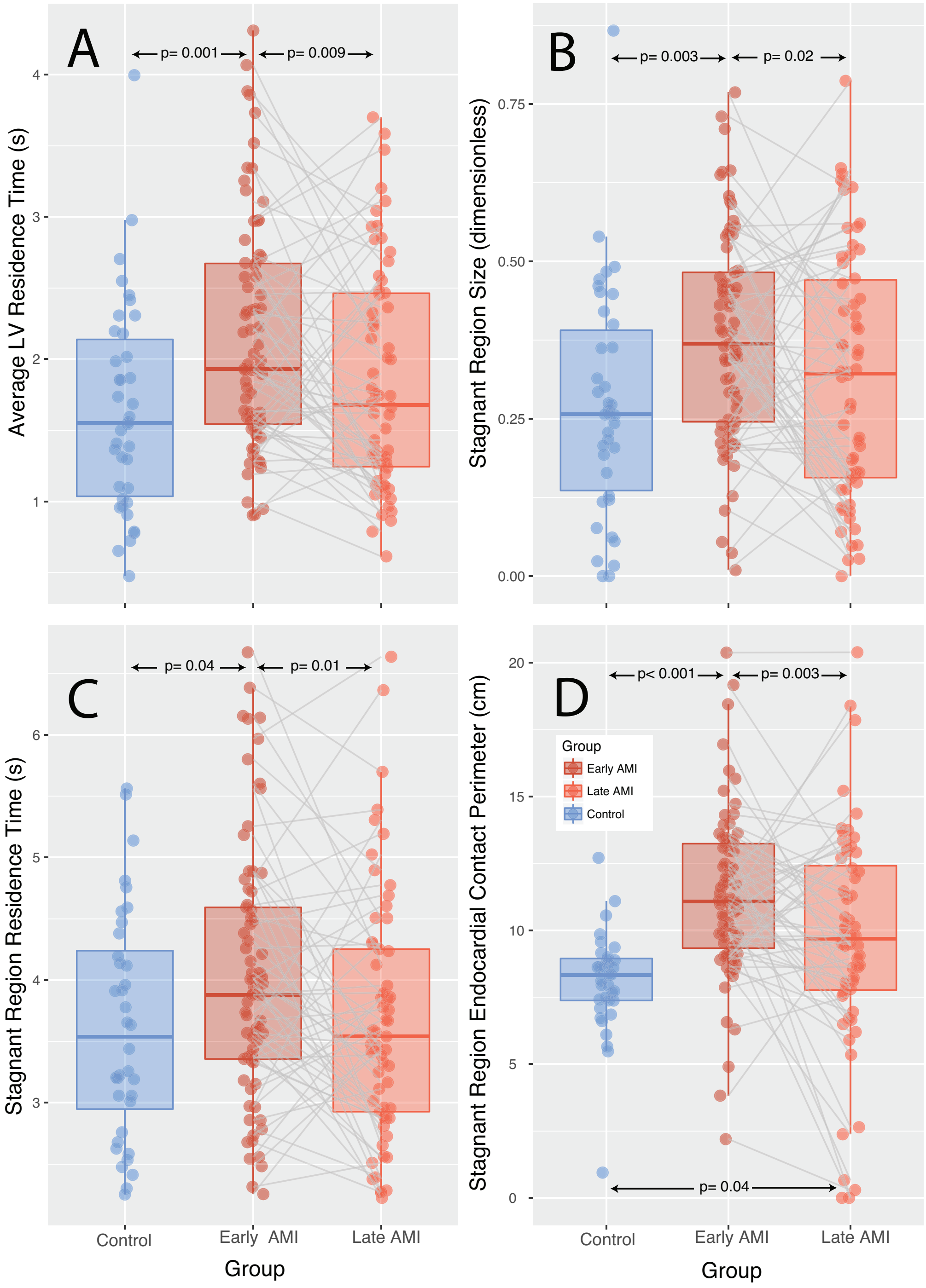

Figure 3.3: Stasis Imaging. Boxplots and scatterplots of stasis indices for the control group (blue) and the AMI patients at the early (dark red) and late phases (light red). A: Average residence time (s). B: Size of the stagnant regions (dimensionless). C: Average residence time of the stagnant regions (s). D: Endocardial contact length of stagnant regions (cm).

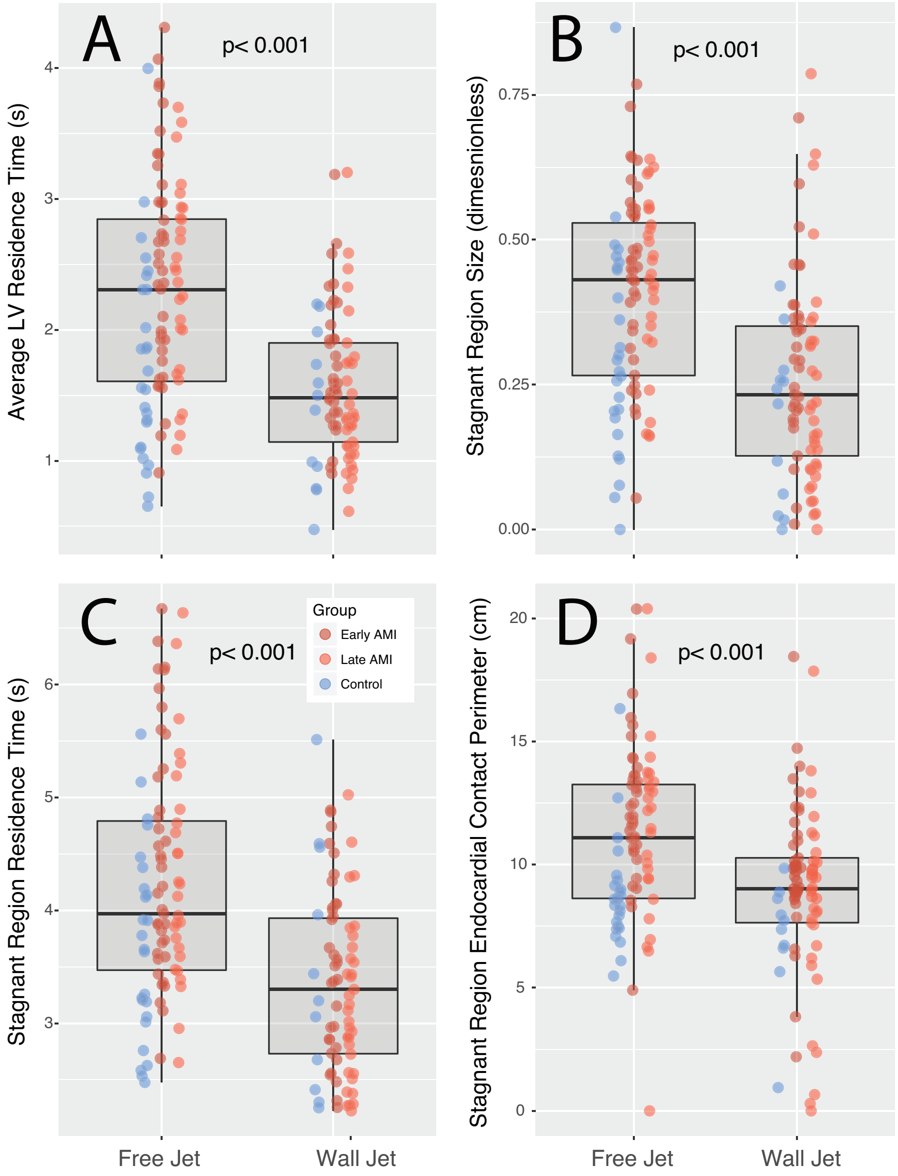

Figure 3.4: Wall Jet & Stasis. Scatterplots and boxplots of stasis indices (pooled early, late and control studies) with and without wall filling jets. Controls are depicted in blue whereas the AMI patients at the early and late phases are shown in dark red and light red, respectively. A: Average residence time (s). B: Size of the stagnant regions (dimensionless). C: Average residence time of the stagnant regions (s). D: Endocardial contact length of stagnant regions (cm).

Table 3.7: Determinants of Stasis. Analysis performed using pooled data from early and late AMI as well as controls studies (n= 172). EF: Ejection Fraction, ESVI: End-Systolic Volume index, SVI: Stroke Volume index, Long Strain: Peak Longitudinal Strain. EPI: E-wave propagation index.

	Average residence time (s)					Endocardial contact length of stagnant regions (cm)				
	Univariate		Multivariate			Univariate		Multivariate		
	R	p	β	std-β	p	R	p	β	std-β	p
Heart Rate	0.12	0.12	-	-	-	-0.11	0.15	-	-	-
EF	-0.24	0.002	1.23	0.17	0.17	-0.49	< 0.001	2.8	0.08	0.43
ESVI	0.27	< 0.001	0.01	0.22	0.02	0.57	< 0.001	0.13	0.48	< 0.001
SVI	0.01	0.80	-	-	-	0.05	0.50	-	-	-
Long Strain	0.34	< 0.001	0.03	0.21	0.03	0.52	< 0.001	0.15	0.28	0.003
EPI	-0.34	< 0.001	-0.47	-0.15	0.06	-0.40	< 0.001	-1.2	-0.09	0.21
Wall Jet		< 0.001	-0.72	-0.44	< 0.001		< 0.001	-2.4	-0.34	< 0.001
			Global R^2_{adj}: 0.60; $p< 0.001$					Global R^2_{adj}: 0.71; $p<0.001$		

3.3.3 Determinants of Stasis

By univariate analyses the EF, end-systolic volume index, apical longitudinal strain and the E-wave propagation index correlated with global and regional indices of stasis (n= 172 pooled control, early and late full AMI cohort studies; Table 3.7). However, it is important to note that all stasis metrics were significantly worse in ventricles without a filling wall jet (Figure 3.4). Detailed inspection of stasis movies showed that filling wall jets readily propagated apically transporting fresh blood towards the apex. By multivariate regression, the absence of a filling wall jet and the end-systolic volume were the main determinants of the global residence time ($std-\beta$ = -0.44, p< 0.001 and $std-\beta$= 0.22, p= 0.02, respectively) and endocardial contact of the stasis region ($std-\beta$ = -0.34, p< 0.001 and $std-\beta$ = 0.48, p< 0.001, respectively), whereas apical strain also had a significant impact on both indices of stasis (Table 3.7).

3.3.4 Stasis and Mural Thrombosis

In early-phase studies of the full AMI cohort, the 15 LVT-positive patients had significantly different stasis metrics than the 47 LVT-negative patients (Figure 3.5). Values of global residence time were higher in LVT-positive patients (2.7 ± 0.9 vs. 2.0 ± 0.8 s, p= 0.01). LVT-positive patients also showed larger regions of stasis (0.50 ± 0.15 vs 0.36 ± 0.16, p= 0.01), with higher regional residence times (4.6 ± 1.0 vs 3.9 ± 1.0 s, p= 0.02) and longer endocardial contact perimeters (13.0 ± 3.1 vs 10.8 ± 3.1 cm, p= 0.02) than the LVT-negative patients. Similar results were obtained when only the selected cohort was analyzed (Figure 3.5).

The diagnostic performance of regional stasis metrics to predict early or late LVT was favorable. Overall area under the ROC curve was 0.73 (bias corrected and adjusted 95% confidence interval: 0.61 - 0.86) for the global residence time and 0.69 (95% CI: 0.54 - 0.83) for endocardial contact perimeter of stagnant regions in the full cohort (Table 3.8 and Figure 3.6). Respective values were 0.80 (95% CI: 0.66 - 0.94) and 0.69 (95% CI: 0.51 - 0.86) in the selected cohort. The highest sensitivity was found for cutoff values of 1.6 s for the global residence time and 9.0 cm for the endocardial contact length of the stagnant region (Table 3.8). Representative examples of AMI

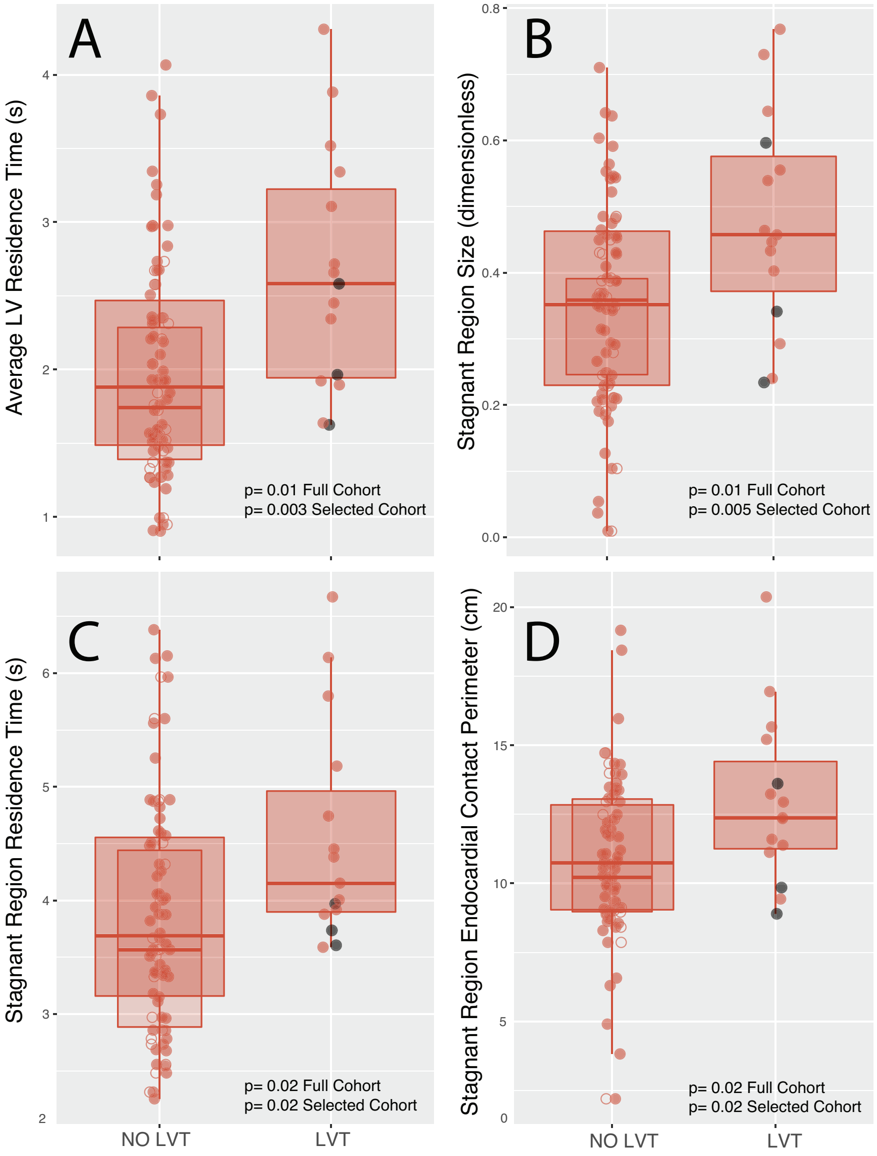

Figure 3.5: Stasis & LVT. Boxplots and scatterplots of stasis indices of early-phase studies of the AMI cohort, with and without LVT. Patients form the selected cohort are represented by empty dots and the narrow boxes. Black dots show the three patients who showed LVT in the late but not in the early-phase study. A: Average residence time (s). B: Size of the stagnant regions (dimensionless). C: Average residence time of the stagnant regions (s). D: Endocardial contact length of stagnant regions (cm).

patients with and without LVT are shown in Figure 3.7.

3.4 Discussion

To our knowledge, this is the first prospective study addressing the clinical potential of functional stasis imaging. We demonstrate that objective indices of ventricular stasis can be derived from bedside echocardiography and we describe important blood transport abnormalities in patients after an anterior AMI. We also show that stasis imaging sensitively captures the improvement in blood washout that follows wall motion recovery. Furthermore, we identified biomechanical factors predisposing to stasis. Thus, stasis imaging techniques provide new insights into cardiac physiology and may be useful to measure cardioembolic risk.

3.4.1 Stasis as an Index of Cardiac Physiology

Avoidance of blood retention in the normal LV is the consequence of complex transport dynamics taking place during systole and diastole. Intuitively one could assume that blood in the LV follows a first-in-first-out transit but not even the normal ventricle works this way. A portion of the blood volume entering the LV exits the chamber during the ensuing systole, whereas other portions are retained [10]. The size, location and persistence of these remnant fractions are conditioned by complex interactions among the entering blood, the valves, the myocardial wall and the volume already present in the ventricle. It is the spatiotemporal coordination of these processes that determines the degree of stasis and washout. The lack of methods for visualizing and quantifying stasis has limited studying blood volume interplay and transport phenomena in the clinical setting. Initial studies using MR laid the foundations for understanding blood transport in the heart, but the analyzed time span was too short to address stasis [10]. In the recent years, several methods for tagging, tracking and quantifying blood transport have been optimized for longer periods [65, 69]. Residence time is an intuitive metric to assess global and regional stasis in the heart [35, 65]. Using this metric cardiac hemodynamics can be evaluated not only in terms of mechanical energy and force but also of avoidance of blood retention.

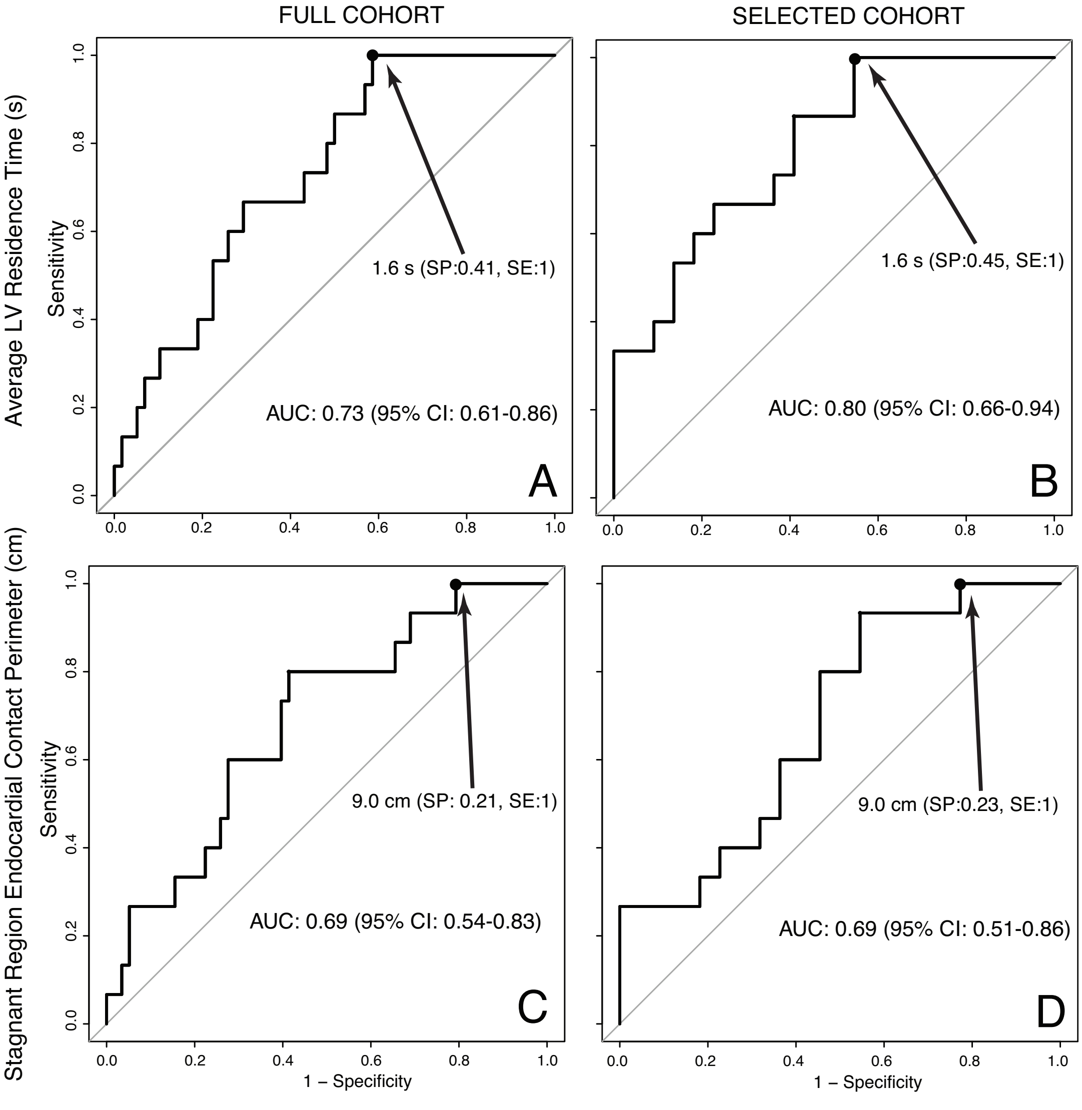

Figure 3.6: ROC analyses. Receiver operating characteristic (ROC) curves for the average residence time (A & B) and the endocardial contact length of stagnant regions (C & D) for the diagnosis of LVT. Full AMI Cohort: A & C. Selected AMI cohort: B & D.

Table 3.8: Receiver-operating characteristic curves (ROC) analysis of stasis metrics to predict LVT in AMI subjects. In parantheses: 95 % CI; PPV: positive predictive value; NPV: negative predictive value.

		Full AMI Cohort				Selected AMI Cohort			
	Thres.	Specificity	Sensitivity	PPV	NPV	Specificity	Sensitivity	PPV	NPV
Average residence time (s)	1.6	0.41 (0.29-0.55)	1 (1-1)	0.31 (0.27-0.37)	1 (1-1)	0.45 (0.23-0.68)	1 (1-1)	0.55 (0.47-0.68)	1 (1-1)
	1.9	0.5 (0.36-0.62)	0.86 (0.67-1)	0.31 (0.24-0.38)	0.94 (0.85-1)	0.59 (0.41-0.77)	0.87 (0.67-1)	0.59 (0.48-0.75)	0.94 (0.71-1)
Endocardial contact length of stagnant regions (cm)	9.0	0.21 (0.10-0.31)	1 (1-1)	0.25 (0.22-0.27)	1 (1-1)	0.23 (0.09-0.41)	1 (1-1)	0.46 (0.43-0.54)	1 (1-1)
	11.1	0.59 (0.47-0.71)	0.80 (0.6-1)	0.33 (0.25-0.42)	0.92 (0.83-1)	0.54 (0.32-0.73)	0.80 (0.6-1)	0.55 (0.43-0.68)	0.80 (0.61-1)

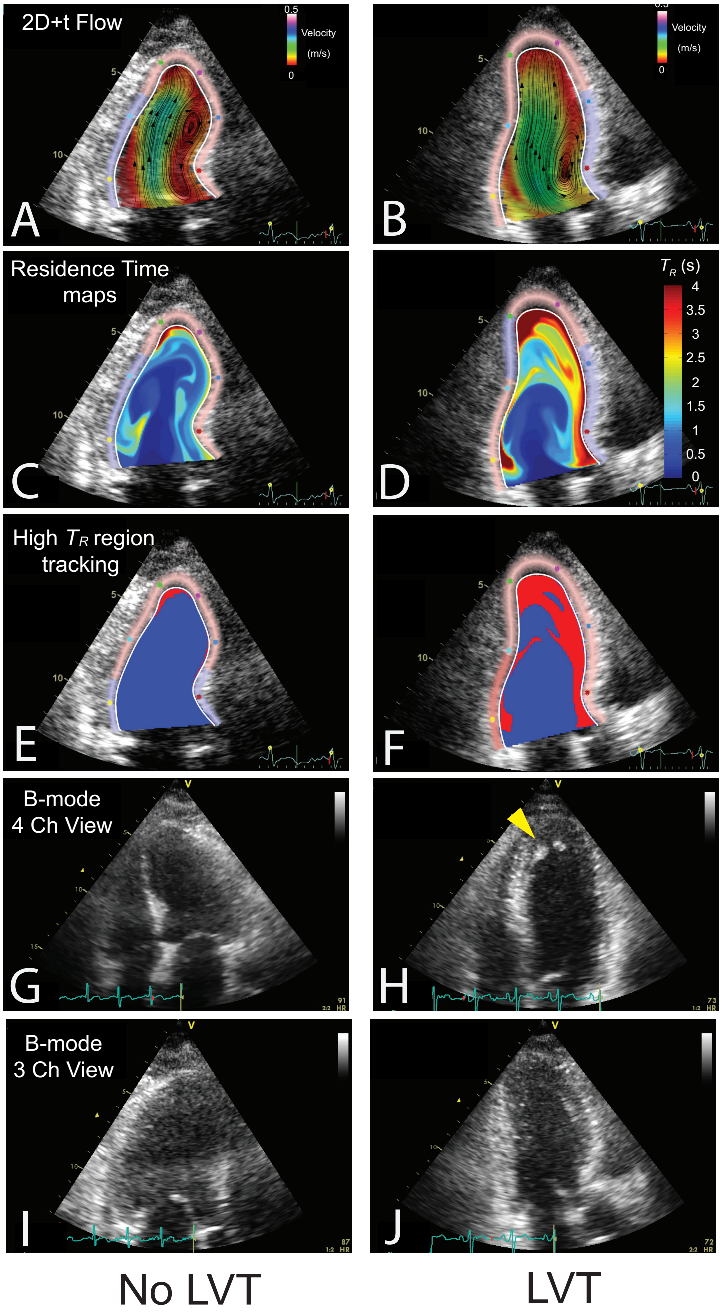

Figure 3.7: Examples. Patient without (A, C, E, G, I) and with LVT (B, D, F, H, J). A-B: 2D+t Flow maps. C-D: Residence time maps in the last beat. E-F: Segmentation and tracking of stagnant regions. G-H: B-Mode 4-chamber view. I-J: B-Mode 3-chamber view. Yellow arrowhead: apical thrombus.

3.4.2 Myocardial Function and Stasis

In AMI, impaired wall motion and/or LV remodeling may disturb the physiological flow trajectories that facilitate blood washout [6, 7, 50, 60, 65]. Increased blood spontaneous contrast is a classical echocardiographic sign of stasis [81] and apical regional wall motion is closely related to mural thrombosis [80]. In the present study we elucidate these empirical observations using quantitative stasis metrics and we describe the changes in flow that take place upon the recovery of myocardial function. Our results show that factors beyond wall motion [80] and apical flow propagation [34] impair blood washout. Flow-mediated factors may also explain why conventional indices of LV function such as EF are limited to guide preventive anticoagulation [38].

Avoidance of blood retention is believed to be one of the teleological advantages of the complex flow patterns observed in the human heart [7]. The vortex ring that develops during diastole has a prominent role in transporting blood and is a major contributor to filling [50, 66]. As the ventricle dilates, although the vortex grows, its propagation along the long axis decreases, diminishing its interaction with apical blood [6]. Recent studies in AMI have associated LVT to the degree of apical propagation of the filling column [34], as well as to the location and pulsatility of the LV vortex [56, 71]. In our study, we demonstrate that the orientation of the filling jet is also a major determinant of stasis. Compared to patients with free filling jets, we found improved washout in patients in whom the inflow jet is oriented towards the inferolateral wall. The trajectory of the filling jet is related to LV inflow tract geometry, the magnitude of the diastolic intraventricular pressure gradients [88] and the degree of remodeling. In theory, particular LV configurations may idiosyncratically promote or protect against stasis. In addition, inflow redirection could be an unreported mechanism promoting intraventricular thrombogenesis after mitral valve replacement. Further 3-dimensional geometrical analyses are warranted to address these issues.

Hypothetically, stagnant regions may activate blood clotting without macroscopic wall thrombosis ever being detected, either because a small mural thrombus is missed, or because the thrombotic material embolizes before imaging. In fact, transcranial Doppler has recorded microembolisms in as many as 25% of patients during

AMI [55]. These microembolisms are not clinically meaningful in most cases, but such a high incidence rate emphasizes the need of further investigation in this setting. Methods to quantify stasis as the one herein proposed are particularly promising for this purpose. In addition to stasis, local and systemic factors (e.g. endocardial disruption and inflammation) also contribute to thrombogenesis and these additional factors could account for the moderate positive predictive value we observed in our study. However importantly, these local and systemic factors can be combined with stasis metrics to obtain composite biomarkers of thrombotic risk [69, 71].

3.4.3 Limitations

LV flow is intrinsically three-dimensional but for the present study we used a 2D based approach. Although a planar flow simplification may lead to inaccuracy, 2D methods have important practical advantages. First, computational requirements are markedly reduced when implemented in 2D [65]. And second, ultrasound-based modalities are more accessible in the setting of AMI than phase-contrast MR. We have shown that the key spatial features and numerical values of residence time are well represented in the long-axis three-chamber plane imaged by 2D echo-CDV [65]. Thus, we do not believe that the main conclusions of our study would change qualitatively when using 3D techniques. As stated above, we did not take into account local and systemic factors that may modulate the risk of LVT. Because a number of stasis metrics were tested, we cannot exclude a certain degree of overfitting in our results. Because we did not perform MR studies in all patients, the exact values of diagnostic performance of stasis metrics to predict LVT must be interpreted with caution.

3.4.4 Clinical Implications

Although we focused on the LV in patients with anterior AMI, other heart chambers and cardiac conditions can also be analyzed applying residence-time methods to flow measurements obtained either by phase-contrast MR [65] or computational fluid dynamic methods. Of particular interest is the field of atrial fibrillation, in which the established paradigm of mural thrombosis formation in the left atrial appendage has been questioned [11]. Also, a full understanding of the mechanisms involved in the thrombotic phenomena of LV assist devices is an unmet need of clinicians and engineers [84].

3.5 Conclusions

Stasis imaging is a useful technique to detect increased intraventricular blood retention in the heart. In anterior AMI, blood stasis is due not only to abnormal apical regional function but also to individual factors of inflow direction. Severe blood transport abnormalities and stasis are identified in patients who develop or are at risk for developing LVT after an anterior AMI. Thus, stasis mapping is a promising method to assess the risk of embolism in cardiac diseases.

3.6 Acknowledgements

Chapter 3, in part, has been published in the *Journal of American College of Cardiology: Cardiovascular Imaging*. Martinez-Legazpi, Pablo; Rossini, Lorenzo; del Villar, Candelas Pérez; Benito, Yolanda; Devesa-Cordero, Carolina; Yotti, Raquel; Delgado-Montero, Antonia; Gonzalez-Mansilla, Ana; Kahn, Andrew M; Fernández-Avilés Francisco; Bermejo, Javier; del Álamo, Juan C. 2017. The title of this paper is “Stasis Mapping Using Ultrasound: A Prospective Study in Acute Myocardial Infarction”. The dissertation author was the second author of this paper.

Chapter 4

Clinical assessment of intraventricular blood transport in patients undergoing cardiac resynchronization therapy

4.1 Introduction

Heart failure (HF) is an increasing global problem for healthcare systems. Responsible for high morbidity and mortality rates in developed countries, HF is the endpoint of a number of chronic cardiovascular diseases [32]. In more than half of patients with HF, the major hallmark of the disease is an impairment of systolic mechanics of the left ventricle (LV). The disease evolution entails a progression of myocardial damage which may also affect the conduction system of the heart. If the conduction in the left-bundle-branch is functionally disturbed, the physiological pathway of normal LV activation is lost. By delaying the onset of mechanical systole of the LV free-wall, left-bundle-branch block leads to a dyssynchronous contraction of the ventricular walls [21].

Dyssynchrony is associated with a higher risk of both worsened failure and sudden cardiac death [39]. In addition to intraventricular conduction abnormalities, patients with dyssynchrony also frequently have associated impaired conduction from the atria to the ventricles. Atrioventricular (AV) dyssynchrony further impairs the ability of the failing heart to pump blood, worsening the severity of HF [41, 47, 68, 85, 86].

Cardiac resynchronization therapy (CRT) is a well-established non-pharmacological treatment for congestive HF. CRT recovers the physiological activation pathways, improving cardiac function and clinical outcomes in patients who associate HF and dyssynchrony. When applied to adequately selected patient populations, CRT has a positive impact on symptoms, quality of life and mortality [12, 59]. This therapy is used to restore coordinated pumping of the ventricles by using a specialized cardiac pacemaker. Unfortunately, between 25% and 30% of patients receiving CRT do not show the expected benefits. It has been suggested that achieving a favorable CRT response may in part depend on proper device programming [31, 57, 72]. Therefore, optimization of the AV delay has been shown to improve cardiac output and may be necessary in up to 55% of CRT patients during follow-up [3, 77, 90]. However, the best method to optimize the AV delay is still controversial [40, 67].

Nature has optimized the coupling of molecular, electrical and mechanical processes of the heart, leading to flow patterns that minimize energy losses and facilitate the smooth redirection of incoming blood towards the outflow tract [10, 42, 63, 87]. The interaction between wall mechanics and intracavitary flow establishes fluid transport barriers, which separate the blood that transits from inflow directly to outflow each cardiac cycle from the blood that is retained inside the LV [10, 17–19, 23]. Lagrangian particle tracking using time-resolved 3D phase-contrast MRI velocity fields [83] and analysis of Lagrangian coherent structures (LCS) have been instrumental to quantify these transport barriers [10, 35]. However, these methods are based on expensive calculations of the trajectories of virtual fluid particles, and are difficult to automate for high-throughput analysis in the clinical setting.

Preliminary studies have shown that the main intraventricular flow pattern, a vortex ring that forms during diastole, is highly sensitive to the timing intervals of the cardiac cycle and to tachycardia [5]. Shortening the filling period by programing long electrical AV delays increases the circulation and kinetic energy of the vortex and results in the vortex staying closer to the mitral valve [35]. When compared to baseline conduction, biventricular stimulation seems to improve organization of intraventricular flow, suggesting that intraventricular flow analysis is a useful tool to understand the effects of resynchronization on heart mechanics [29]. Remarkably, changes in electrical activation have been shown to modify the net orientation of the forces acting on blood inside the LV, which has been associated with improved long-term outcome in patients undergoing CRT [61]. These findings suggest that flow imaging may be a suitable tool for optimizing this therapy. However, how CRT settings affect the specific time evolution of the different flow volumes and the LV filling waves is still poorly understood.

The present study was designed with the twofold purpose of

1. implementing a clinically feasible high-throughput method for measuring and mapping blood transport in the heart, and
2. testing its clinical potential to characterize changes in blood transport caused by CRT.

The general approach was to obtain individual quantitative metrics of flow transport from flow-velocity measurements in the LV.

4.2 Methods

4.2.1 Study Population

The present study is based on the analysis of 9 patients with HF and CRT under different AV delays and 3 healthy volunteers matched by age and gender to the patient group. Patients were consecutively enrolled from the pacemaker outpatient clinic. Controls were selected from a large database of healthy volunteers recruited at our institutions [6]. The study protocol was approved by the local institutional review committee, and all subjects provided written informed consent for this study. Clinical data are summarized in Table 4.1.

4.2.2 AV Delay Settings and Data acquisition

In the patient group, ultrasound sequences were acquired at 5 different programming settings to analyze the effect of pacing (CRT on vs CRT off), the AV delay

Table 4.1: Summary of study population data. Three normal subjects (VOL1-3) and nine patients undergoing CRT (CRT1-9) were considered. Patient CRT7 is used as example in Figures 4.1,4.2 and 4.4. Each patient is labeled with the symbol used to represent their data in Figures 4.3 and 4.5.

ID	Age	Gender	H.R. (bpm)	EF (%)	CRT OFF	AVOPT (ms)	AVMAX (ms)	AVMIN (ms)	100 bpm
VOL1	73	F	60	71	NORMAL	—	—	—	—
VOL2	55	F	70	56	NORMAL	—	—	—	—
VOL3	66	M	59	71	NORMAL	—	—	—	—
CRT1 (◯)	70	F	CRT dep.	52	YES	110	200	70	NO
CRT2 (□)	78	F	CRT dep.	38	YES	110	180	70	NO
CRT3 (⋄)	59	M	CRT dep.	39	YES	90	200	70	NO
CRT4 (▷)	62	M	CRT dep.	14	YES	90	150	70	NO
CRT5 (◁)	80	M	CRT dep.	51	YES	110	170	70	YES
CRT6 (▽)	62	F	CRT dep.	31	YES	110	210	70	NO
CRT7 (△)	57	F	CRT dep.	29	YES	110	170	70	YES
CRT8 ($\times$)	65	F	CRT dep.	30	YES	120	160	100	YES
CRT9 ($\star$)	59	M	CRT dep.	43	YES	80	180	70	NO

and the heart rate. Patients were studied in spontaneous sinus rhythm at 3 different AV delay settings: maximum AV (AVMAX), minimum AV (AVMIN), optimum AV (AVOPT). Then, maintaining the optimum AV, images were again acquired at 100 bpm induced by atrial pacing. Finally, patients were studied after turning off the cardiac pacing (CRTOFF). Maximum AV was obtained by increasing AV delay until capture was lost due to intrinsic conduction. Minimum AV was obtained by decreasing the AV delay down to 80 ms. The optimum AV delay was set using the iterative method, which uses the mitral valve pulsed wave Doppler to optimize the diastolic filling time (DFT). The iterative method attempts to obtain the longest DFT time that does not truncate A-wave, achieving maximal separation between the E- and the A-waves. Briefly, DFT was measured from the start of the E-wave until the end of the A-wave. A long AV delay was programmed and reduced in 20-ms steps until A-wave truncation. The interval was then increased in 10 ms increments, and the shortest AV delay without A-wave truncation was selected to maximize the DFT [72].

Comprehensive echocardiographic examinations were performed using a Vivid 7 ultrasound machine with 2-4 MHz transducers (GE Healthcare). For each particular CRT-device setting, we obtained 2D color-Doppler and B-mode (grayscale) sequences from the long-axis apical view. In addition, pulsed-wave Doppler recordings were obtained from the 5-chamber apical view, carefully located to obtain spectral recordings of opening and closing of the mitral and aortic valves. Event timings of the cardiac cycle were measured from these recordings, and then forwarded to the fluid-dynamic solver [6].

4.2.3 2D Image Analysis and Intraventricular Flow Processing

The LV myocardial wall was segmented using speckle-tracking software to delineate the endocardial boundary (EchoPac v.110.1.2, GE Healthcare). We reconstructed the time-dependent flow field inside the LV using 2D echo-CDV, as previously described and validated in vitro [24] and in vivo [6]. Conventional Doppler-echocardiographic data was measured following current recommendations [44].

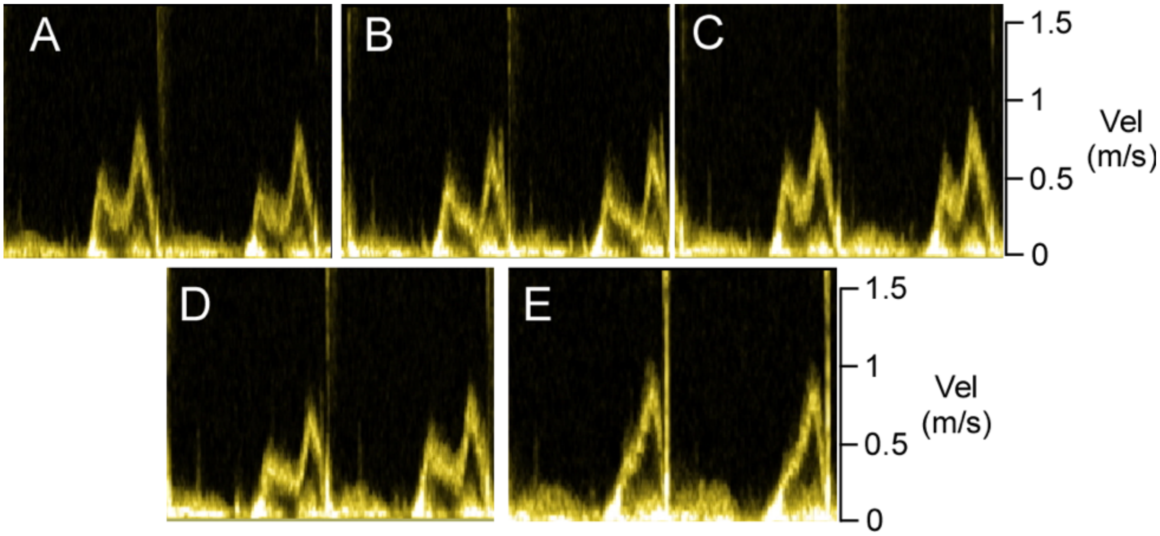

Figure 4.1: Pulse wave Doppler inflow velocity as a function of time in a patient without CRT (A), and undergoing CRT at AVOPT (B), AVMAX (C), AVMIN (D), and atrial pacing at 100 bpm(E). Notice the truncation of the A wave for AVMIN, affecting the timing of atrial driven filling, and the fusion of the E and A waves for tachycardia.

4.2.4 Blood Transport Assessment

Blood transport equation for Virtual MULTI-COLOR Angiography

Using the time-dependent 2D echo-CDV velocity field v(x,t) and the LV wall tracking data as input, we solved an advection equation for a passive scalar field ψ with uniform initial conditions and step-wise Dirichlet inflow boundary conditions,

$$\frac{\mathrm{D}\psi}{\mathrm{D}t} = \frac{\partial \psi}{\partial t} + \nabla \cdot (\vec{v}\psi) = 0, \tag{4.1}$$

$$\psi\left(\mathbf{x}, t=0\right) = \psi_0 = \text{const}, \tag{4.2}$$

$$\psi\left(\mathbf{x}_{inlet}, 0 < t < t_1\right) = \psi_0 = \text{const}, \tag{4.3}$$

$$\psi\left(\mathbf{x}_{inlet}, t_1 \leq t < t_2\right) = \psi_0 = \text{const}, \tag{4.4}$$

$$\text{etc.}$$

This continuous semi-Lagrangian approach tags different volumes of blood with different numerical values that are transported by the flow, thereby simulating the visualization of distinct virtual contrast media inside the LV. For instance, one can implement a two-step inlet boundary condition to track the evolution of the two fluid volumes that enter the ventricle during the E wave and the A wave. Blood is a complex multi-component suspension for which it is generally accepted that the mass diffusivity of different species is negligible compared to momentum diffusivity [7, 73]. Thus, we did not include a diffusive term in the transport equation. This approach is analogous to previous analyses of LV blood transport based on the deterministic integration of fluid particle trajectories [10, 17, 18, 23, 35]. Note that the absence of diffusive terms makes it possible to integrate equation 1 backward in time applying Dirichlet boundary conditions at the outlet of the domain. As shown below, combining the results from the forward and backward integrations allows for a straightforward categorization of blood transport templates inside the LV. Equation (4.1) was numerically integrated using previously described in-house software written in FORTRAN [65]. The equation was discretized on a Cartesian grid by a 2nd-order finite volume method, and a total variation diminishing flux limiting scheme [46] was used to avoid numerical oscillations at the sharp interfaces created between volumes of blood with different inflow tags.

Characterization of blood transport patterns

The time-evolving distribution of ψ was automatically thresholded to track the blood carried by the transport structures generated during the E-wave and A-wave, and to determine the size of these structures and their frontal position.

Equation (4.1) was integrated with uniform initial conditions and two different inlet boundary conditions for the E wave and A wave (e.g. $\psi(x, t = 0) = 0$, $\psi(x_{inlet}, t \in \mathrm{E-wave}) = 1$ and $\psi(x_{inlet}, t \in \mathrm{A-wave}) = 2$). The iso-contours $\psi = 0, 1, 2$ allowed us to track the time-evolving distribution of the blood that entered the LV during both filling waves, together with that of the residual volume of blood occupying the LV at the onset of diastole. E and A wave sizes, S_E and S_A, were calculated from the area they occupied in the imaging plane, and normalized by the total end-diastolic LV area in the same plane. To systematically analyze the effect of AV delay on LV filling transport, we determined the fraction of LV size occupied by the E and A waves, S_E/S_{LV} and S_A/S_{LV}, as well as the normalized apical position of each wave's front X_E/L and X_A/L, where L is the long axis length of the LV (i.e.

$X/L = 0$ is the LV base and $X/L = 1$ is the LV apex).

In addition to tracking the filling transport patterns, we analyzed the spatiotemporal evolution of the blood that is ejected each cardiac cycle by integrating equation (4.1) backwards in time with uniform initial conditions, and Dirichlet boundary conditions at the aortic valve annulus. Combining the results from the backward and forward integrations allowed us to automatically identify the following transport structures: direct flow (DF, blood that enters and exits the LV in the same cardiac cycle), retained inflow (RI, incoming blood that is not ejected during the same cycle), delayed ejection (DE, ejected blood that entered the LV in a previous cardiac cycle) and residual flow (RF, blood that entered the LV in a previous cycle and is not ejected in the current cycle, therefore residing in the LV for at least two cardiac cycles) [10]. For the purpose of this 2D study we used the respective planar-volumes (areas) to account for each of these fractions.

To assess the kinematic efficiency of flow redirection inside the LV under CRT, we determined the size, kinetic energy density and acceleration of each transport region at the onset of systole. Kinetic energy density was calculated from 2D echo-CDV data as $K(\mathbf{x},t) = |\mathbf{v}|^2/2$. Fluid acceleration was calculated as $\mathbf{m}(x,t_0) = \left(\dfrac{\partial \mathbf{v}}{\partial t} + \mathbf{v}\cdot\nabla\mathbf{v}\right)$. These variables were spatially integrated over the surface occupied by each transport region to obtain their overall values inside the region (e.g. $M_{DF} = \int_{S_{DF}} \mathbf{m}(\mathbf{x})\mathrm{d}\mathbf{x}$). It is important to note that $\mathbf{M}$ is a vector that not only indicates the magnitude of the acceleration of each fluid volume, but also its direction. The orientation of the whole ventricle's $\mathbf{M}$ with respect with the ventricular long axis has been recently shown to correlate with long-term outcome in patients undergoing CRT [61]. We calculated the ratio $\eta_K = K_{DF}/K_{LV}$ at aortic valve opening in all the patients to determine if CRT changes contributed to efficiently focusing the inflow kinetic energy into the volume of fluid that was ejected during systole. The ratio of direct flow area to total LV area in the imaging plane, $\eta_{DF} = S_{DF}/S_{LV}$, was also computed to quantify the efficiency of volumetric blood transport within one cardiac cycle.

In addition to focusing kinetic energy towards into the direct flow volume, efficient LV blood transit from the inflow to the outflow tract requires a marked change in the direction of fluid motion. A measure of the efficiency of this process

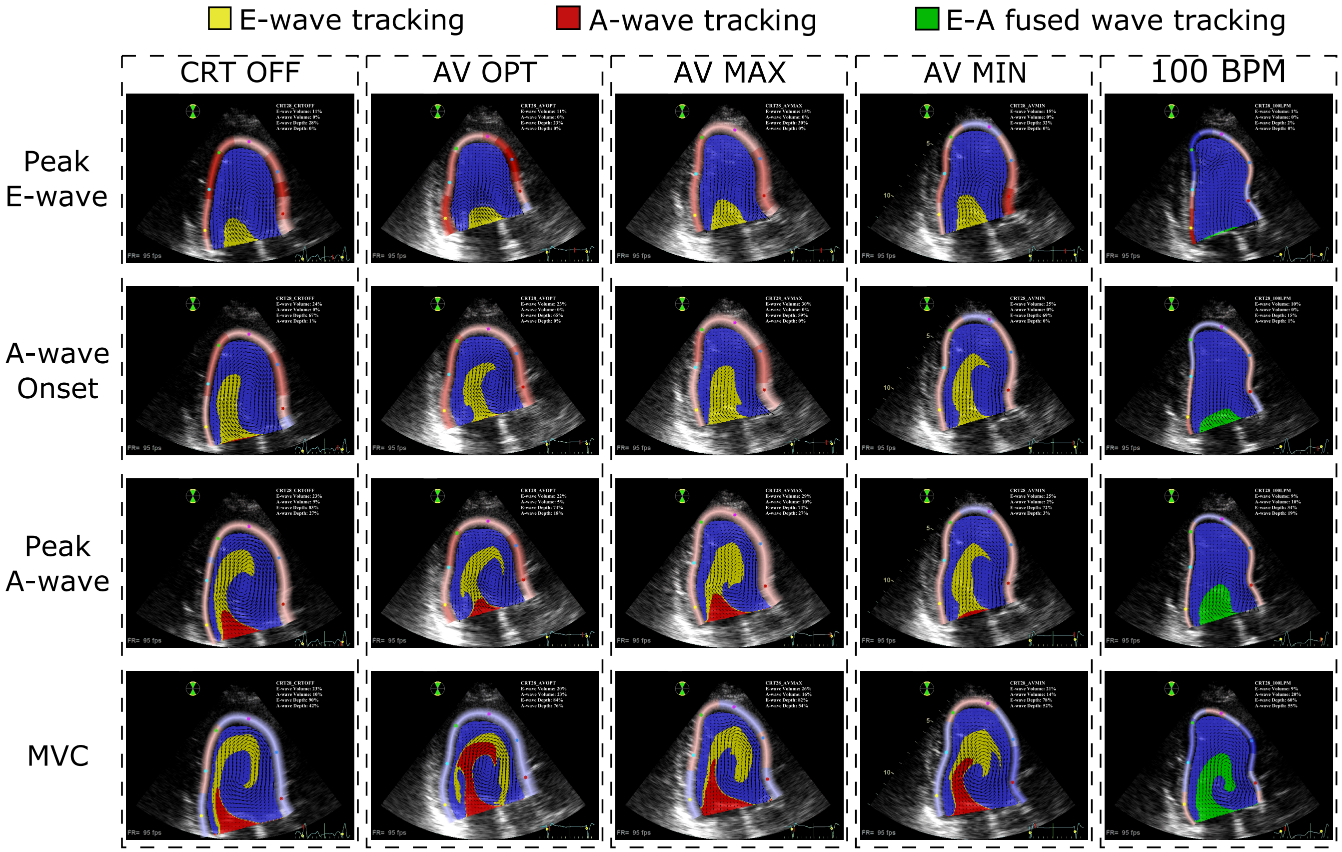

Figure 4.2: Evolution of filling transport regions in the LV of the same patient shown in Figure 4.1. Each column represents a different CRT setting: A) CRT-OFF, B) AVOPT, C) AVMAX, D) AVMIN and E) Tachycardia (100 bpm). Each row represents a different instant during diastole: the 1st , 2nd, 3rd and 4th rows correspond respectively to peak E wave, A-wave onset, peak A wave and MVC. In each panel, the yellow and red regions track respectively the fluid that enters the LV during the E wave and the A wave, whereas the blue background tracks the residual volume of blood that occupies the LV at the onset of diastole. Instantaneous velocity vectors are shown in black. In the Tachycardia setting the E/A-waves fusion is depicted in green.

Table 4.2: Intraclass correlation coefficient (R_{ic}) of the reproducibility study. S_{DF}: Direct flow, S_{RI}: Retained inflow, S_{DE}: Delayed ejection, S_{RF} : Residual flow and, S_{LV}: Whole LV planar volumes. $S_E/_{LV}$ and S_A/S_{LV}, fraction of LV size occupied by the E and A waves.

Parameter	Intraobserver	Interobserver
S_{DF}/S_{LV} (η_{DF})	0.75	0.85
S_{RI}/S_{LV}	0.46	0.51
S_{DE}/S_{LV}	0.70	0.69
S_{RF}/S_{LV} (λ_{RF})	0.68	0.84
S_E/S_{LV}	0.73	0.77
S_A/S_{LV}	0.53	0.53

is the net acceleration transferred to the direct flow region in the direction of the LV outflow tract normalized with the total magnitude of this acceleration, $\eta_{\mathbf{M}} = \mathbf{M}_{DF} \cdot \mathbf{e}_{LVOT}/|\mathbf{M}_{DF}|$, where $\mathbf{e}_{LVOT}$ is the unitary vector parallel to the direction of the LV outflow tract, pointing outwards the LV. The calculation of the 2D+t velocity field, the integration of equation (4.1) and the post processing work were programmed to be automatic and no-operator dependent. Best and worst full time for the entire post-processing from RAW echo images were 10 and 20 minutes (13±3 min).

Reproducibility (fully blinded echocardiographic image acquisition and re-acquisition, calculation of 2D flow velocity fields, event-time identification, and final index computation by two independent observers; n= 7 normal subjects) was relatively good for most calculated indices (Table 4.2).

4.2.5 Statistical Analysis

Individual scatterplots and boxplots showing the median and interquartile range are shown for each parameter. Differences among phases are compared using linear mixed effects accounting for repeated measured within each subject (random effect). Reproducibility of quantitative indices was analyzed using the intraclass correlation coefficient (R_{ic}). All analyses were performed in R (v. 3.2) and p values $<$ 0.05 were considered significant.

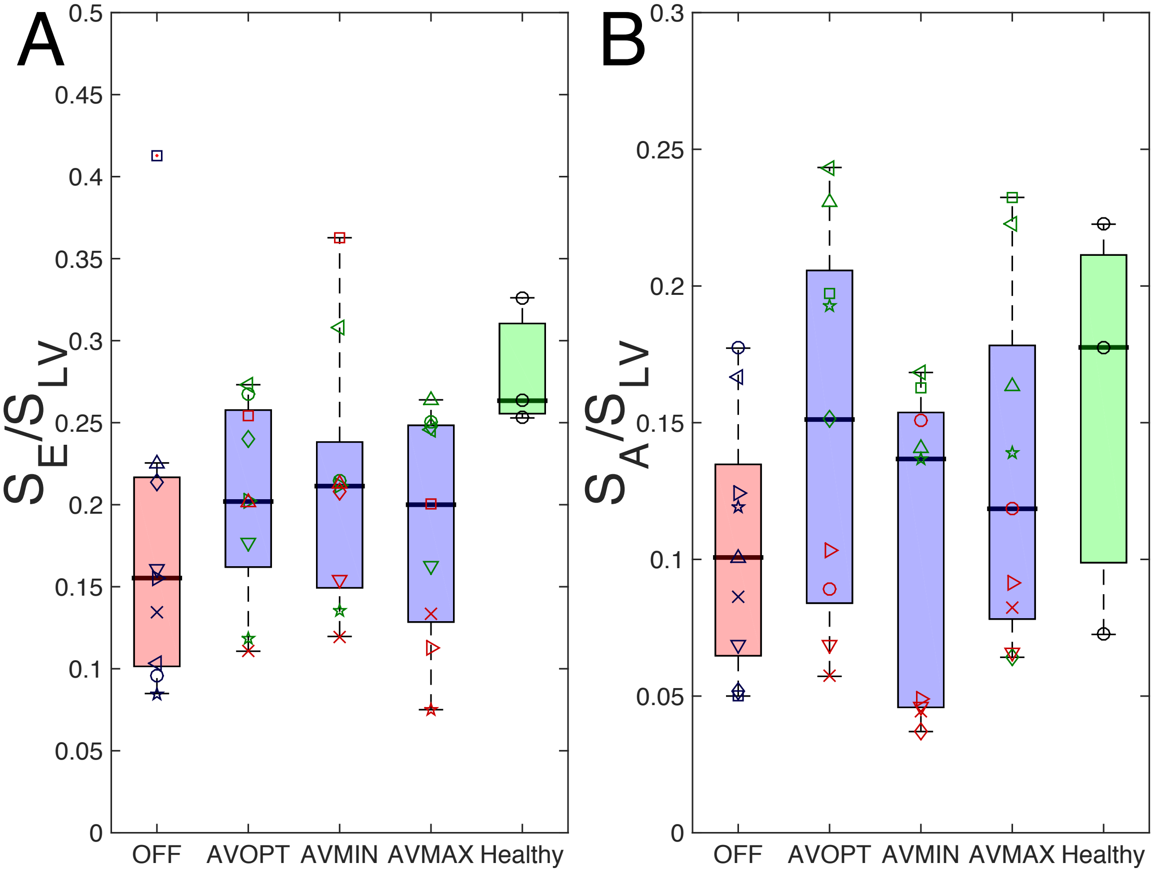

Figure 4.3: Percentage LV volume occupied by E-wave (panel A) and A-wave (panel B) filling transport at mitral valve closing in patients (N=9) undergoing CRT with different AV delay settings, compared with healthy volunteers (N=3). The data in each column are plotted as univariate scatter plots and summarized in the form of boxplots. In the patients, red and blue boxplots refer respectively CRTOFF and different AV delay cases. Each symbol type refers to a different patient, and is colored in green (red) if CRT makes the corresponding variable more (less) similar to the healthy subjects. The latter are represented by a green boxplot.

Table 4.3: Results of E and A wave tracking at mitral valve closing (average ± standard deviation). $X_E/$ and X_A/L : normalized apical position of each E and A waves. $S_E/_{LV}$ and S_A/S_{LV}, fraction of LV size occupied by the E and A waves.

	OFF	AVOPT	AVMIN	AVMAX	100BPM	NORMALS
X_E/L	0.81±0.14	0.82±0.12	0.83±0.14	0.87±0.11	0.51±0.16	0.75±0.08
X_A/L	0.45±0.16	0.45±0.23	0.30±0.20	0.51±0.22		0.47±0.12
S_E/S_{LV}	0.18±0.1	0.20±0.06	0.21±0.08	0.18±0.07	0.15±0.10	0.28±0.04
S_A/S_{LV}	0.10±0.05	0.15±0.07	0.10±0.06	0.13±0.06		0.16±0.08

4.3 Results

4.3.1 Intraventricular Inflow and Blood Transport Under Cardiac Resynchronization Therapy

CRT and AV delay optimization modify the inflow velocity profile in patients implanted with bi-ventricular pacemakers. This is illustrated in Figure 4.1, which displays pulsed wave Doppler (PW) measurements from a representative patient (CRT7, see Table 4.1) for each one of the 5 different pacing settings. The PW profiles exhibit the two flow velocity envelopes that define left-ventricular filling flow: the E-wave representing the early, passive filling phase of the LV, and the A-wave representing the late active filling phase driven by the atrial contraction. Varying the AV delay displaces the start and end of these waves in time, and modulates the magnitude and timing of the inflow velocity, leading therefore to different intraventricular flow fields.

4.3.2 Atrioventricular Delay and Blood Transport During Early and Late Filling

The AV delay has a number of effects not only on global chamber mechanics but also on myocardial fiber pre-stretching and contraction [91]. Consequently, as said above, changes in AV delay modify the dynamics of the filling flow driven by the E and A waves. Figure 4.2 illustrates these differences for the same patient shown in Figure 4.1. The total amount of blood entering the LV varied between 26% and

42% of the LV area in the imaged plane for the pacing settings considered, in fair agreement with the patient's measured ejection fraction of 29% measured at AVOPT. More importantly, both the size (i.e. area) and shape of the regions defined by E-wave and A-wave filling were sensitive to the presence of pacing (CRTON vs CRTOFF), the AV delay, and the heart rate (Table 4.3). In the patient group, CRT increased the fraction of LV volume occupied by the E wave at the end of diastole, bringing this variable closer to the healthy range (Figure 4.3A). The observed increase in the early LV filling volume was particularly noticeable for AVOPT, where 6 out of the 9 patients experienced an increase in S_E/S_{LV}. We found a similar trend for CRT to increase the apical position of the E-wave front (Table 4.3). Moreover, CRT caused moderate rising in the late filling volume fraction S_A/S_{LV} (Figure 4.3B).

4.3.3 Time-Evolution of Intraventricular Transport Regions

Figure 4.4 displays the end-diastolic distribution of the direct flow, retained inflow, delayed ejection and residual flow regions in the LV of the representative patient shown in figures 4.1 and 4.2. In the absence of pacing, the overall transit of LV blood transport followed a wide arch, so that a large fraction of LV volume in the center of the chamber remained as residual flow. CRT altered this effect increasing direct flow, particularly for AVOPT. With tachycardia, the filling and ejection phases were shortened and defined small transport regions that did not intersect significantly, consequently creating a small amount of direct flow. Figure 4.5A and Table 4.4 summarize the statistics of η_{DF} as a function of AV delay in the patient population, including reference data from healthy subjects and previous studies. Consistent with Figure 4.4, AVOPT shows a significant increment in the direct flow region with respect to the CRTOFF condition in the whole population; η_{DF} increased in 7 of the 9 patients, and the median η_{DF} increased by a factor of ~ 3. The variation of η_{DF} was less pronounced for the two other AV delay settings, though η_{DF} increased in 7 out of 9 patients for both AVMIN and AVMAX . In addition to increasing direct flow, CRT enhanced the efficiency of LV blood transit by decreasing the portion of the chamber occupied by residual volume, defined as $\lambda_{RF} = S_{RF}/S_{LV}$ (Figure 4.5B). Eight out 9 patients reduced their residual volumes at AVOPT. Nevertheless, AVMAX also

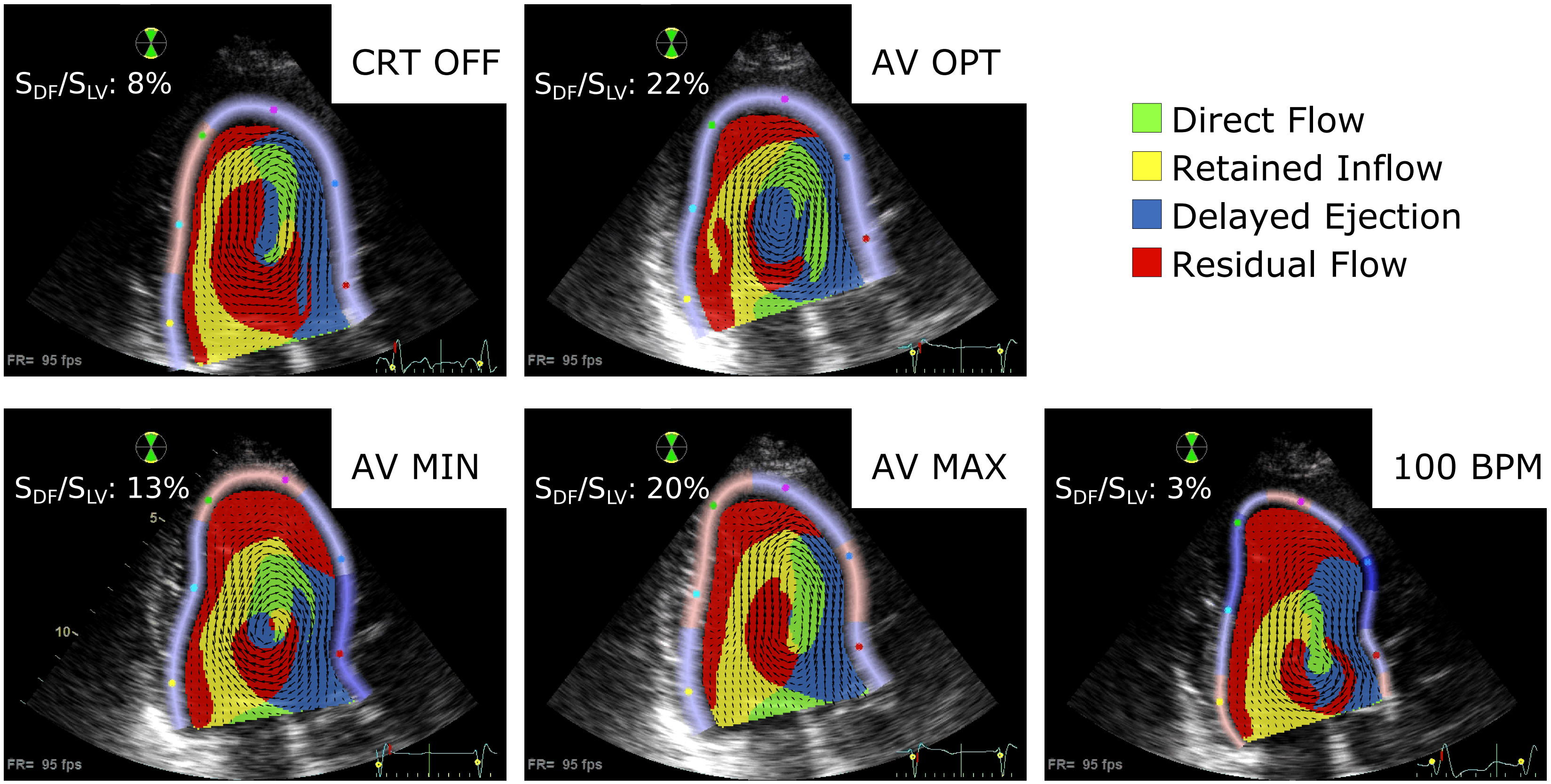

Figure 4.4: End-diastolic distribution of different transport regions in the LV of the same patient shown in Figures 4.2 and 4.4, plotted for different CRT settings (CRTOFF, AVOPT, AVMIN, AVMAX and Tachycardia). The different regions represented are direct flow (green), retained inflow (yellow), delayed ejection (blue) and residual flow (red)

Table 4.4: Average ± standard deviation of relative end-diastolic flow fractions of the LV for the different CRT settings compared with the values obtained by Eriksson et al, Fredriksson et al. and Bolger et al [25,23,22]. S_{DF}: Direct flow, S_{RI}: Retained inflow, S_{DE}: Delayed ejection, S_{RF}: Residual flow and, S_{LV}: Whole LV planar volumes. * in the results by Eriksson et al, Fredriksson et al. and Bolger et al account for a patient with dilated cardiomyopathy.

	OFF	AV opt	AV min	AV max	100 bpm	Healthy	Eriksson et al. (2010)	Eriksson et al. (2010)	Fredriksson et al. (2011)	Bolger et al. (2007)	Bolger et al. (2007)
N	9	9	9	9	9	3	13	1*	10	17	1*
S_{DF}/ S_{LV} (η_{DF})	0.06 ± 0.04	0.14 ± 0.09	0.12 ± 0.07	0.10 ± 0.06	0.06 ± 0.05	0.24 ± 0.08	0.37 ± 0.05	0.08	0.44 ± 0.06	0.21 ± 0.06	0.04
S_{RI}/ S_{LV}	0.23 ± 0.07	0.24 ± 0.07	0.23 ± 0.10	0.26 ± 0.09	0.16 ± 0.11	0.20 ± 0.04	0.17 ± 0.04	0.25	0.17 ± 0.03	0.27 ± 0.08	0.31
S_{DE}/ S_{LV}	0.17 ± 0.04	0.17 ± 0.08	0.17 ± 0.06	0.17 ± 0.06	0.13 ± 0.08	0.21 ± 0.02	0.16 ± 0.03	0.28	0.15 ± 0.03	0.27 ± 0.06	0.26
S_{RF}/ S_{LV} (λ_{RF})	0.54 ± 0.09	0.45 ± 0.14	0.48 ± 0.15	0.46 ± 0.15	0.66 ± 0.17	0.35 ± 0.06	0.30 ± 0.05	0.37	0.23 ± 0.06	0.24 ± 0.12	0.39

Table 4.5: Flow kinematic efficiency parameters obtained at aortic valve opening (average ± standard deviation). η_K: ratio of total kinetic energy in the volume of fluid that is focused into the direct flow region; λ_K: ratio of total kinetic energy in the volume of fluid that is focused into the residual flow region; η_M: net acceleration transferred to the direct flow region in the direction of the LV outflow tract normalized with the total magnitude of this acceleration.

	OFF	AVopt	AVmin	AVmax	100bpm	NORMALS
η_K	0.09±0.07	0.25±0.18	0.22±0.13	0.18±0.15	0.07±0.09	0.25±0.08
λ_K	0.36±0.10	0.26±0.21	0.25±0.14	0.29±0.20	0.49±0.30	0.16±0.05
η_M	0.37±0.61	0.70±0.43	0.60±0.57	0.62±0.61	0.76±0.27	0.68±0.20

provided a significant effect (λ_{RF} decreased in 7/9 patients).

We found η_K to be higher in the healthy subjects than in the patients with CRTOFF. Furthermore, there was a clear trend of increase in η_K with CRT that was relatively insensitive to the AV delay. Additionally, CRT decreased the amount of inflow kinetic energy that remains in the residual volume at the end of diastole, $\lambda_K = K_{RF}/K_{LV}$. The observed decrease in wasted kinetic energy was most significant for AVOPT and AVMIN, with λ_K showing variations in 8 and 9 (out of 9) patients respectively (Figure 4.5D, Table 4.5). Figure 4.5E and Table 4.5 summarize the statistics of η_M at the onset of systole. Similar to η_{DF} and η_K, this directional parameter became higher with CRT regardless of the AV delay, showing an increase in 6 out of 9 patients for AVMIN, AVMAX and AVOPT.

4.4 Discussion

In the present study we implement a high-throughput method, suitable for visualizing and measuring flow transport in the LV using ultrasound in the clinical setting. This method is based on a continuous semi-Lagrangian formulation that allowed us to track and to determine quantitative metrics of LV volume fractions from flow velocity measurements with no user interaction. As a result, this method provides accurate maps of blood transport without the need to integrate the trajectories of a large number of virtual blood particles and to perform semi-manual segmentation of the delineated fluid structures, as previously done using either phase-contrast MR

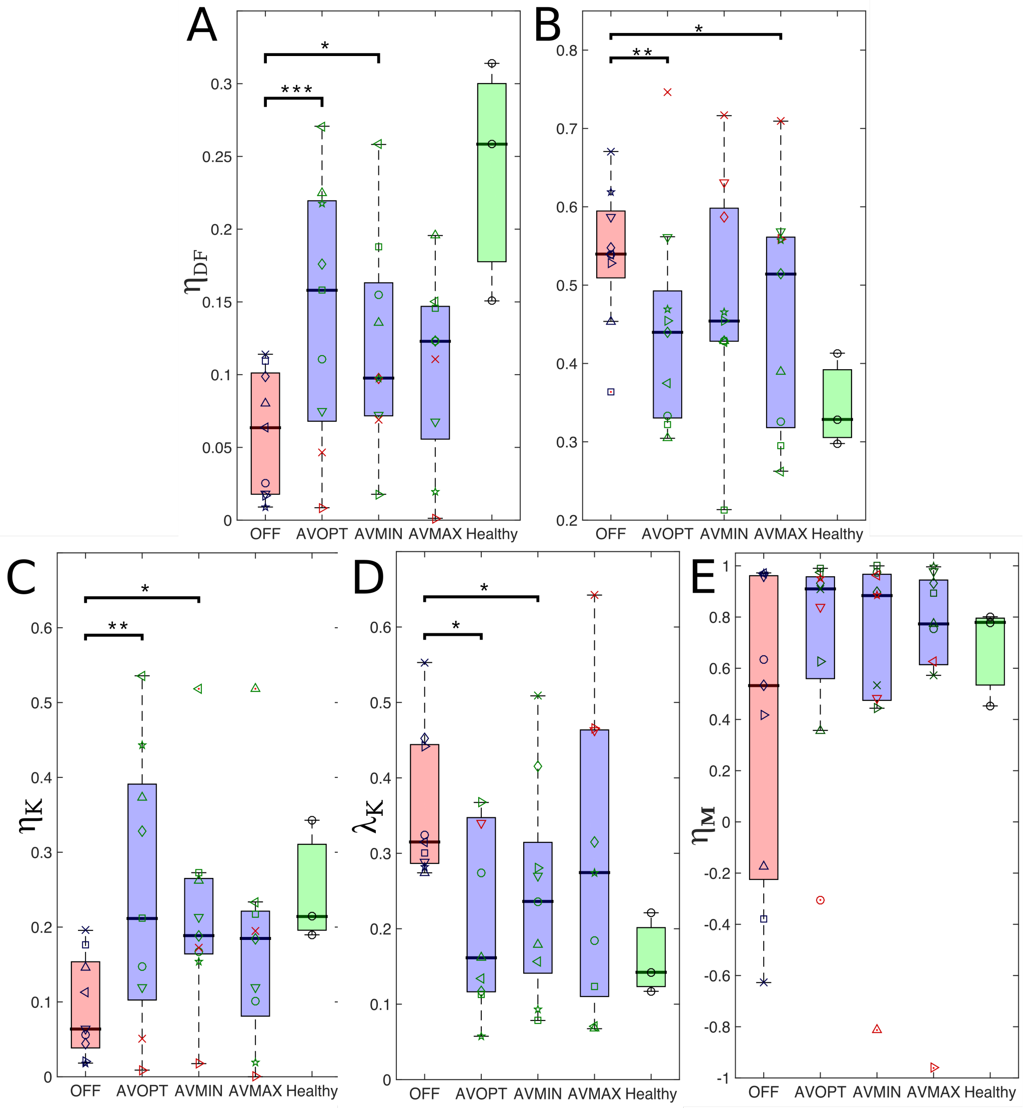

Figure 4.5: Statistics of intraventricular blood redirection efficiency at aortic valve opening in patients (N=9) undergoing CRT with different AV delay settings, compared with healthy volunteers (N=3). A) Fraction of LV volume that undergoes direct flow in the imaged plane, $\eta_{DF} = S_{DF}/S_{LV}$. B) Fraction of LV occupied by residual volume in the imaged plane, $\lambda_{RF} = S_{RF}/S_{LV}$. C) Fraction of total kinetic energy in the LV contained in the direct flow region, $\lambda = K_{RF}/K_{LV}$. D) Fraction of total kinetic energy in the LV contained in the residual volume, $\eta_K = K_{DF}/K_{LV}$. E) Net acceleration communicated to the direct flow region in the direction of the outflow tract, normalized by the total acceleration magnitude, $\eta_{\mathbf{M}} = \mathbf{M}_{DF} \cdot \mathbf{e}_{LVOT}/|\mathbf{M}_{DF}|$). The data in each column are plotted as univariate scatter plots and summarized in the form of boxplots. In the patients, red and blue boxplots refer respectively CRTOFF and different AV delay cases. Each symbol type refers to a different patient, and is colored in green (red) if CRT makes the corresponding variable more (less) similar to the healthy subjects. The latter are represented by a green boxplot.

[10] or Doppler-echocardiography [35]. Our data compare well with previous studies using phase-contrast MR in healthy and diseased hearts, as shown in Table 4.4.

We used manual modification of CRT pacemaker parameters to illustrate the clinical potential of this novel tool, and demonstrated acute changes in blood transport patterns inside the LV with different AV delays. As shown, flow organization inside the LV is highly dynamic and sensitive to the timing of cardiac events. Even a moderate increase in heart rate induced important changes in the manner LV flow affects the transit of blood from the mitral valve to the aorta.

However, the functional consequences of intraventricular flow organization remain mostly unknown. It has been shown that diastolic vortex structures are useful to efficiently transport flow from the LA towards the apex, both during the early and late filling phases [28, 50]. As described above, direct flow allows a significant amount of the inflow's kinetic energy to be transferred to the ejection volume. To what extent preserving energy throughout the cardiac cycle provides a functional benefit in the normal heart is a matter of debate [42, 59, 70, 78]. However, any mechanism of increased performance may be relevant in the failing ventricle which has almost exhausted its contractile reserve.

Overall, the presented data imply that the spatio-temporal evolution of the intraventricular blood flow in a patients undergoing CRT can be highly sensitive to heart rate and AV delay. The blood flow in the CRTOFF condition is driven by a persistent clockwise swirling pattern that is typically found in patients with dilated cardiomyopathy [6, 35], forcing the blood entering the LV to follow an arched path along the inferolateral and anteroseptal LV walls. Turning CRT on modified this transport pattern, particularly for AVOPT. For the latter CRT setting, the incoming blood was distributed forming a pattern consistent with a more symmetric starting jet - vortex ring structure.

In addition to having an effect on LV filling, CRT may potentially improve the efficient redirection of left ventricular blood inflow towards the outflow tract by: 1) modifying the transport patterns to increase the amount of blood coming into the LV each cardiac cycle that is ejected in the same cardiac cycle (i.e. direct flow), 2) increasing the amount of kinetic energy that is transferred from incoming blood to ejected blood, and 3) aligning the motion of the ejected blood with the left ventricular outflow tract. Furthermore, our results and the emerging literature imply that CRT favors the generation of coherent intraventricular pressure gradients that accelerate blood in the direction of the LV outflow tract [61]. Finally, the impact of different transport patterns on intraventricular flow mixing and prevention of blood stasis needs to be addressed [65].

Flow transport visualization methods such as the one presented in this study are readily applicable to large patient populations and are therefore particularly well suited to clarify issues such as the effect of CRT on LV blood transport. This is supported by the relatively good agreement between the presented data and previous studies using PC-MR, especially in the diseased heart (see Table 4.4). From a clinical perspective, this method opens the possibility of using flow imaging techniques to optimize CRT. However, large-scale trials will be necessary to clarify the future role of intracardiac fluid dynamics in medical diagnosis, clinical decision-making, and physiologic programming of cardiac devices. In addition, these emerging methods will likely provide new fundamental insight on cardiac biomechanics. Flow transport visualization methods not only will help investigators to understand the physiological basis of heart failure but also to optimize pharmacological and non-pharmacological therapies to improve the outcomes associated with one of the most prevalent diseases in the world.

4.5 Limitations

We used a 2D flow imaging method even though intraventricular blood transport is a 3D process. This planar flow simplification may lead to some degree of inaccuracy in the estimation of transport. However, our echocardiographic 2D approach has important practical advantages, as it provides high temporal and spatial resolutions, is fast, clinically feasible, and does not require infusion of contrast agents. Moreover, the proposed transport analysis methodology relies on clinical access to time-resolved LV velocity fields, but it is independent of the particular imaging modality employed to measure intraventricular velocity. Applying a similar analysis to flow velocity maps from time-resolved 3D phase-contrast MR has shown that the key features of intraventricular blood transport and mixing are well represented in the long-axis three-chamber plane imaged by 2D echo-CDV [74]. Thus, although the exact transport numerical values may vary when they are calculated in 3D, we are confident that our 2D analysis was able to accurately capture relative changes induced by CRT on intraventricular flow transport. Larger clinical studies shall establish the final clinical of this novel methodology technique in the modern armamentarium of cardiovascular imaging.

4.6 Conclusions

Blood transport patterns in the LV can be readily derived from flow-velocity fields by solving a passive-scalar advection partial differential equation. This continuous semi-Lagrangian method is suitable for high-throughput processing without the need of discrete particle tracking or user interaction. Combining this tool with color-Doppler ultrasound, we were able to demonstrate important effects of cardiac resynchronization therapy and atrioventricular delay optimization on intraventricular blood transport.

4.7 Acknowledgements

Chapter 4, in part, has been published in *Meccanica.* Rossini, Lorenzo; Martinez-Legazpi, Pablo; Benito, Yolanda; del Villar, Candelas Pérez; Gonzalez-Mansilla, Ana; Barrio, Alicia; Borja, María-Guadalupe; Yotti, Raquel; Kahn, Andrew M; Shadden, Shawn C; Fernández-Avilés Francisco; Bermejo, Javier; del Álamo, Juan C. 2017. The title of this paper is "Clinical assessment of intraventricular blood transport in patients undergoing cardiac resynchronization therapy". The dissertation author was the primary author of this paper.

Chapter 5

Conclusions and future direction

5.1 Summary of the dissertation

In this dissertation we have presented a new method to quantify and assess blood stagnation in the left ventricle. The method is based on intraventricular velocity flow maps which can be obtained completely non-invasively using standard ultrasound acquisition or 4D Flow cardiac magnetic resonance imaging. The focus of this research has been on the ultrasound modality because of how easily such images can be obtained and because it best fits within the current cardiology clinical work flow.

From a clinical perspective, this work introduces the new paradigm that a quantitative flow dynamics analysis can provide the basis to obtain sub-clinical markers of intraventricular thrombosis risk. In summary, the main idea is to measure the blood stasis through residence time inside a patient's left ventricle to predict an increased intraventricular thrombosis risk.

The residence time (T_R) spent by blood particles inside the LV since entering the chamber is obtained by solving the advection equation with unit forcing for a passive scalar from time-resolved blood velocity fields. Such equation can be obtained both from a Lagrangian view for each blood particle or more rigorously from statistical mechanics as shown in Chapter 2. A residence time threshold can be used to automatically segment and label residual blood volumes that do not mix with the fresh blood entering the LV each cardiac cycle, and which are potentially stagnant.

When compared to Lagrangian particle tracking, this approach has the advantage to be fully automatic, operator independent and very efficient computationally.

We initially tested the new method in normal hearts, dilated cardiomyopathy and a patient before and after the implantation of a left ventricular assist device (LVAD) to show feasibility of the idea. We were able to also test the method using 3D PC-MRI and the results suggested that the 2D long axis view is able to capture the main features of LV blood transport. We also developed original metrics to combine complex flow properties such as blood kinetic energy and shear stress into simple scalars suitable for a robust and personalized assessment of the risk of thrombosis.

To test the validity of the method and the hypotheses in a relevant clinical scenario we chose patients with acute myocardial infarction (AMI). In this patient population (after an anterior-AMI) the incidence of LV thrombosis can be as high as 15-20% and the risk of cardiac embolism clearly exceeds that of the general population. The sequential study of LV blood stasis after AMI allowed for addressing the time-evolving interactions among regional myocardial function, intraventricular stasis and mural thrombosis. Assessing the risk of LV thrombosis is of particular value in patients with an anterior-AMI because prophylactic anti-coagulation has to be balanced against the bleeding risk of triple antithrombotic regimens.

Using our residence time approach, we characterized the blood stasis abnormalities induced by AMI: our data shows that larger and more persistent regions of stagnant blood, particularly those with a large endocardial contact perimeters, are associated with mural thrombosis. Upon the recovery of myocardial function, changes in intraventricular flow and stasis appear and the results of our determinant analyses emphasize the complexity of the flow features that govern thrombosis. This complex interaction between myocardial function, blood stasis and mural thrombosis may explain why conventional echocardiographic indices of LV function are limited to guide preventive anticoagulation.

Finally in Chapter 4, we modified our residence time method to compute the different blood transport regions. This compartmentalization of blood volumes (or surfaces in 2D) is relatively common in the literature and allowed us to show how cardiac resynchronization therapy has direct influence in the LV blood transport phenomenon.

In this case, patients who are considered non responders to CRT might benefit from a blood transport analysis as we have showed that the spatio-temporal evolution of the intraventricular blood flow in CRT patients can be highly sensitive to the device programming (heart rate and AV delay). For the optimal AV-delay, the incoming blood was distributed forming a pattern consistent with a more symmetric starting jet - vortex ring structure. CRT also improved the efficient redirection of left ventricular blood inflow towards the outflow tract by increasing the amount of direct flow, its kinetic energy and aligning the motion of the ejected blood with the left ventricular outflow tract.

5.2 Recommendations for future work

The idea of blood stasis derived from blood residence time can be applied to different population of patients, with different imaging modalities and also to different heart chambers.

5.2.1 Left Ventricular Assist Device

One of the most straightforward application is in patients implanted with left ventricular assist device (LVAD). LVAD is a life-saving therapy for patients with advanced heart failure (HF). In the last decade the use of LVADs has increased significantly and the treatment is now widely used both as a bridge to heart transplantation or as a destination therapy. Despite a greatly improved survival the largest obstacle to the use of LVADs are the complications, particularly the ones related to thrombosis and bleeding.

As shown in Chapter 2, LVAD implantation drastically disrupts the normal physiological blood flow patterns in the heart. However, assessment of intraventricular flow patterns during LVAD treatment has been limited. A residence time based analysis would be useful to systematically describe qualitatively and quantitatively the modified intraventricular flow patterns. It would be of particular interest to study blood transport and stasis as a function of different device speeds during a ramp test, so that an optimal pump speed can be chosen for each patient.

5.2.2 Residence Time in the Left Atrium

Blood stasis is believed to be one of the main risk factors for intracardiac thrombosis not only in the left ventricle but also in the other heart chamber suche as the left atrium (LA). Atrial fibrillation (AF) is the most common form of arrhythmia that affects approximately 35 million people worldwide and is particularly common in elderly patients. Compared to the general population, patients with AF have five times the risk of stroke, which can cause major morbidity and death.

Anticoagulants may be administered to selected patients but this treatment carries major associated risks such as internal hemorrhaging. Currently, the decision whether to anti-coagulate patients with AF is based on general population factors (age, sex, blood pressure, etc.), which have moderate accuracy and modest predictive power.

Thromboembolic events have been tightly linked to blood stasis (especially in the left-atrial appendage), which could be identified by regions of high blood residence time. This premise is supported by recent literature [8, 16] showing that both the sphericity of the left atrial (LA) chamber and the shape of the left atrial appendage (LAA) correlate with stroke risk, which implies that flow features dictated by LA anatomy are an important factor contributing to left atrial thrombogenesis.

A patient-specific thrombosis risk scores derived from the analysis of blood flow and transport in the left atrium of individual patients could be an ideal metric to improve patient selection for anticoagulation treatments. Blood flow in the left atrium is more three dimensional than in the left ventricle and each patient's anatomy could be obtained from medical imaging to calculate the residence time of blood in the left atrium via computational fluid dynamics (CFD) direct numerical simulations (DNS).

A high-fidelity database resulting from DNS performed on several 3D patient-specific anatomies could be then used to develop and validate surrogate atrial thrombosis risk indices like geometric parameters of left atrial shape, their temporal changes along the cardiac cycle, or simplified indices of blood stasis inside the left atrial appendage based on Doppler echocardiography.

In contrast to computationally intensive CFD simulations, these surrogate indices of the left atrial blood stasis are computationally uninvolved and could be evaluated in real time in the clinical setting.

Bibliography

[1] P. C. Adams, M. Cohen, J. H. Chesebro, and V. Fuster. Thrombosis and embolism from cardiac chambers and infected valves. *J Am Coll Cardiol*, 8(6 Suppl B):76B–87B, 1986.

[2] A. Arboix and J. Alio. Cardioembolic stroke: clinical features, specific cardiac disorders and prognosis. *Curr Cardiol Rev*, 6(3):150–161, 2010.

[3] A. Auricchio, C. Stellbrink, S. Sack, M. Block, J. Vogt, P. Bakker, C. Huth, F. Schondube, U. Wolfhard, D. Bocker, O. Krahnefeld, H. Kirkels, and H. Pacing Therapies in Congestive. Long-term clinical effect of hemodynamically optimized cardiac resynchronization therapy in patients with heart failure and ventricular conduction delay. *J Am Coll Cardiol*, 39(12):2026–2033, 2002.

[4] A. Bakalli, L. Georgievska-Ismail, D. Kocinaj, N. Musliu, A. Krasniqi, and E. Pllana. Prevalence of left chamber cardiac thrombi in patients with dilated left ventricle at sinus rhythm: the role of transesophageal echocardiography. *J Clin Ultrasound*, 41(1):38–45, 2013.

[5] Y. Benito, J. Bermejo, M. Alhama, R. Yotti, C. Pérez del Villar, P. Martínez-Legazpi, A. González-Mansilla, A. Barrio, F. Fernández-Avilés, and J. C. del Álamo. Heart rate and AV delay modify left ventricular filling vortex properties. *Circulation*, 126:A18099, 2012.

[6] J. Bermejo, Y. Benito, M. Alhama, R. Yotti, P. Martinez-Legazpi, C. Pérez del Villar, E. Pérez-David, A. González-Mansilla, C. Santa-Marta, A. Barrio, F. Fernandez-Aviles, and J. C. del Alamo. Intraventricular vortex properties in non-ischemic dilated cardiomyopathy. *Am J Physiol Heart Circ Physiol*, 306(5):H718–29, 2014.

[7] J. Bermejo, P. Martinez-Legazpi, and J. C. del Alamo. The Clinical Assessment of Intracardiac Flows. *Ann Rev Fluid Mech*, 47:315–342, 2015.

[8] F. Bisbal, F. G??mez-pulido, P. Cabanas-Grand??o, N. Akoum, M. Calvo, D. Andreu, S. Prat-Gonz??lez, R. J. Perea, R. Villuendas, A. Berruezo, M. Sitges, A. Bay??s-Gen??s, J. Brugada, N. F. Marrouche, and L. Mont. Left Atrial Geometry Improves Risk Prediction of Thromboembolic Events in Patients With

Atrial Fibrillation. *Journal of Cardiovascular Electrophysiology*, 27(7):804–810, 2016.

[9] D. Bluestein. Research approaches for studying flow-induced thromboembolic complications in blood recirculating devices. *Expert review of medical devices*, 1(1):65–80, sep 2004.

[10] A. F. Bolger, E. Heiberg, M. Karlsson, L. Wigstrom, J. Engvall, A. Sigfridsson, T. Ebbers, J. P. Kvitting, C. J. Carlhall, and B. Wranne. Transit of blood flow through the human left ventricle mapped by cardiovascular magnetic resonance. *J Cardiovasc Magn Reson*, 9(5):741–747, 2007.

[11] M. Brambatti, S. J. Connolly, M. R. Gold, C. A. Morillo, A. Capucci, C. Muto, C. P. Lau, I. C. Van Gelder, S. H. Hohnloser, M. Carlson, E. Fain, J. Nakamya, G. H. Mairesse, M. Halytska, W. Q. Deng, C. W. Israel, J. S. Healey, and A. Investigators. Temporal relationship between subclinical atrial fibrillation and embolic events. *Circulation*, 129(21):2094–2099, 2014.

[12] M. R. Bristow, L. A. Saxon, J. Boehmer, S. Krueger, D. A. Kass, T. De Marco, P. Carson, L. DiCarlo, D. DeMets, B. G. White, D. W. DeVries, A. M. Feldman, and C. Investigators. Cardiac-resynchronization therapy with or without an implantable defibrillator in advanced chronic heart failure. *New England Journal of Medicine*, 350(21):2140–2150, 2004.

[13] J. Busch, D. Giese, L. Wissmann, and S. Kozerke. Reconstruction of divergence-free velocity fields from cine 3D phase-contrast flow measurements. *Magn Reson Med*, 69(1):200–210, 2013.

[14] A. J. Chorin. The numerical solution of the Navier-Stokes equations for an incompressible fluid. *Bull. Am. Math. Soc.*, 73:928–931, 1967.

[15] C. Devesa, L. Rossini, P. Martinez-Legazpi, C. Perez del Villar, Y. Benito, A. Barrio, F. Fernandez-Aviles, R. Yotti, J. C. del Alamo, and J. Bermejo. Prediction of intraventricular thrombosis by quantitative imaging of stasis: A pilot color-Doppler study in patients with acute myocardial infarction. *J Am Coll Cardiol*, 65 (10_S), 2015.

[16] L. Di Biase, P. Santangeli, M. Anselmino, P. Mohanty, I. Salvetti, S. Gili, R. Horton, J. E. Sanchez, R. Bai, S. Mohanty, A. Pump, M. Cereceda Brantes, G. J. Gallinghouse, J. D. Burkhardt, F. Cesarani, M. Scaglione, A. Natale, and F. Gaita. Does the left atrial appendage morphology correlate with the risk of stroke in patients with atrial fibrillation? Results from a multicenter study. *Journal of the American College of Cardiology*, 60(6):531–538, 2012.

[17] J. Eriksson, A. F. Bolger, T. Ebbers, and C. J. Carlhall. Four-dimensional blood flow-specific markers of LV dysfunction in dilated cardiomyopathy. *Eur Heart J Cardiovasc Imaging*, 14(5):417–424, 2013.

[18] J. Eriksson, C. J. Carlhall, P. Dyverfeldt, J. Engvall, A. F. Bolger, and T. Ebbers. Semi-automatic quantification of 4D left ventricular blood flow. *J Cardiovasc Magn Reson*, 12:9, 2010.

[19] J. Eriksson, P. Dyverfeldt, J. Engvall, A. F. Bolger, T. Ebbers, and C. J. Carlhall. Quantification of presystolic blood flow organization and energetics in the human left ventricle. *Am J Physiol Heart Circ Physiol*, 300(6):H2135–41, 2011.

[20] M. Esmaily-Moghadam, T. Y. Hsia, and A. L. Marsden. A non-discrete method for computation of residence time in fluid mechanics simulations. *Phys Fluids*, 25(11), 2013.

[21] D. Farwell, N. R. Patel, A. Hall, S. Ralph, and A. N. Sulke. How many people with heart failure are appropriate for biventricular resynchronization? *Eur Heart J*, 21(15):1246–1250, 2000.

[22] R. L. Fournier. *Basic transport phenomena in biomedical engineering.* CRC Press, Boca Raton, 3rd edition, 2012.

[23] A. G. Fredriksson, J. Zajac, J. Eriksson, P. Dyverfeldt, A. F. Bolger, T. Ebbers, and C. J. Carlhall. 4-D blood flow in the human right ventricle. *Am J Physiol Heart Circ Physiol*, 301(6):H2344–50, 2011.

[24] D. Garcia, J. C. Del Alamo, D. Tanne, R. Yotti, C. Cortina, E. Bertrand, J. C. Antoranz, E. Perez-David, R. Rieu, F. Fernandez-Aviles, and J. Bermejo. Two-dimensional intraventricular flow mapping by digital processing conventional color-Doppler echocardiography images. *IEEE Trans Med Imaging*, 29(10):1701–1713, 2010.

[25] A. Garcia-Alvarez, L. Fernandez-Friera, J. M. Garcia-Ruiz, M. Nuno-Ayala, D. Pereda, R. Fernandez-Jimenez, G. Guzman, D. Sanchez-Quintana, A. Alberich-Bayarri, D. Pastor-Escuredo, D. Sanz-Rosa, J. Garcia-Prieto, J. G. Gonzalez-Mirelis, G. Pizarro, L. J. Jimenez-Borreguero, V. Fuster, J. Sanz, and B. Ibanez. Noninvasive monitoring of serial changes in pulmonary vascular resistance and acute vasodilator testing using cardiac magnetic resonance. *J Am Coll Cardiol*, 62(17):1621–1631, 2013.

[26] C. W. Gardiner. *Handbook of stochastic methods for physics, chemistry, and the natural sciences.* Springer, Berlin ; New York, 3rd edition, 2004.

[27] B. Gellen, L. Biere, D. Logeart, O. Lairez, E. Vicaut, A. Furber, J. J. Mercadier, and M. Sirol. Timing of cardiac magnetic resonance imaging impacts on the detection rate of left ventricular thrombus after myocardial infarction. *JACC Cardiovasc Imaging*, doi:10.1016/j.jcmg.2016.12.006, 2017.

[28] M. Gharib, E. Rambod, A. Kheradvar, D. J. Sahn, and J. O. Dabiri. Optimal vortex formation as an index of cardiac health. *Proc Natl Acad Sci U S A*, 103(16):6305–6308, 2006.

[29] G. Goliasch, K. Goscinska-Bis, G. Caracciolo, A. Nakabo, G. Smolka, G. Pedrizzetti, J. Narula, and P. P. Sengupta. CRT improves LV filling dynamics: insights from echocardiographic particle imaging velocimetry. *JACC Cardiovasc Imaging*, 6(6):704–713, 2013.

[30] G. Gonzalez, D. Jimenez-Carretero, S. Rodriguez-Lopez, K. K. Kumamaru, E. George, R. San Jose Estepar, F. J. Rybicki, and M. J. Ledesma-Carbayo. Automated Axial Right Ventricle to Left Ventricle Diameter Ratio Computation in Computed Tomography Pulmonary Angiography. *PLoS One*, 10(5):e0127797, 2015.

[31] J. Gorcsan 3rd, T. Abraham, D. A. Agler, J. J. Bax, G. Derumeaux, R. A. Grimm, R. Martin, J. S. Steinberg, M. S. Sutton, C. M. Yu, G. American Society of Echocardiography Dyssynchrony Writing, G. American Society of Echocardiography Dyssynchrony Writing, and S. Heart Rhythm. Echocardiography for cardiac resynchronization therapy: recommendations for performance and reporting–a report from the American Society of Echocardiography Dyssynchrony Writing Group endorsed by the Heart Rhythm Society. *J Am Soc Echocardiogr*, 21(3):191–213, 2008.

[32] K. Guha and T. McDonagh. Heart failure epidemiology: European perspective. *Curr Cardiol Rev*, 9(2):123–127, 2013.

[33] O. Hachet, C. Guenancia, K. Stamboul, B. Daubail, C. Richard, Y. Bejot, V. Yameogo, A. Gudjoncik, Y. Cottin, M. Giroud, and L. Lorgis. Frequency and predictors of stroke after acute myocardial infarction: specific aspects of in-hospital and postdischarge events. *Stroke*, 45(12):3514–3520, 2014.

[34] T. T. Harfi, J. H. Seo, H. S. Yasir, N. Welsh, S. A. Mayer, T. P. Abraham, R. T. George, and R. Mittal. The E-wave propagation index (EPI): A novel echocardiographic parameter for prediction of left ventricular thrombus. Derivation from computational fluid dynamic modeling and validation on human subjects. *Int J Cardiol*, 227:662–667, 2017.

[35] S. Hendabadi, J. Bermejo, Y. Benito, R. Yotti, F. Fernandez-Aviles, J. C. Del Alamo, and S. C. Shadden. Topology of blood transport in the human left ventricle by novel processing of Doppler echocardiography. *Ann Biomed Eng*, 41(12):2603–2616, 2013.

[36] S. Homma, J. L. Thompson, P. M. Pullicino, B. Levin, R. S. Freudenberger, J. R. Teerlink, S. E. Ammon, S. Graham, R. L. Sacco, D. L. Mann, J. P. Mohr, B. M. Massie, A. J. Labovitz, S. D. Anker, D. J. Lok, P. Ponikowski, C. J. Estol, G. Y. Lip, M. R. Di Tullio, A. R. Sanford, V. Mejia, A. P. Gabriel, M. L. del Valle, R. Buchsbaum, and W. Investigators. Warfarin and aspirin in patients with heart failure and sinus rhythm. *N Engl J Med*, 366(20):1859–1869, 2012.

[37] G. R. Hong, G. Pedrizzetti, G. Tonti, P. Li, Z. Wei, J. K. Kim, A. Baweja, S. Liu, N. Chung, H. Houle, J. Narula, and M. A. Vannan. Characterization and quantification of vortex flow in the human left ventricle by contrast echocardiography using vector particle image velocimetry. *J Am Coll Cardiol Img*, 1(6):705–717, 2008.

[38] I. Hopper, M. Skiba, and H. Krum. Updated meta-analysis on antithrombotic therapy in patients with heart failure and sinus rhythm. *Eur J Heart Fail*, 15(1):69–78, 2013.

[39] D. A. Kass. Cardiac resynchronization therapy. *J Cardiovasc Electrophysiol*, 16 Suppl 1:S35–41, 2005.

[40] N. Kedia, K. Ng, C. Apperson-Hansen, C. H. Wang, P. Tchou, B. L. Wilkoff, and R. A. Grimm. Usefulness of atrioventricular delay optimization using Doppler assessment of mitral inflow in patients undergoing cardiac resynchronization therapy. *Am J Cardiol*, 98(6):780–785, 2006.

[41] W. F. Kerwin, E. H. Botvinick, J. W. O'Connell, S. H. Merrick, T. DeMarco, K. Chatterjee, K. Scheibly, and L. A. Saxon. Ventricular contraction abnormalities in dilated cardiomyopathy: effect of biventricular pacing to correct interventricular dyssynchrony. *J Am Coll Cardiol*, 35(5):1221–1227, 2000.

[42] P. J. Kilner, G. Z. Yang, A. J. Wilkes, R. H. Mohiaddin, D. N. Firmin, and M. H. Yacoub. Asymmetric redirection of flow through the heart. *Nature*, 404(6779):759–761, 2000.

[43] R. L. Kormos. Left ventricular assist device pump thrombosis: Understanding mechanisms as a key to causality. *J Thorac Cardiovasc Surg*, 149(3):673–674, 2015.

[44] R. M. Lang, L. P. Badano, V. Mor-Avi, J. Afilalo, A. Armstrong, L. Ernande, F. A. Flachskampf, E. Foster, S. A. Goldstein, T. Kuznetsova, P. Lancellotti, D. Muraru, M. H. Picard, E. R. Rietzschel, L. Rudski, K. T. Spencer, W. Tsang, and J. U. Voigt. Recommendations for cardiac chamber quantification by echocardiography in adults: an update from the American Society of Echocardiography and the European Association of Cardiovascular Imaging. *J Am Soc Echocardiogr*, 28(1):1–39 e14, 2015.

[45] E. F. Leonard, E. F. Grabowski, and V. T. Turitto. The role of convection and diffusion on platelet adhesion and aggregation. *Ann N Y Acad Sci*, 201:329–342, 1972.

[46] R. J. LeVeque. *Finite-volume methods for hyperbolic problems.* Cambridge University Press, Cambridge ; New York, 2002.

[47] L. Littmann and J. D. Symanski. Hemodynamic implications of left bundle branch block. *J Electrocardiol*, 33 Suppl:115–121, 2000.

[48] G. D. Lowe. Virchow's triad revisited: abnormal flow. *Pathophysiol Haemost Thromb*, 33(5-6):455–457, 2003.

[49] J. O. Mangual, F. Domenichini, and G. Pedrizzetti. Describing the highly three dimensional Right Ventricle flow. *Ann Biomed Eng*, 40(8):1790–1801, 2012.

[50] P. Martinez-Legazpi, J. Bermejo, Y. Benito, R. Yotti, C. Perez Del Villar, A. Gonzalez-Mansilla, A. Barrio, E. Villacorta, P. L. Sanchez, F. Fernandez-Aviles, and J. C. del Alamo. Contribution of the diastolic vortex ring to left ventricular filling. *Journal of the American College of Cardiology*, 64(16):1711–1721, oct 2014.

[51] B. M. Massie, J. F. Collins, S. E. Ammon, P. W. Armstrong, J. G. Cleland, M. Ezekowitz, S. M. Jafri, W. F. Krol, C. M. O'Connor, K. A. Schulman, K. Teo, S. R. Warren, and W. T. Investigators. Randomized trial of warfarin, aspirin, and clopidogrel in patients with chronic heart failure: the Warfarin and Antiplatelet Therapy in Chronic Heart Failure (WATCH) trial. *Circulation*, 119(12):1616–1624, 2009.

[52] K. May-Newman, Y. K. Wong, R. Adamson, P. Hoagland, V. Vu, and W. Dembitsky. Thromboembolism is linked to intraventricular flow stasis in a patient supported with a left ventricle assist device. *ASAIO J*, 59(4):452–455, 2013.

[53] R. Mittal, H. Dong, M. Bozkurttas, F. M. Najjar, A. Vargas, and A. von Loebbecke. A versatile sharp interface immersed boundary method for incompressible flows with complex boundaries. *Journal of Computational Physics*, 227(10):4825–4852, 2008.

[54] N. A. Mody and M. R. King. Influence of Brownian motion on blood platelet flow behavior and adhesive dynamics near a planar wall. *Langmuir*, 23(11):6321–6328, 2007.

[55] Z. G. Nadareishvili, Z. Choudary, C. Joyner, D. Brodie, and J. W. Norris. Cerebral microembolism in acute myocardial infarction. *Stroke*, 30(12):2679–2682, 1999.

[56] G. Nucifora, V. Delgado, M. Bertini, N. A. Marsan, N. R. Van de Veire, A. C. Ng, H. M. Siebelink, M. J. Schalij, E. R. Holman, P. P. Sengupta, and J. J. Bax. Left ventricular muscle and fluid mechanics in acute myocardial infarction. *Am J Cardiol*, 106(10):1404–1409, 2010.

[57] H. Pavlopoulos and P. Nihoyannopoulos. Recent advances in cardiac resynchronization therapy: echocardiographic modalities, patient selection, optimization, non-responders–all you need to know for more efficient CRT. *Int J Cardiovasc Imaging*, 26(2):177–191, 2010.

[58] R. A. Peattie. Transport phenomena in biomedical engineering principles and practices, 2013.

[59] G. Pedrizzetti and F. Domenichini. Nature Optimizes the Swirling Flow in the Human Left Ventricle. *Physical Review Letters*, 95(10):1–4, sep 2005.

[60] G. Pedrizzetti, G. La Canna, O. Alfieri, and G. Tonti. The vortex-an early predictor of cardiovascular outcome? *Nat Rev Cardiol*, 11(9):545–553, 2014.

[61] G. Pedrizzetti, A. R. Martiniello, V. Bianchi, A. D'Onofrio, P. Caso, and G. Tonti. Changes in electrical activation modify the orientation of left ventricular flow momentum: novel observations using echocardiographic particle image velocimetry. *Eur Heart J Cardiovasc Imaging*, 2015.

[62] A. Quaini, S. Canic, and D. Paniagua. Numerical characterization of hemodynamics conditions near aortic valve after implantation of Left Ventricular Assist Device. *Math Biosci Eng*, 8(3):785–806, 2011.

[63] E. E. R. Richter Y. Cardiology is flow. *Circulation*, 113(23):2679–2682, 2006.

[64] D. Rodriguez Munoz, M. Markl, J. L. Moya Mur, A. Barker, C. Fernandez-Golfin, P. Lancellotti, and J. L. Zamorano Gomez. Intracardiac flow visualization: current status and future directions. *Eur Heart J Cardiovasc Imaging*, 14(11):1029–1038, 2013.

[65] L. Rossini, P. Martinez-Legazpi, V. Vu, L. Fernández-Friera, C. Pérez del Villar, S. Rodríguez-López, Y. Benito, M.-G. Borja, D. Pastor-Escuredo, R. Yotti, M. J. Ledesma-Carbayo, A. M. Kahn, B. Ibáñez, F. Fernández-Avilés, K. May-Newman, J. Bermejo, and J. C. del Alamo. A clinical method for mapping and quantifying blood stasis in the left ventricle. *J Biomech*, In press, 2015.

[66] P. G. Saffman. *Vortex Dynamics.* Cambridge University Press, Cambridge, 1993.

[67] N. S. Sawhney, A. D. Waggoner, S. Garhwal, M. K. Chawla, J. Osborn, and M. N. Faddis. Randomized prospective trial of atrioventricular delay programming for cardiac resynchronization therapy. *Heart Rhythm*, 1(5):562–567, 2004.

[68] L. A. Saxon, W. F. Kerwin, M. K. Cahalan, J. M. Kalman, J. E. Olgin, E. Foster, N. B. Schiller, J. S. Shinbane, M. D. Lesh, and S. H. Merrick. Acute effects of intraoperative multisite ventricular pacing on left ventricular function and activation/contraction sequence in patients with depressed ventricular function. *J Cardiovasc Electrophysiol*, 9(1):13–21, 1998.

[69] J. H. Seo, T. Abd, R. T. George, and R. Mittal. A coupled chemo-fluidic computational model for thrombogenesis in infarcted left ventricles. *Am J Physiol Heart Circ Physiol*, 310(11):H1567–82, 2016.

[70] J. H. Seo and R. Mittal. Effect of diastolic flow patterns on the function of the left ventricle. *Phys Fluids*, 25:110801, 2013.

[71] J. Son, W. Park, J. Choi, H. Houle, M. Vannan, G. Hong, and N. Chung. Abnormal left ventricular vortex flow patterns in association with left ventricular apical thrombus formation in patients with anterior myocardial infarction: a quantitative analysis by contrast echocardiography. *Circulation Journal*, 76(11):2640–6, 2012.

[72] T. Stanton, N. M. Hawkins, K. J. Hogg, N. E. Goodfield, M. C. Petrie, and J. J. McMurray. How should we optimize cardiac resynchronization therapy? *Eur Heart J*, 29(20):2458–2472, 2008.

[73] J. M. Tarbell. Mass transport in arteries and the localization of atherosclerosis. *Annu Rev Biomed Eng*, 5:79–118, 2003.

[74] R. B. Thompson and E. R. McVeigh. Fast measurement of intracardiac pressure differences with 2D breath-hold phase-contrast MRI. *Magn Reson Med*, 49(6):1056–1066, 2003.

[75] H. D. Toeg, T. Al-Atassi, J. P. Garcia, and M. Ruel. An update on mechanical circulatory support for heart failure therapy. *Curr Opin Cardiol*, 29(2):167–173, 2014.

[76] C. Vecchio, F. Chiarella, G. Lupi, P. Bellotti, and S. Domenicucci. Left ventricular thrombus in anterior acute myocardial infarction after thrombolysis. A GISSI-2 connected study. *Circulation*, 84(2):512–519, 1991.

[77] A. D. Waggoner, L. De Las Fuentes, M. N. Faddis, M. J. Gleva, K. E. Spence, and V. G. Davila-Roman. Left ventricular diastolic filling prior to cardiac resynchronization therapy: implications for atrioventricular delay programming. *Pacing Clin Electrophysiol*, 31(7):838–844, 2008.

[78] H. Watanabe, S. Sugiura, and T. Hisada. The looped heart does not save energy by maintaining the momentum of blood flowing in the ventricle. *Am J Physiol Heart Circ Physiol*, 294(5):H2191–6, 2008.

[79] J. W. Weinsaft, H. W. Kim, A. L. Crowley, I. Klem, C. Shenoy, L. Van Assche, R. Brosnan, D. J. Shah, E. J. Velazquez, M. Parker, R. M. Judd, and R. J. Kim. LV thrombus detection by routine echocardiography: insights into performance characteristics using delayed enhancement CMR. *JACC Cardiovasc Imaging*, 4(7):702–712, 2011.

[80] J. W. Weinsaft, J. Kim, C. B. Medicherla, C. L. Ma, N. C. Codella, N. Kukar, S. Alaref, R. J. Kim, and R. B. Devereux. Echocardiographic algorithm for post-myocardial infarction LV thrombus: a gatekeeper for thrombus evaluation by delayed enhancement CMR. *JACC Cardiovasc Imaging*, 9(5):505–515, 2016.

[81] J. W. Weinsaft, R. J. Kim, M. Ross, D. Krauser, S. Manoushagian, T. M. LaBounty, M. D. Cham, J. K. Min, K. Healy, Y. Wang, M. Parker, M. J. Roman, and R. B. Devereux. Contrast-enhanced anatomic imaging as compared to contrast-enhanced tissue characterization for detection of left ventricular thrombus. *JACC Cardiovasc Imaging*, 2(8):969–979, 2009.

[82] F. M. White. *Viscous Fluid Flow*. McGraw-Hill, 1991.

[83] L. Wigstrom, T. Ebbers, A. Fyrenius, M. Karlsson, J. Engvall, B. Wranne, and A. F. Bolger. Particle trace visualization of intracardiac flow using time-resolved 3D phase contrast MRI. *Magn Reson.Med.*, 41(4):793–799, 1999.

[84] K. Wong, G. Samaroo, I. Ling, W. Dembitsky, R. Adamson, J. C. del Álamo, and K. May-Newman. Intraventricular flow patterns and stasis in the LVAD-assisted heart. *Journal of Biomechanics*, 47(6):1485–1494, apr 2014.

[85] H. B. Xiao, S. J. Brecker, and D. G. Gibson. Effects of abnormal activation on the time course of the left ventricular pressure pulse in dilated cardiomyopathy. *Br Heart J*, 68(4):403–407, 1992.

[86] H. B. Xiao, C. Roy, S. Fujimoto, and D. G. Gibson. Natural history of abnormal conduction and its relation to prognosis in patients with dilated cardiomyopathy. *Int J Cardiol*, 53(2):163–170, 1996.

[87] G. Z. Yang, R. Merrifield, S. Masood, and P. J. Kilner. Flow and myocardial interaction: an imaging perspective. *Philos Trans R Soc Lond B Biol Sci*, 362(1484):1329–1341, 2007.

[88] R. Yotti, J. Bermejo, M. M. Desco, J. C. Antoranz, J. L. Rojo-Alvarez, C. Cortina, C. Allue, H. Rodriguez-Abella, M. Moreno, and M. A. Garcia-Fernandez. Doppler-derived ejection intraventricular pressure gradients provide a reliable assessment of left ventricular systolic chamber function. *Circulation*, 112(12):1771–1779, 2005.

[89] B. Zhang, C. Gao, Q. Hou, J. Yin, L. Xie, S. Pu, Y. Yi, and Q. Gao. Different independent susceptibility markers for first-ever cerebral infarction and myocardial infarction in young patients. *J Neurol*, 259(7):1420–1425, 2012.

[90] Q. Zhang, J. W. H. Fung, Y. S. Chan, H. C. K. Chan, H. Lin, S. Chan, and C. M. Yu. The role of repeating optimization of atrioventricular interval during interim and long-term follow-up after cardiac resynchronization therapy. *Int J Cardiol*, 124(2):211–217, 2008.

[91] J. J. Zwanenburg, M. J. Gotte, J. P. Kuijer, M. B. Hofman, P. Knaapen, R. M. Heethaar, A. C. van Rossum, and J. T. Marcus. Regional timing of myocardial shortening is related to prestretch from atrial contraction: assessment by high temporal resolution MRI tagging in humans. *Am J Physiol Heart Circ Physiol*, 288(2):H787–94, 2005.